UNIVERSIDADE D
COIMBRA

Raquel Cadete Laginha da Silva

New Drugs to Fight Osteosarcoma – A Complete Vibrational Microspectroscopy Study

Dissertação no âmbito do Mestrado em Química, na área de especialização em Química Avançada e Industrial, orientada pela Doutora Ana Batista de Carvalho e co-orientada pelo Professor Doutor Luís Batista de Carvalho e apresentada ao Departamento de Química da Faculdade de Ciências e Tecnologia da Universidade de Coimbra.

Setembro de 2023

À minha avó,

Acknowledgements

Como disse Dag Hammarskjöld, "For all that has been, Thanks. To all that shall be, Yes."

Seria impensável chegar ao fim desta etapa e não agradecer às pessoas que me ajudaram a torná-la possível.

Primeiro quero agradecer à Doutora Ana Batista de Carvalho e ao Professor Doutor Luís Batista de Carvalho por me terem tão bem acolhido na Unidade de I&D Química-Física Molecular, por me terem sempre incentivado a querer mais, a toda a ajuda dada por ambos no desenvolvimento deste trabalho e a alcançar oportunidades únicas. Se tenho um sítio a que posso chamar segunda casa é graças a vocês.

Obrigada a todos os membros da unidade que me ajudaram de forma incansável nos momentos mais difíceis e resolveram muitas das minhas crises existenciais. A todos vós obrigado por todas as amizades que ganhei. Dentro destas pessoas, há três que seria impensável não agradecer em separado.

À Clara, obrigada por toda a tua ajuda tanto no trabalho como a nível pessoal, tranquilidade em momentos difíceis e fotos dos gatos, sem ti não teria conseguido.

À Jéssica, a minha parceira de laboratório que está sempre disponível para discutir uma ideia mirabolante que eu tenho às 3h da manhã, que atura o meu mau feitio, que me incentiva a pensar noutras possibilidades, aceita sem nunca criticar os meus miaus nos momentos mais aleatórios, corretora dos meus textos tenebrosos, entre muito outras coisas. Não acredito que tenha palavras para descrever o quão importante és para mim e para te agradecer.

À Ana, possivelmente és a pessoa que eu mais tenho dificuldade em agradecer, não porque fizeste pouco, pelo contrário, não há palavras que eu considere suficientemente dignas para o fazer. Obrigada pela amizade, pelo apoio incondicional tanto a nível académico como pessoal. Sinto que cresci bastante nestes últimos anos, e foste a pessoa a quem tenho mais a agradecer por isso. Sei que tenho alguém que posso sempre contar, nem que seja para poder tirar do sério.

À Cruz, a minha mulher, a minha companhia nestes cinco anos. Obrigada por tudo, pelo companheirismo, construção de tunas, colega de laboratório (shake, shake shake)

restruturação sofisticada de ideia aleatórias, entre muitas outras coisas. Quando penso em Coimbra és a primeira pessoa que me vem à mente.

A todos os meus amigos criados na universidade, agradeço a vossa camaradagem e acompanhamento de atividades lúdicas.

À Majó, Nanci, Bia, Nuno e Casimiro os meus amigos que me acompanham desde o secundário, obrigada por todo o apoio, sei que vos tenho para a vida. Desculpem a ausência, mas brevemente volto a acompanhar-vos para irmos ao Mc e descobrir o caminho para a lagoa Azul

À Tia Lina, Ângela, Paula, Margarida e Henrique, não vos posso deixar de agradecer por todo o vosso apoio.

À Pinky, a principal causadora de danos no meu computador, nunca percebi como é que alguém era capaz de gostar tanto de um animal, agora entendo.

Ao meu irmão, obrigada pelo financiamento e não só. Apesar das poucas palavras sei que tenho sempre o teu apoio.

Aos meus pais, por tudo, mas neste caso em específico, por no primeiro ano não me deixarem desistir, um dos melhores conselhos que já me deram. Obrigada por todo o apoio, presença, incentivo, e muito mais. Sem a vossa ajuda incondicional este trabalho não seria possível.

Por último, a pessoa à qual dedico o meu trabalho, à minha avó. Obrigada por seres um dos meus pilares, sem ti isto seria impossível. Por seres a pessoa mais crítica, mas o fazeres sempre com tanto amor. Obrigada por mostrares tanto orgulho em mim e de fazeres um esforço para ler esta tese.

Abstract

Worldwide, cancer still is the second cause of death-disease related being expected to rise up to 22 million cases per year within the next two decades. Osteosarcoma (OS) is the most common primary malignant bone cancer with a poor prognosis for patients with metastatic or recurrent disease. Some progress has been achieved regarding OS therapy and survival rates have increased from less than 20% to 65-70% with the multidrug regimen designated as MAP (methotrexate (MTX), doxorubicin (DOX), and cisplatin). However, the severe toxicity and deleterious side-effects associated with MAP are a limiting factor. In this context, the currently ongoing European and American Osteosarcoma Study (EURAMOS-1) phase III clinical trial seeks to improve survival rate of OS patients through MAP concentrations adjustments. The advantage of a combined therapy is to be able to deliver the same or enhanced cytotoxic effect relative to the one attained with each drug individually. Upon cells' viability evaluation against osteosarcoma cell line, MG-63, $Pd_3Spd_2Cl_6$ was considered the best drug to be tested against a healthy cell line, HOb.

Vibrational microspectroscopy both FTIR with synchrotron radiation and Raman were used to assess the drugs' bioavailability, biodistribution, metabolic impact as well as cellular response to treatment with either newly synthesized cisplatin-like compounds (Pd_2SpmCl_4 and $Pd_3Spd_2Cl_6$) alone or in combination in the MAP regimen against both osteosarcoma (cancer cells) and osteoblasts (healthy cells) cell lines.

The results thus gathered clearly evidenced a spectral discrimination between the control and the drug-treated cells with the IC_{50} values, obtained for osteosarcoma at 48 h for cisplatin (12 μM), Pd_2SpmCl_4 (14 μM), and $Pd_3Spd_2Cl_6$ (12 μM), applied at both cell lines, MG-63 and HOb. As well as with drug combination, administered according to the EURAMOS-1 protocol in order to compare the protentional treatment drugs with cisplatin at 96 h of incubation time (4.8 μM of drug + 3 μM of DOX at 0h plus an additional dose of 4.8 μM of MTX at 72 h).

Resumo

A nível mundial, o cancro ainda é a segunda causa de morte devido a doença, prevendo-se que aumente para 22 milhões de casos por ano nas próximas duas décadas. O osteossarcoma (OS) é o cancro ósseo primário mais comum, com um mau prognóstico para pacientes com doença metastática ou recorrente. A terapia do OS tem tido alguma evolução positiva tendo as taxas de sobrevivências aumentado de menos de 20% para 65-70% utilizando o regime multimedicamentoso designado como MAP (metotrexato (MTX), doxorrubicina (DOX) e cisplatina). No entanto, a elevada toxicidade e os efeitos colaterais associados ao MAP são um fator limitante. Neste contexto, o ensaio clínico de fase III do *European and American Osteosarcoma Study* (EURAMOS-1) em curso procura aumentar a taxa de sobrevivência de pacientes com OS através de variações nas concentrações dos fármacos presentes no MAP. A vantagem de uma terapia combinada é a possibilidade de obter o mesmo ou maior efeito citotóxico em relação ao obtido com cada um dos medicamentos individualmente. Após a avaliação da viabilidade celular na linha celular de osteossarcoma MG-63, o composto $Pd_3Spd_2Cl_6$ foi considerado o melhor fármaco a ser testado numa linha celular saudável, HOb.

A microespetroscopia vibracional, tanto de FTIR com radiação de sincrotrão como de Raman, foram utilizadas para avaliar a biodisponibilidade, biodistribuição e impacto metabólico dos medicamentos, bem como a resposta celular ao tratamento com os compostos semelhantes à cisplatina sintetizados (Pd_2SpmCl_4 e $Pd_3Spd_2Cl_6$) tanto na sua forma isolada como em combinação de acordo com o regime MAP em linhas celulares de osteossarcoma (células cancerígenas) e osteoblastos (células saudáveis).

Os resultados obtidos evidenciaram uma clara discriminação espectral entre o controlo e as células tratadas com o fármaco com os valores de IC_{50}, obtidos para o osteossarcoma às 48 h para a cisplatina (12 μM), o Pd_2SpmCl_4 (14 μM) e o $Pd_3Spd_2Cl_6$ (12 μM), administrados a ambas as linhas celulares, MG-63 e HOb. Assim como com a combinação, administrada de acordo com o protocolo EURAMOS-1 de modo a comparar o efeito potenciador dos novos fármacos com a cisplatina às 96 horas de tempo de incubação total (4,8 μM de fármaco + 3 μM de DOX às 0h mais uma dose adicional de 4,8 μM de MTX às 72 h).

Table of Contents

1. Introduction

1.1. Bone Cancer

Worldwide, cancer is the second cause of death by a disease, and it is expected to rise to 22 million cases per year within the next two decades. Cancer can spread from organs to bone, known as bone metastasis, which are more common than primary bone cancers (less than 1% of all cancers). In 2023, are estimated 3970 new cases (1810 in females and 2160 in males) and 2140 deaths (940 in females and 1200 in males) from primary cancer of the bones and joints by the American Cancer Society [1].

Although bone cancer can begin in any bone, studies report the pelvis and the long bones in the arms and legs as the most frequent places for bone cancer to develop. A scheme of bone cancer in the femur can be found in Figure 1. The definition of bone cancer thus not included metastasis in the bone from other types of cancer [2].

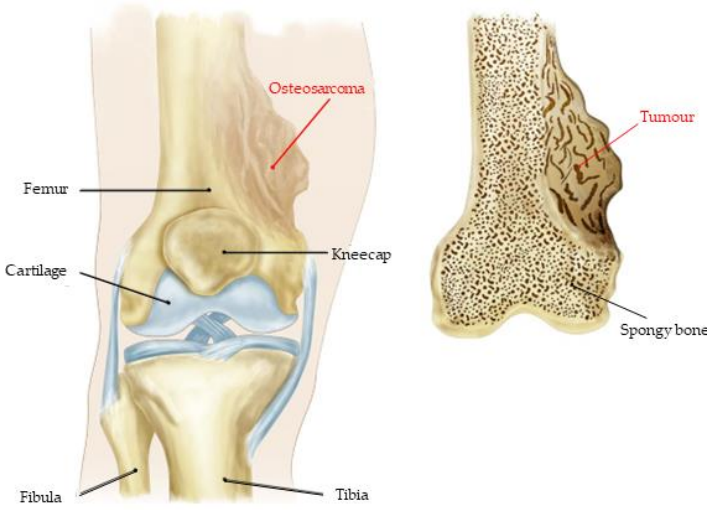

Figure 1: Schematic representation of a type of bone cancer, osteosarcoma.

Bones are composed by four types of cells, osteoclasts, osteoblasts, osteocytes, and bone lining [3]. Osteoblasts are the cells that construct new bone, osteoclasts the ones which dissolve old bone, this continuous formation and dissolution is what maintain the bones strong. Moreover, osteocytes which control the extracellular concentration of phosphate and calcium in bone tissue, and bone lining are present in the surface of the bone [4-8].

There are seven types of bone cancer:

- Osteosarcoma;
- Ewing sarcoma;
- Chondrosarcoma;
- High-grade undifferentiated pleomorphic sarcoma (UPS) of bone;
- Fibrosarcoma of bone;
- Giant cell tumour of bone;
- Chordoma.

The most common treatment in these cases is surgical removal, although chemo and radiation therapies can be necessary, it depends on the type of bone cancer [2, 9, 10].

1.2. Osteosarcoma

Osteosarcoma (OS) is the most common primary malignant bone cancer with poor prognosis for patients with metastatic or recurrent disease. Although OS can develop at any age, the incidence is greater in children and young adults, and more prevalent in males than in females. Hence, there is a need to develop new and more effective anticancer agents in order to kill neoplastic cells while having minimal effects on healthy tissue [2]. According to the International Classification of Childhood Cancer, ICCC, for the United States, the incidence rate per million in children from birth to 14 years old is 4.3 and for young adults, from 15 to 19 years 8.0, with a 5-year relative survival of 69% and 67%, respectively [1, 2, 11].

According to the recent World Health Organization, WHO, Osteosarcoma can be divided in high-, intermediate- and low-grade, which are classified in different therapeutic approaches [12].

1.2.1. Current Therapeutic Approaches

Some challenges are found in the diagnosis and management of osteosarcoma, and a way to bypass them is a multidisciplinary approach. Presently, the techniques used are radiotherapy, surgical excision and multiagent systematic therapy. Although low-grade osteosarcoma can be treated by surgery, high- grade treatment consists in the combination of chemotherapy followed by surgery and then more chemotherapy, (sometimes radiation

therapy is also needed). The chemotherapy employed usually consists in a multidrug regimen [10, 13].

In the last 30 years some progresses have been achieved regarding OS therapy and survival rates have increased from less than 20% to 65-70% with the multidrug regimen designated as MAP (methotrexate (MTX), adriamycin (commonly known as doxorubicin (DOX)) and cisplatin), in Figure 2 is represented the molecular structure for each drug. However, there is a limiting factor, the severe toxicity associated with MAP implying damage to the kidneys, heart, and a decrease of the bone marrow activity (cisplatin nephrotoxicity, DOX cardiotoxicity, and MTX nephrotoxicity and myelosuppression) [2, 12, 14]. In this context, the currently ongoing European and American Osteosarcoma Study (EURAMOS-1) presently in phase III clinical trial seeks to improve survival rate of OS patients through MAP concentrations adjustments [15]. The EURAMOS-1 study consists in a multimodal treatment that includes surgery as well as pre- and postoperative chemotherapy regimens [15, 16].

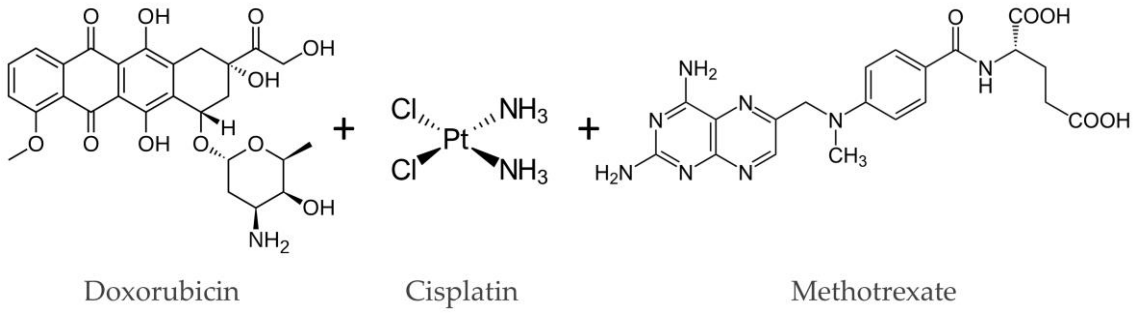

Figure 2: Molecular Structure of MAP: doxorubicin (DOX), cisplatin and methotrexate (MTX).

1.3. Pd and Pt Complexes

Chemotherapy is one of the most common forms of treatment to prevent neoformed tissue from growing. Drugs used in chemotherapy can be categorised according to their mode of action, such as metallic complexes, where the complexes described in the present work are inserted, antimetabolites, and immunotherapy. Compared to other modes, complexes that bond directly to DNA (purine's nitrogen atoms) by the hydrolysis of the chloride groups (Figure 3(A) and (B)) prove to be quite effective preventing its replication. On the other hand, phosphate clamps (Figure 3(C)) are a different type of complex-DNA interactions, it may occur when the complex does not contain those leaving groups to

suffer hydrolysis, and by being positively charged, can establish electrostatic interactions with the DNA phosphates. Combined with Van der Waals forces between the hydrogen from the ligands' carbon chain and the DNA backbone [2, 17-25].

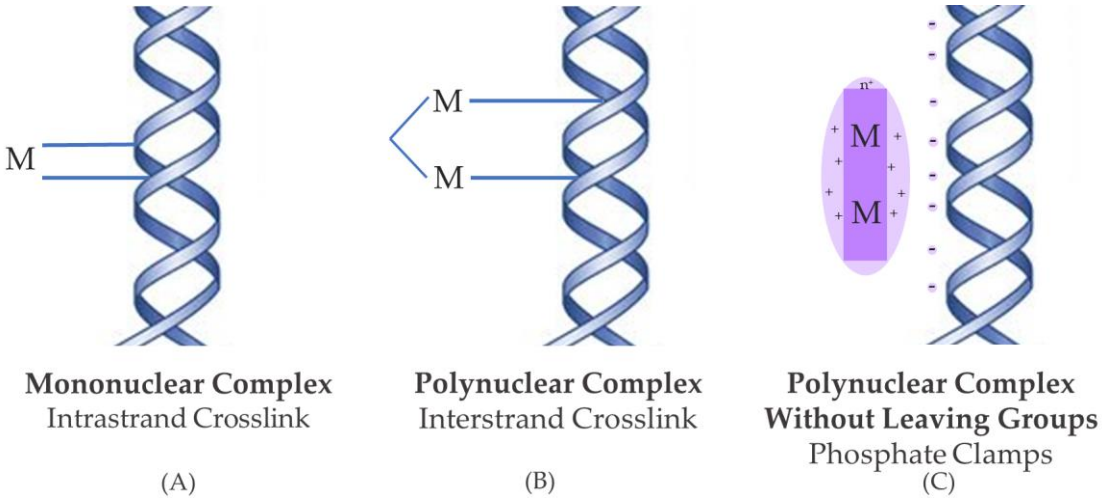

Figure 3: Schematic representation of different mechanisms of anticancer agents.

1.3.1. Pd and Pt Complexes approved for Clinical Use

In the early stages of the research of metal complexes with platinum, the first compound to be synthesized and administered was cis-dichlorodiamineplatinum (II), the common name being cisplatin. It was first synthesized in 1845 by Michele Peyrone, and discovered again by Barnett Rosenberg in 1960, during a study of the effect of electric field on bacterial growth of *E. Coli*. Thus, in the 1970s, cisplatin was tested and approved in clinical trials against metastatic ovarian and testicular cancers [26, 27]. Since then, and with the positive results of cisplatin in the chemotherapy treatment of cancer, the development of inorganic anticancer agents has gained prominence, and over the years complexes have been developed with different metal ions, such as ruthenium (II) and palladium (II), and ligands, namely phosphines, chloroquine, and polyamines [28-30].

Platinum complexes approved for clinical use as anticancer agents are cisplatin and second- and third-generation complexes, carboplatin and oxaliplatin, respectively. However, they have some side effects at the renal and hepatic level, as well as acquired resistance (Figure 4) [2, 31].

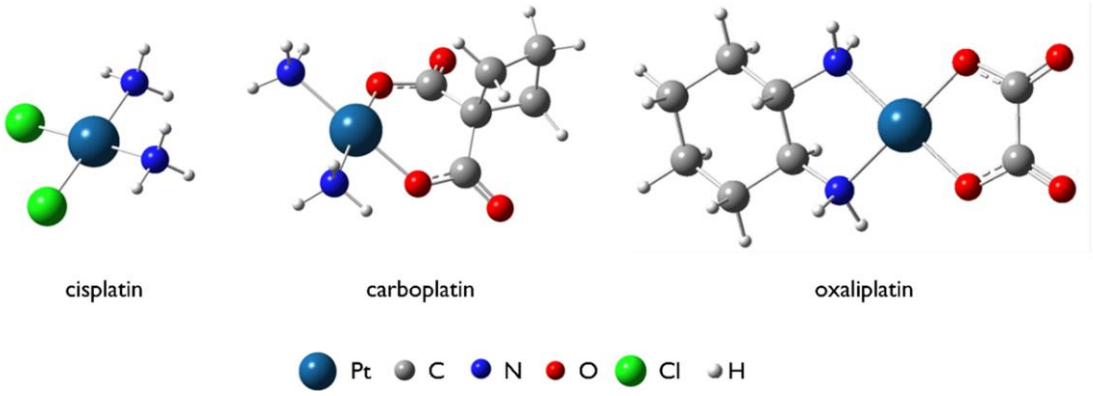

Figure 4: Structural representation of cisplatin, carboplatin and oxaliplatin, compounds used in the clinic as anticancer drugs.

The development of new anticancer agents aims at reducing toxicity in order to minimize side effects, increase treatment efficacy, and overcome cellular resistance mechanisms. In short, the new compounds are evaluated in five parameters, absorption, distribution, metabolism, excretion, and toxicity. This optimization is carried out based, not only on the structure, choice of metal ion/ions, type of leaving groups and amine ligands, but also on its conformation, as these factors affect its reactivity and absorption. For an in-depth knowledge of the complexes and determination of structure-activity relationships (SARs), vibrational spectroscopy techniques coupled to quantum mechanical calculation may be used, for understanding the structures and conformational behaviour, by comparison of the theoretical and the experimental vibrational methods [28, 32, 33].

1.4. Polynuclear Complexes of Platinum and Palladium with Polyamines

Biogenic polyamines, putrescine, spermine and spermidine (Figure 5), are present in all cells since they are essential for eukaryotic cells growth. One of the main features consists of polycations, which allows the interaction with negatively charged molecules such as DNA [28, 34, 35].

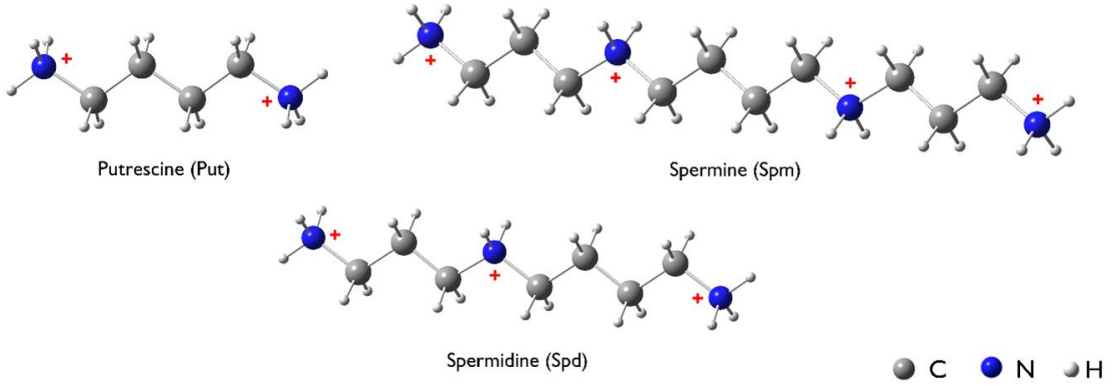

Figure 5: Structural representation of the biogenic polyamines (putrescine, spermine and spermidine) at physiological conditions.

These ligands have high conformational freedom and lipo-hydrophilic duality. The advantage of using polyamines as ligands is that it gives the complexes a greater cytotoxic effect. Complexes with this type of ligand cause a more severe and less reversible DNA damage than conventional complexes, because not only the ligand flexibility provides intrachain crosslinks, but also interchain crosslinks [28, 29, 36].

Although the metals, platinum and palladium are quite identical, belonging to the same group in the periodic table, having 8 valence electrons, it has been observed experimentally that chemical reactions with Pd(II) complexes are faster than those with Pt(II) [17]. As platinum has more occupied orbitals than palladium, it has a higher energy splitting in the 5d orbitals than palladium in the 4d, according to the Ligand Field Theory. This leads to the electrons in the 5d orbital being less attracted to the nucleus, allowing the donation of 2 electrons from the valence layer to the ligands with the formation of more stable bonds, these being dative bonds, that is, formed entirety by the donation of charge of the metal towards the ligand, which will make the complex more inert than those formed with palladium. As observed in recent studies, the use of polynuclear complexes instead of mononuclear complexes presents a higher advantage, as it leads to an increase in the antineoplastic activity of the drug [36]. Polynuclear complexes of platinum and palladium with polyamines are compounds that have been studied in the last decades, *e.g.*, their reactivity of palladium and platinum complexes, their effect against several types of cancer [17, 36-40]. In the case of the inorganic complex, Pd_2SpmCl_4 (Figure 6) is in many studies compared to cisplatin [28, 38, 39, 41]. With the positive results shown for this type of polynuclear drug in cancer treatment, the present work consists on the

comparison of cisplatin and Pd_2SpmCl_4 to four new polynuclear compounds: $Pd_2Put_2Cl_4$, $Pt_2Put_2(NH_3)_4Cl_4$ ($Pt_2Put_2(NH_3)_4^{4+}$), $Pd_3Spd_2Cl_6$ and $Pt_3Spd_2Cl_6$.

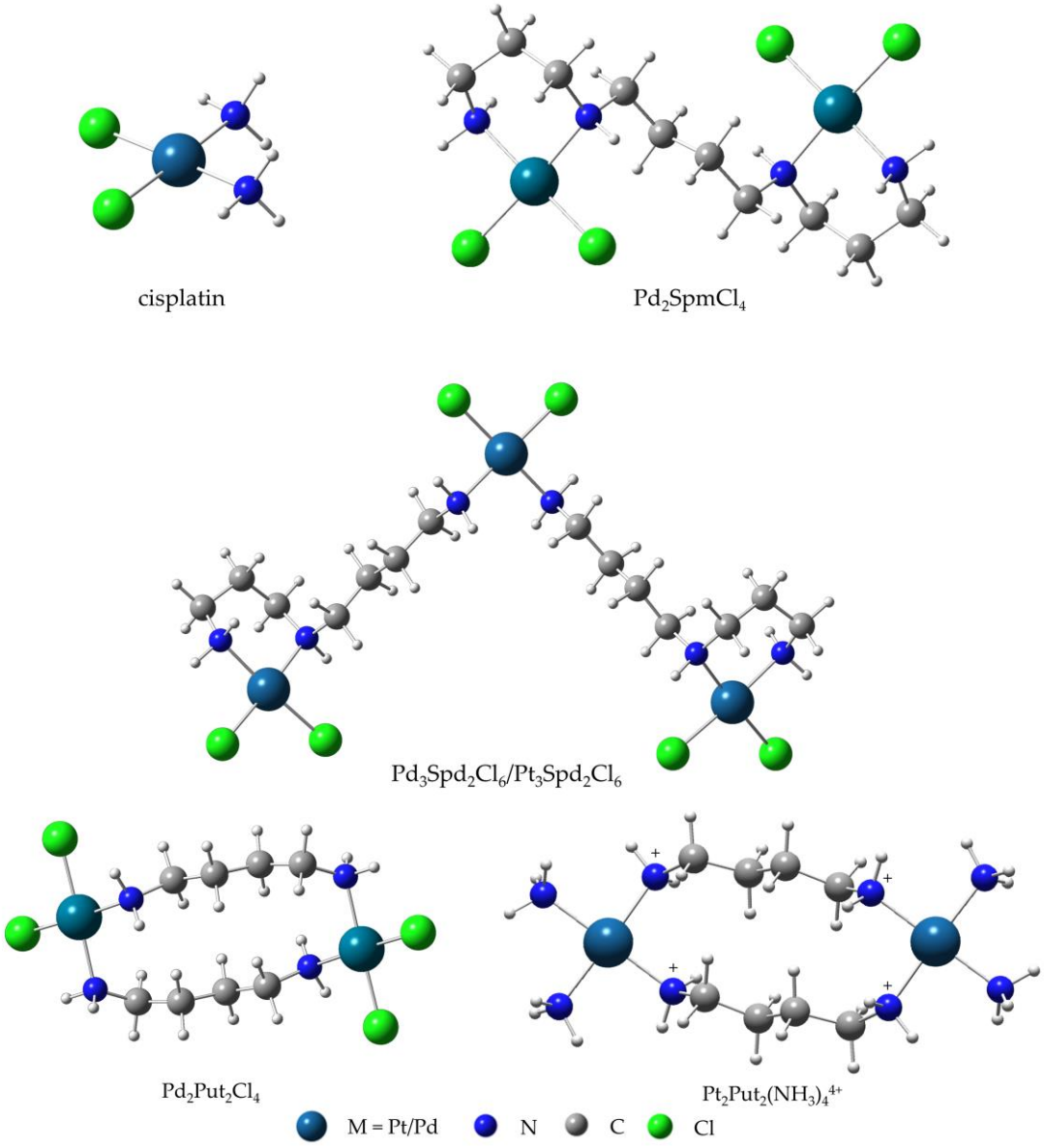

Figure 6: Structural representation of cisplatin, Pd_2SpmCl_4, $Pd_2Put_2Cl_4$, $Pt_2Put_2(NH_3)_4^{4+}$, $Pd_3Spd_2Cl_6$ and $Pt_3Spd_2Cl_6$.

1.5. Computational Chemistry

1.5.1. Quantum Mechanics

The interrelation of quantum mechanics and vibrational spectroscopy provides a deep understanding of molecular conformation.

Electronic structure calculations of molecules, in the stationary state, can be achieved by the *ab initio* method, which is based on Schrödinger's equation, by solving the equation (1), time-independent, also known as the Hamiltonian eigenvalues' equation:

$$\hat{H}\Psi=E\Psi \tag{1}$$

Where the Hamiltonian operator ($\hat{H}$), wave function (Ψ) and energy (E) describing the system are dependent on every particle's coordinates.

The Hamiltonian operator is composed of the sum of the kinetic and potential energies of all the particles in the system, equation (2) which describes the momentum of the particles (kinetic energy) and the interaction between particles and their system (potential energy) for N electrons and M nucleus in the system.

$$H= -\sum_{i}^{N}\frac{1}{2}\nabla_i^2 - \sum_{i}^{N}\sum_{A}^{M}\frac{Z_A}{|r_i-R_A|} + \sum_{i}^{N}\sum_{k>i}^{M}\frac{1}{|r_k-r_i|} + \sum_{A=1}^{M}\sum_{B>A}^{M}\frac{Z_AZ_b}{R_{AB}} \tag{2}$$

The Laplacian operator, ∇, is given by the second derivative concerning the electron's cartesian coordinates, equation (3).

$$\nabla^2 = \frac{\partial^2}{\partial x^2}+\frac{\partial^2}{\partial y^2}+\frac{\partial^2}{\partial z^2} \tag{3}$$

The equation (2) can be simplified by the following terms: T corresponding to the kinetics energy and the sum of the different potential energies considered in the system, the nucleus-electron attraction (V_{ne}), electron-electron interaction (V_{ee}) and nucleus-nucleus repulsion (E_{NN}) the following equation (4),

$$H=T+V_{ne}+V_{ee}+E_{NN} \tag{4}$$

The methods used in the present work are based on the molecular orbital theory (MO) where a new orbital is formed by combining the orbitals of each electron sharing atom. This consists of an orbital approximation, whereas in monoelectronic atoms this does not happen, because the wave function depends only on one coordinate, so the Schrödinger equation has an analytical solution. In polyelectronic atoms, this approximation occurs in agreement with the Pauli principle, so the wave function is decomposed in a product of monoelectronic functions resulting in an antisymmetric solution [42, 43].

The resolution of Schrödinger's equation in *ab initio* calculations required three approximations: Hamiltonian, orbital and Born-Oppenheimer. The last one considers the atom's nucleus to be static, since the electrons and nucleus have different movement velocities the wave function is divided in two, one for the nucleus's static geometry and one with the influence of electronic potential energy [42].

1.5.2. Hartree-Fock Method

The HF method with Self Consistent Field (SCF), (HF-SCF) is the beginning point of the majority of *ab initio* methods, designated as post-Hartree-Fock. Based on the MO theory, supposing that the number of MO is equal to the atomic orbital the MO is calculated according to the Linear Combination of Atomic Orbitals (LCAO).

HF foundation is based on the approximation for the determination of wave function and energy of various electrons system in the stationary state by solving the Schrodinger equation. From this method, one Slater determinant allows the approximation of N orbital spins for the wave function of N bodies in a quantum system. A solution of the derivation of a group of N equations accoupled to N spin orbital is obtained by the variational method. A solution of this equation gives a wave function of Hartree-Fock and the ground-state energy. In the calculation of electronic energy, there are essentially two principal approximations: the Hamiltonian (perturbation method) and wave function (variational method) [44].

As worldwide used, the HF method is computationally efficient. Nevertheless, have two inabilities, the repulsion energy as an average of the MO and the inexistence of an electronic correlation term [45].

1.5.3. Density Functional Theory Method

Density functional theory (DFT) is an *ab initio* computational method that allows to solve systems with a large amount of electron, by the application of functionals without experimental or empiric parameters. Functionals are functions that take another function, about electronic density, as an argument, that allows the obtainment of correlation energy. From the premise that the entire energy of a system may be described in terms of electron density, provides a greatly simplicity of the calculation, rather than wavefunction, that

depends on each electron and spin coordinates. This is the essence of the Kohn-Sham equations, which are a set of single-particle Schrödinger equations with an effective potential that relies on the electron density, yields the electron density. These equations are solved loopily, to achieve self-consistency it starts with an initial guess for the electron density. Once the first step has been determined the total energy of the system, can be calculated by assessing the functional of the electron density. These equations are similar to the Hartree equations excepting the Hamiltonian operator and the inclusion of term representing the exchange-correlation potential. The first exchange-correlation functional was based on the Local Density Approximation, LDA, which stands for the assumption that exchange-correlation energy depends only on the value of electronic density in each spatial point, stipulating that is locally constant, without considering its gradient. A premiss not actually correct for high and low electronic densities.

The wB97XD functional widely used in transition metal complexes studies, is the combination of two different functional a long-range corrected functional, wB97X, and the exchange-correlation functional, XDH describing accurately weak Van der Waals forces and intermolecular interactions, respectively [32, 46-49].

1.5.4. Basis Functions

The wave-like behaviour of electrons in molecules is described by basis functions, which are mathematical functions with an exponential behaviour, meaning that they describe exponentially the digression of electron and nucleus. Basis functions has two main types: STO (slater type orbital) and GTO (gaussian type orbital) that simplify the wave function by expressing the MO as LCAO [50].

STOs are mathematically resembling to the wave function of monoelectronic atoms. Is unconsidered to be accurate basis function for complex electron density distribution in many molecules. Opposing to GTOs that are similar to the Gaussian probability distribution. Although having a higher computational complexity, because the foundation is the decomposition of a Slater orbital in a linear combination of gaussian functions.

The basis function used in this work, belonging to the Pople basis set, is a double-zeta (double-ζ) type, when two function is applied to each atomic orbital. The Pople basis set consists of a split-valence basis which provides flexibility to the valence orbitals and a

single set of functions for the core. The 6-31G* consists in 6 gaussian primitives for each core orbital, 3 gaussian functions and 1 gaussian primitive that composes a linear combination each for the valence orbitals. The * denotation adds to 6-31G five d-types cartesian gaussian set of polarization functions. A type of function useful in a numerus electron's system, helping to describe the electron cloud distortion by adding a different angular moment to the basis set.

1.5.5. Effective Core Potentials

The ECPs method consists in the approximation of the frozen core electrons replacing them by a pseudopotential, a constant effective potential that provides a similar electron interaction with the valence orbitals. This outperforms the usage of large set of gaussians minimising the computational effort without sacrificing the calculations efficiency. On the opposite, ECPs doesn't account for the relativistic effects generated in atoms with a substantial atomic number. The use of Relativistic Effective Core Potentials (RECPs) can surpass the last problem by including the effects of electron-electron interactions, considered a better relativistic pseudopotential for calculations that require higher accuracy.in the RECPs parametrization, not only the relativistic effects spin independent and spin-orbital interaction ca be incorporated, but basis functions of density potentials also including diffuse and polarised functions can be added [51]. Throughout this work, the RECP LANL2DZ (Los Alamos National Laboratory 2 of Double Zeta) created by Hay and Wadt is used exclusively in the treatment of platinum and palladium atoms.[17, 52, 53]

1.5.6. Geometry Optimization and Frequency Calculations

MO calculus permits the achievement of energy values for different molecular conformations and harmonic vibrations frequencies, active in Raman and/or infrared spectroscopies. However, many types of energy minima can be achieved through a geometry optimization process. In other words, different potential energy surface stationary points, *i.e.* different minima (global or local) and saddle points can be reached. With the last step completed, the frequency calculations provide the thermodynamic parameters for each geometry in study.

1.6. The Methods

1.6.1. Viability Evaluation

The MTT (3-(4,5-Dimethylthiazol-2-yl)-2,5-Diphenyltetrazolium Bromide) is a colorimetric assay, one type of *in vitro* assays, and is used to study the cells' viability after drug exposure. Within the mitochondria, the yellow tetrazolium salt is reduced to purple formazan crystals by an enzyme designated succinate dehydrogenase, a process NADH dependent (Figure 7) which only happens in metabolically active cells[25, 40, 54].

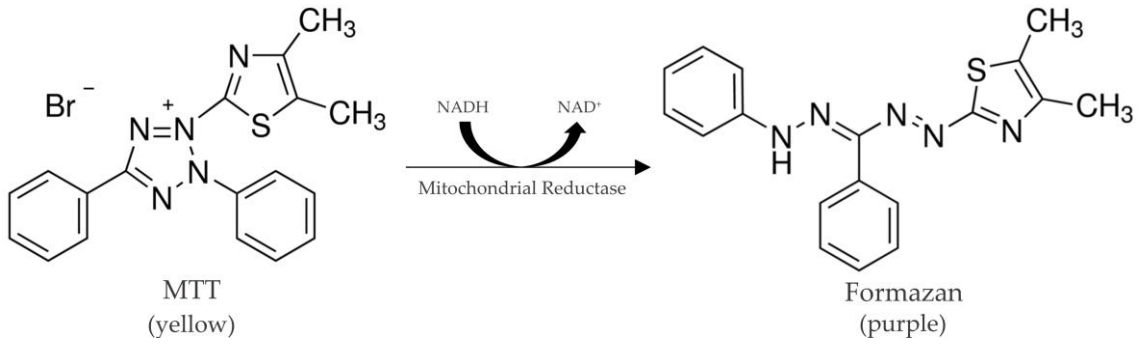

Figure 7: Structural representation of NADH reduction of MTT to Formazan.

1.6.2. Spectroscopy

Spectroscopy studies the interactions of electromagnetic radiation with matter, in which the interaction promotes transitions at the energy level, namely at the rotational, vibrational, and electronic levels. The energy involved transfers in discontinuous increments, whether absorbed or emitted. By the principle of equipartition of energy, the change in the energy of a system is given by the change in the energies of all its components, a relationship carried out in equation (5) in which it is considered that the electronic energy is constant:

$$\Delta E\,\text{sis} \simeq \Delta E\,\text{vib} + \Delta E\,\text{rot} + \Delta E\,\text{trans} \ldots \quad (5)$$

There are several types of energy transformation, the vibrational one being used for this work. Planck proposed that the energy of a given electromagnetic radiation is governed by specific energy values and that these do not vary arbitrarily. With this, Planck designated these energy limitations as being their quantization. Where for energy values allowed in an electromagnetic oscillator, υ corresponds to its respective frequency, integer

values of hυ would be obtained, where h was deduced by Planck, as the value that would provide a better fit, where h = 6.626x10^{-34} J.s. From the equation defined by it, equation (6), it is possible to quantify the energy difference between two certain energy levels [33, 41, 55].

$$E = h\upsilon \tag{6}$$

1.6.2.1. Vibrational Spectroscopy

The vibrational spectrum of a molecule depends not only on the mass of the atoms that constitute it but also on its spatial arrangement and strength of chemical bonds.

In the treatment of the vibrations of a molecule, the mechanical harmonic approximation can be considered, this approximation despite being crude, simplifies the treatment of the vibrations, being the harmonic potential close to the real potential profile close to the place of minimum energy. If the intention is to analyse the equilibrium geometries of molecules, this approach pays off by simplifying calculations and works reasonably well. In analysing the molecular vibrations of a diatomic molecule, it will be easier to interpret when considering it as two masses separated by a weightless elastic spring (Figure 8), by the elastic force constant, *k*, where each mode of vibration will have a wave number difference observable in the vibrational spectrum, this model is based on Hooke's law. A high force constant implies a harder deformation, hence a tighter bending of the oscillator. In this system, being defined by a harmonic oscillator, in which the spring constant force is related to the electronic characteristics of the system, for a displacement of Δr from the equilibrium position, the spring restoration force, *F*, is defined, following Newton's second law is deduced from Hooke's law, equation (7):

$$F = ma = \mu\frac{d^2r}{dt^2} = -f.\Delta r \tag{7}$$

Where the reduced mass obtained by equation (8) and the elastic force from the vibration frequency, equation (9):

$$\mu = \frac{m_1 m_2}{m_1 + m_2} \tag{8}$$

$$\nu = \frac{1}{2}\pi\sqrt{\frac{k}{\mu}} \tag{9}$$

In Figure 8 the harmonic oscillator is compared to the anharmonic oscillator being this the most correct to be considered for a diatomic molecule, this is because, in a harmonic oscillator, the dissociation of the molecule and the approximation of vibrational levels are not considered, due to its simplicity [55].

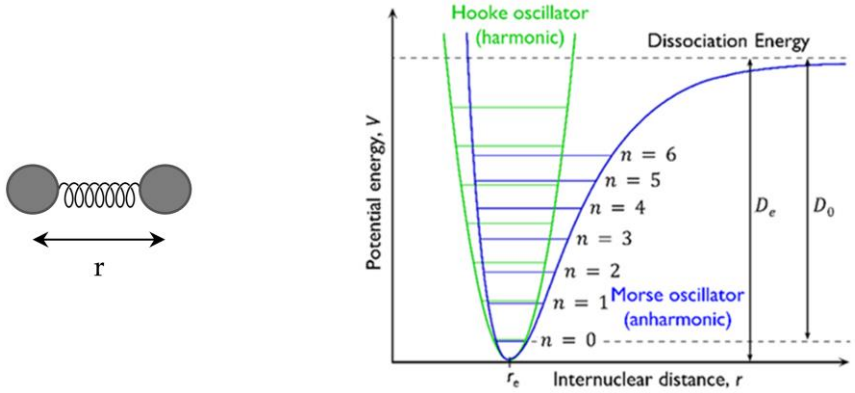

Figure 8: Schematic representation of the potential energy curve and energy levels corresponding to the Hooke model (harmonic oscillator) for a diatomic molecule *vs* the Morse model (anharmonic oscillator). (Adapted from [33])

The vibrational states of a diatomic molecule are more realistically defined by the anharmonic oscillator in equation (10):

$$V(r) = De[1 - \exp(-\beta\Delta r)]^2 \tag{10}$$

The energy for a given vibrational level is given by the expression (11), the first part of which is relative to the harmonic oscillator and the second to the anharmonic one.

$$E_n = h\nu\left(n+\frac{1}{2}\right) - h\nu k_{an}\left(n+\frac{1}{2}\right) \tag{11}$$

This relation is made, because the energy for the smallest energy level, n=0, is greater than the minimum of 1/2 hυ. In Figure 8, the dissociation energy, D_e, consists of the energy involved starting at zero energy up to the maximum energy at which dissociation occurs, whereas D_o, corresponds to the dissociation energy with the knowledge of the zero point of vibrational energy [33].

Through the classic treatment of molecular vibrations, in which it is defined that the total number of degrees of freedom of a molecule is 3*n*, where n is the total number of atoms that constitute it, both the translational and rotational components use each one with 3 degrees of freedom, according to Cartesian coordinates. For non-linear molecules, the number of vibrational degrees of freedom is given by 3*n*-6, and for linear ones 3*n*-5,

these being normal modes of vibration. A normal mode of vibration is a mode of vibration in which the centre of mass of the molecule is not changed, which leads to deformation both in length and in the angles established between chemical bonds, periodically [56].

1.6.2.1.1. Infrared Spectroscopy

In spectroscopic terms, if in each case there are two vibrations, one symmetric and the other antisymmetric, in the infrared the most intense band will correspond to the antisymmetric vibration because normally it is the one that causes a greater variation of the dipole moment. Thus, for a molecular vibration to be detected by infrared, there must be a change in the dipole moment, μ, in short, by analysing equation (12), the derivative of the dipole moment with the coordinate of the movement between the atoms involved in this vibration will have to be different from zero.

$$\left(\frac{\partial \mu}{\partial r}\right)_0 \neq 0 \tag{12}$$

The dipole moment can be defined as the sum of the charges and the relative distances of the atoms belonging to the molecule under study, equation (13):

$$\mu = \sum q_i r_i \tag{13}$$

In the electromagnetic spectrum, Figure 9, the infrared region can be divided into three zones, each corresponding to a range of specific wavenumber values:

(i) close (12800 cm^{-1} to 4000 cm^{-1}) where most overtones are found;

(ii) average (4000 cm^{-1} to 200 cm^{-1}) associated with the fundamental vibrations of the system and the fingerprint region that is unique for each molecule;

(iii) distant (200 cm^{-1} to 10 cm^{-1}) can also be used in rotational spectroscopy.

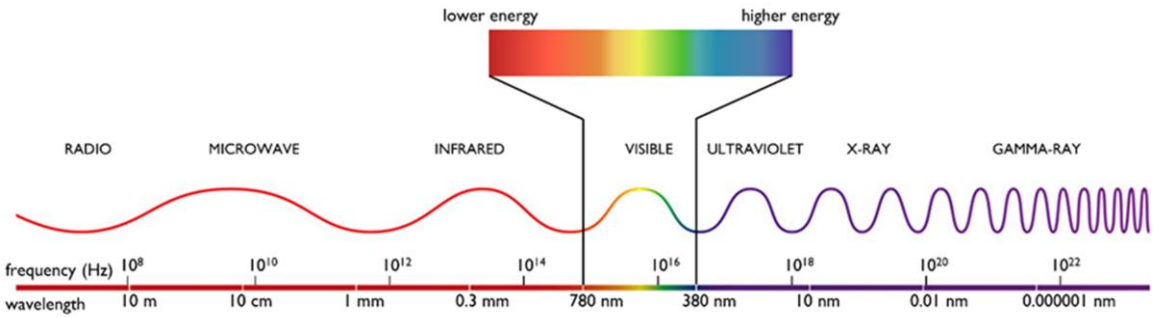

Figure 9: Schematic representation of the electromagnetic spectrum. (Adapted from [33])

The vibrations corresponding to the vibrational modes are observable and their energy is measurable through infrared spectroscopy [57]. In Figure 10, an energy diagram is represented, where the lowest, fundamental energy electron level, the corresponding transitional levels, and a representation of phenomena that can be used in infrared spectroscopy are shown [33].

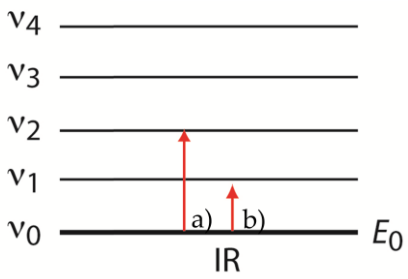

Figure 10: Energy diagram with transitions that occur in the infrared region.

As it can be seen in Figure 10, transition a) is a fundamental transition and b) an overtone. These transitions occur due to the absorption of infrared radiation, directly. Comparing the transitions, the most intense are the transitions of type a), and those that are normally analysed in an infrared spectrum. By the Bohr condition, a transition between two vibrational states occurs when there is the absorption of a photon containing exactly the energy necessary for the transition.

In qualitative terms, it is possible to state that the greater the variation in the polarity of a bond during the vibration, the greater its sign. If the dipole moment varies substantially, it will correspond to a band of high intensity, if it does not vary, a band will not be observed [33, 55].

The two sampling modes used in this work are reflectance and transmittance. In the reflection mode, the absorption properties of the sample can be extracted by reflected light. In transmission, a more conventional method, quantification is more direct than in other samplings, detection is carried out by the radiation passing through the sample, in this case, the Beer-Lambert Law can be applied to transform the spectrum signal into absorbance if the purpose is quantitative analytical determinations [56].

The coupling of synchrotron radiation (SR) as a photon source to the FTIR, allows a substantial improvement of a special resolution, in the mid-infrared spectral region, providing a more chemical detailed spectrum [58]. The SR-FTIR experiments were carried out in the Multimode InfraRed Imaging And Microspectroscopy beamline B22 (MIRIAM)

at the Diamond Light Source (DLS) of the Harwell Science and Innovation Campus, (Science and Technology Facilities Council (STFC), UK [59].

1.6.2.1.1.1. Fourier Transform Infrared

The acronym FTIR corresponds to Fourier-Transform Infrared Spectroscopy. Fourier-Transform Infrared, this consists of converting a periodic function in space-time, equation (14), into a series of signals/pulses in frequency space, equation (15):

$$f(t) = \frac{1}{2\pi}\int_{-\infty}^{\infty} F(\omega)e^{i\omega t}\,d\omega \tag{14}$$

$$F(\omega) = \frac{1}{2\pi}\int_{-\infty}^{\infty} f(t)e^{-i\omega t}\,dt \tag{15}$$

This relationship dictates that any signal can be decomposed as a sum of periodic contributions, improving the signal-to-noise ratio, S/N [57].

1.6.2.1.2. Raman Spectroscopy

The fundamental of Raman spectroscopy relies on the inelastic scattering of the light from an incident monochromatic radiation, when the matter is irradiated. This incident radiation can be scattered in two diverse ways upon interaction with a molecule, Rayleigh scattering and Raman scattering. The characteristics that differentiate them consist of the difference in the variance of energy of the emitted and absorbed photons. In Rayleigh scattering the energy of both photons is equal, when energy is given to the molecule it can maintain its original frequency. In both types of Raman scattering, Stokes or anti-Stokes (Figure 11), the photons have different energies, meaning the laser's light and the scattered light have different frequencies. If the final vibrational state is more energetic then the ground state, a red-shift occurs, while with anti-Stokes a blue-shift of the scattered light occurs. The intensity of the Stokes bands is significantly stronger than the anti-Stokes signals, as a consequence of the Boltzmann distribution within the vibrational states of the molecule, the population of ground state being much lower than that of the excited states. The scattering process always involves two photons, the incident and the emitted, and since it is an inelastic process it involves three types of states: initial, final, and non-stationary state, physically non-observed designated as a virtual state. In contrast to absorption and emission, a single photon process has the initial and final state [60].

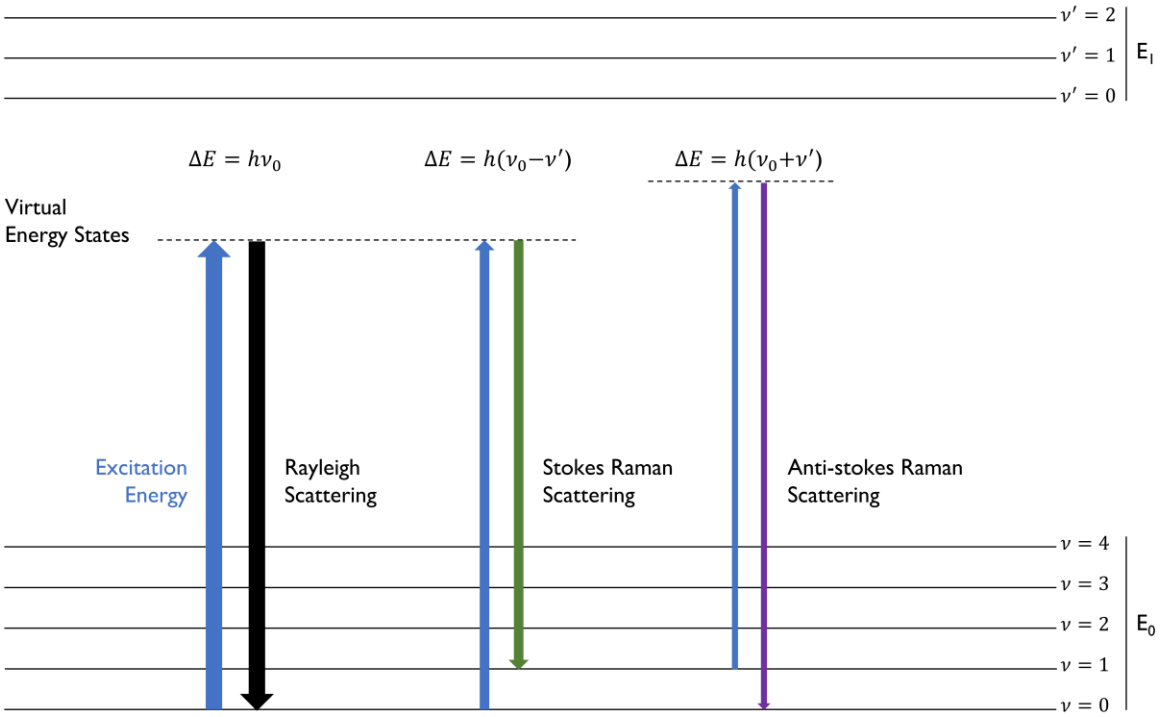

Figure 11: Schematic representation of the energy-level diagram with the different states involved in Raman Spectroscopy. (Adapted from [33])

As a way for a molecular vibration to be active in Raman, an alteration of the polarizability, α, of the molecule may occur (as a deformity of the electronic cloud), calculated by the derivative of α, .in relation to the rearrangement of r coordinate of the vibrational mode, equation (16). In other words, when the derivative below is different from zero, the vibration is active in Raman.

$$\left(\frac{\partial \alpha}{\partial \mathrm{r}}\right)_0 \neq 0 \tag{16}$$

The intensity of the bands in terms of polarizability change can be explained by a selection of rules defined by the classical theory of Raman scattering. It can explain the uncomplicated impact that an electric field, in a form of incident radiation, has upon an electronic cloud of a molecule, inducing a dipole moment. Considering a vector, $\vec{\mu}$,this result can be obtained by multiplying the polarizability, α, and the electric field vector, $\vec{E}$, equation (17):

$$\vec{\mu} = \alpha \vec{E} \tag{17}$$

1.6.2.2. Vibrational Microspectroscopy

The coupling of microscopy to infrared and Raman spectroscopies is used in the analysis of complex tissues, cell lines and heterogeneous samples, *in situ* and non-destructive analysis of the biological components under analysis, in the distinction of benign and malignant tumours, in obtaining images and in a large number of spectra from specific analysis sites, among other factors, allows a better understanding at the biological and chemical level, by enhancing spatial resolution and sensitivity [57, 61-65].

2. Experimental

2.1. Reagents and Material

Table 1: List of reagents, material, equipment, and software used in the present work.

Reagents	
Acetic acid glacial (99.7%)	Merck KGaA, Sintra, PT
Acetone (≥ 95%)	Merck KGaA, Sintra, PT
Hydrochloric acid (37%)	Merck KGaA, Sintra, PT
Crystal Violet (≥ 90.0%)	Merck KGaA, Sintra, PT
cis-dichlorodiammine platinum(II) (cisplatin) (99.9%)	Merck KGaA, Sintra, PT
cis-dichlorodiammine palladium(II) (cispalladium)	Merck KGaA, Sintra, PT
Dimethyl sulfoxide (DMSO) (≥ 99%)	Merck KGaA, Sintra, PT
Doxorubicin	Merck KGaA, Sintra, PT
HBSS (Hanks' balanced salt solution)	Merck KGaA, Sintra, PT
Minimum Essential Medium – High Glucose (EMEM/NEAA) (with Earle's Balance salts, 2.0 mM L-glutamine and NEAA without sodium bicarbonate)	Merck KGaA, Sintra, PT
MEM Non-essential Amino acid solution (100x) (without L-glutamine, liquid, sterile filtered, BioReagents, suitable for cell culture)	Merck KGaA, Sintra, PT
Ethanol (99.8%)	Merck KGaA, Sintra, PT
Ethylenediaminetetraacetic acid (EDTA) (≥ 98.5%)	Merck KGaA, Sintra, PT
Fetal Bovine Serum (FBS) (EU Approved (South American))	Gibco-Life Technologies, Porto, PT
Formalin solution, neutral-buffered, 10%	Merck KGaA, Sintra, PT
Methanol (≥ 99.8%)	Merck KGaA, Sintra, PT
Methotrexate	Merck KGaA, Sintra, PT
Osteoblast Growth Medium	Merck KGaA, Sintra, PT
Palladium(II) chloride (99.9%)	Merck KGaA, Sintra, PT
Penicillin-Streptomycin solution (Pen/Strep) (10,000 units penicillin and 10 mg streptomycin/mL)	Merck KGaA, Sintra, PT
Potassium bromide, (FTIR grade, ≥ 99%)	Merck KGaA, Sintra, PT

Potassium chloride	Merck KGaA, Sintra, PT
Potassium phosphate monobasic (≥ 99.0%)	Merck KGaA, Sintra, PT
Potassium tetrachloropalladate(II) (98%)	Merck KGaA, Sintra, PT
Potassium tetrachloroplatinate(II) (98%)	Merck KGaA, Sintra, PT
Putrescine (≥97%)	Merck KGaA, Sintra, PT
Quercetin (≥ 95%)	Merck KGaA, Sintra, PT
Sodium bicarbonate (≥ 99.7%)	Merck KGaA, Sintra, PT
Sodium chloride (99.0%)	Merck KGaA, Sintra, PT
Sodium hydroxide	Merck KGaA, Sintra, PT
Sodium phosphate dibasic (≥ 99.0%)	Merck KGaA, Sintra, PT
Sodium pyruvate	Merck KGaA, Sintra, PT
Spermine (97%)	Merck KGaA, Sintra, PT
Spermidine (≥ 99.0%)	Merck KGaA, Sintra, PT
Trypan Blue (0.4% (*w*/*v*) solution)	Merck KGaA, Sintra, PT
Trypsin (10x solution, 25 g porcine trypsin *per* litre in 0.9% sodium chloride)	Merck KGaA, Sintra, PT
3-(4,5-dimethylthiazol-2-yl)-2,5-diphenyltetrazolium Bromide	Merck KGaA, Sintra, PT
Material	
12 wells plates	OrangeScientific, Frilabo, PT
24 wells plates	OrangeScientific, Frilabo, PT
48 wells plates	OrangeScientific, Frilabo, PT
96 wells plates	OrangeScientific, Frilabo, PT
T 75 cm^2 culture flasks	OrangeScientific, Frilabo, PT
T 182 cm^2 culture flasks	OrangeScientific, Frilabo, PT
15 and 50 mL conic tubes	OrangeScientific, Frilabo, PT
1.5 and 2 mL micro-tubes	OrangeScientific, Frilabo, PT
5, 10 and 25 mL pipettes	OrangeScientific, Frilabo, PT
5, 10 and 20 mL syringes	BD Falcon, Enzifarma, PT
0.80 x 120 mm needles	Sterican, Braun, PT
MgF_2 (2x20 mm) windows	Crystran, UK

CaF_2 (IR-grade, 1x13 mm) windows	Crystran, UK
CaF_2 (UV-grade, 1x13 mm) windows	Crystran, UK
Q-Max syringe filters	OrangeScientific, Frilabo, PT
Main Equipment	
Analytical balance (Toledo AB54)	Mettler, Rotoquímica, PT
pH-meter (Basic 20 +)	Crison, Rotoquímica, PT
Shaker "Vortex" (MS2 Minishaker)	IKA® Works, Frilabo, PT
Water purification apparatus Milli –Q (Gen Pure)	TKA, Frilabo, PT
Centrifuge with cooling (MPW-350R)	MPW, Frilabo, PT
Incubator MCO-19AIC (UV)	Sanyo, Frilabo, PT
Laminar flow hood (BW 100) (flow rate : 1050m^3/h)	BioWizard, Frilabo, PT
Microplate reader μQuant MQX200	BioTek, PT
Microscope CRX41 coupled to a DP20 camera	Olympus®, PT
Senterra dispersive Raman microspectrometer with a charge-coupled device (CCD) detector	Bruker, UK
Infrared beamline B22 (MIRIAM – Multimode InfraRed Imaging And Microspectroscopy) – Vertex 80v FTIR spectrometer, Hyperion 3000 microscope	Diamond Light Source, UK
Vertex 70 FTIR spectrometer	Bruker, PT
Software	
Gaussian 16w	Gaussian Inc., Wallingford, USA
GaussView 6.0	Gaussian Inc., Wallingford, USA
GraphPad Prism 8	La Jolla, CA, USA
Matlab 2020b	The MathWorks Inc., Natick, MA
OPUS 9.1	Bruker Optik, DE
OriginPro 9.1	OriginLab, USA
Quasar 16.0	Orange, SI
Gen5 1.11	Agilent BioTek, USA

2.2. Experimental Methods

2.2.1. Synthesis of Metal Complexes with Polyamines

2.2.1.1. $Pd_3Spd_2Cl_6$

K_2PdCl_4 (1 mmol, 326.4 mg) was dissolved in the minimum volume of distilled water and spermidine (0.66 mmol, 104 μL) was added in agitation for 15 minutes, a beige compound was revealed. The solution was filtrate, and the precipitate was left drying after being washed with distilled water, ethanol, and ketone.(yield 65.5%). The reaction was prepared according with Navarro-Ranninger *et al* [35].

2.2.1.2. $Pt_3Spd_2Cl_6$

K_2PtCl_4 (1.5 mmol, 623.0.mg) was dissolved in 3 mL of distilled water and spermidine (1 mmol, 157 μL) was added in agitation for 24 hours, a brown compound was revealed. The solution was filtrate, and the precipitate was left drying after being washed with distilled water, and ethyl ether yielding 72.4%. The reaction was prepared according to Navarro-Ranninger *et al* [66].

2.2.1.3. $Pd_2Put_2Cl_4$

Pd_2Cl_4 (2.76 mmol, 487.7.mg) was dissolved in 2.5 mL of methanol and putrescine dihydrochloride (2.76 mmol, 443.0.mg) was dissolved in 1.25 mL of methanol. Both were mixes added in agitation for 96 hours, a yellow dark compound was revealed. The solution was filtrate, and the precipitate was left drying after being washed with a solution of 6 M hydrochloric acid, distilled water, and ethyl ether (yield 51.7%). The reaction was prepared according to an optimisation with Navarro-Ranninger *et al* [67].

2.2.1.4. $Pt_2Put_2(NH_3)_4^{4+}$

Cisplatin (2 mmol, 600 mg) was dissolved in distilled water and putrescine (2 mmol, 200 μL) was added slowly in agitation at 60 °C for 1.5 hours. The solution was filtered, evaporated to approximately 1 mL, and left for 48 h at 4 °C. The white precipitate was

isolated by filtration and washed two times with ethanol (yield 11.5%). The reaction was prepared according to an optimisation with Farrell *et al* [68].

2.2.2. Preparation of Solutions

Table 2: Solutions used in the experimental work.

Solution	Components	pH	Storage
Cell culture			
Phosphate Buffered Saline (PBS) 10x	2.0 g KH_2PO_4 (15 mM) 6.1 g Na_2HPO_4 (43 mM) 2.0 g KCl (27 mM) 87.7 g NaCl (1.5 M) 1000.0 mL ultrapure water	7.4	Room temperature
PBS 1x	100.0 mL PBS 10x 900.0 mL ultrapure water	7.4	Room temperature
MEM	9.61 g MEM 2.5 g $NaHCO_3$ 1000.0 mL (final volume) ultrapure water	7.0	4 °C
MEM 10% (*v*/*v*) FBS, 1% Pen/Strep, 1% Non-essential Amino acid and 1%sodium pyruvate	890.0 mL MEM 100.0 mL FBS 10.0 mL Pen/Strep 10.0 mL Non-essential Amino acid solution 10.0 ml sodium pyruvate	7.0	4 °C
Trypsin-EDTA 1x	90.0 mL PBS 1x 10.0 mL Trypsin 10 x 20.0 mg EDTA	7.4	4 °C
Trypsin. Inhibitor	95.0 mL HBSS 5.0 mL FBS	7.4	4 °C
Tested agents			
Cisplatin 1 mM	3.0 mg cisplatin 10.0 mL PBS 1x	-	-20 °C
Pd_2SpmCl_4 500 μM	2.8 mg Pd_2SpmCl_4 9.0 mL PBS 1x 1.0 mL DMSO	-	-20 °C
$Pt_3Spd_2Cl_6$ 3 mM	30.4 mg $Pt_3Spd_2Cl_6$ 9.0 mL PBS 1x 1.0 mL DMSO	-	-20 °C

$Pd_3Spd_2Cl_6$ 1.7 mM	14.0 mg $Pd_3Spd_2Cl_6$ 9.0 mL PBS 1x 1.0 mL DMSO	-	-20 °C
$Pd_2Put_2Cl_4$ 3 mM	15.8 mg $Pd_2Put_2Cl_4$ 9.0 mL PBS 1x 1.0 mL DMSO	-	-20 °C
$Pt_2Put_2(NH_3)_4Cl_4$ 2.5 mM	18.9 mg $Pt_2Put_2(NH_3)_4Cl_4$ 10.0 mL PBS 0.8x	-	-20 °C
Doxorubicin 3 mM	16.3 mg Doxorubicin 10.0 mL ultrapure water	-	-20 °C
Methotrexate 1.44 mM	6.5 mg Methotrexate 10.0 mL PBS 1x	-	-20 °C
MTT colorimetric assay			
MTT 0.5 mg/mL	15 mg MTT 30 mL ultrapure water	-	-20 °C
Spectroscopic experiments			
Sodium chloride 0.9%	9.0 g Sodium chloride 1000 mL ultrapure water	7.4	Room temperature
Formalin 4%	40.0 mL 60.0 mL ultrapure water	-	-20 °C

2.2.3. Characterization of the Complexes

2.2.3.1. FTIR-ATR Spectroscopy

FTIR acquisitions were performed using a Bruker Optics Vertex 70 spectrometer with a liquid nitrogen-cooled mercury-cadmium-telluride (MCT) detector for mid-infrared (400 – 4000 cm^{-1}) and for far-infrared (40 – 600 cm^{-1}) a deuterated triglycine sulphate (DTGS) detector, purged by CO_2-free dry air. Each spectrum was the sum of 128 scans, at 2 cm^{-1} resolution.

2.2.3.2. Raman Spectroscopy

Raman microspectroscopy acquisition was performed using a WITec confocal Raman microscopy system Alpha 300 R coupled to an ultra-high-throughput spectrometer (UHTS) 300 VIS-NIR, using a CDD (charged-coupled device) detector and a diode laser of 785 nm as excitation font. The laser power on the sample was kept at 16 mW and the

measurements were achieved using a 10× Zeiss Epiplan objective with 30 accumulations of 30 s for $Pt_2Put_2(NH_3)_4Cl_4$, and 5 accumulations of 30 s per spectrum for the other complexes.

2.2.3.3. Computational Methods

Quantum mechanical calculations were performed for $Pd_3Spd_2Cl_6$, $Pt_3Spd_2Cl_6$ $Pd_2Put_2Cl_4$ and $Pt_2Put_2(NH_3)_4Cl_4$, using the Gaussian 16W program. Both geometry optimisation and calculation of the harmonic vibrational frequencies, within the Density Functional Theory (DFT) approach, at a level which was previously shown by the authors to be the best choice for describing this type of Pd(II)/Pt(II)-biogenic polyamine complexes, since it presents the finest compromise between accuracy and computational demands. The wB97XD functional was used, along with the split valence basis set 6-31G*, for all atoms except for the metal. Pd(II) and Pt(II) were represented by the relativistic Effective Core Potentials of Hay and Wadt (G16W keyword LANL2DZ).

The harmonic vibrational wavenumbers, as well as Raman activities and infrared intensities, were obtained at the same theory level as the geometry optimisation procedure.

2.2.4. *In vitro* Assay

2.2.4.1. Cell Culture

The osteosarcoma cell line (MG-63) and non-tumorigenic (HOb) cell lines were obtained from the ECCAC Culture Collections and supplied by Merck KGaA (Sintra, Portugal). They were cultured as monolayers, at 37 °C, in a humidified atmosphere of 5% CO_2. The MG-63 cultures were maintained in MEM culture medium, supplemented with 10% (v/v) heat-inactivated FBS, 1% (v/v) penicillin/streptomycin, 1% (v/v) non-essential Amino acid solution and 1% (v/v) sodium pyruvate 1M solution. The HOb cultures were maintained in Osteoblast Growth Medium. The MG-63 and HOb cells were subcultured at 80% confluence, using 0.05% trypsin-EDTA (1×) in PBS [69, 70]. Differently from the trypsin inactivation for the MG-63 cell line that is proceed by the addiction of MEM culture

medium, for the HOb cell line is added a trypsin neutralizing solution to inhibit the trypsin's effect.

2.2.4.2. Evaluation of Cells' Viability

For both cell lines, cell cultures were established in 96-well plates (100 μL/well) at a density of 3×10^4 cells/cm^2 for MG-63 and 1.6×10^4 cells/cm^2 for HOb, and were allowed to attach for 24 h. Triplicates were treated for different incubation periods (three independent experiments) with a range of concentrations between 5.31 and 170 μM of $Pd_3Spd_2Cl_6$, 3.91 and 250 μM of $Pt_2Put_2(NH_3)_4^{4+}$, 18.3 and 300 μM of $Pt_3Spd_2Cl_6$ and $Pd_2Put_2Cl_4$, in single-drug administration for MG-63 cell line. According to the population doubling time for all cell lines (*c.a.* 24 h), 24, 48, and 72 h time points after drug administration were chosen. For the HOb cell line, for single-drug administration, the triplicates were treated with the IC_{50} determined for the MG-63 cell line at 48h. The concentrations chosen regarding the combined administration were the same for both cell lines (MG-63 and HOb), they were selected according to the EURAMOS-1 protocol: cisplatin (4.8 μM), DOX (4.8 μM) and MTX (3 μM), the concentrations of the new designed drugs were the same as the one stipulated for cisplatin. At 0h, the MG-63 cell line was expose to $Pd_3Spd_2Cl_6$, $Pt_2Put_2(NH_3)_4^{4+}$, $Pt_3Spd_2Cl_6$ and $Pd_2Put_2Cl_4$ all with DOX, incubating for 24, 48, 72 and 96h followed by the MTT assay (Figure 12 (A)). At the 72h time point, MTX was administrated and incubated for more 24 h. For the HOb cells, cisplatin, Pd_2SpmCl_4 and $Pd_3Spd_2Cl_6$ with DOX were administrated, 72 h later the MTX was added and at the 96 h time point the cells' viability was assessed by the MTT assay (Figure 12(B)).

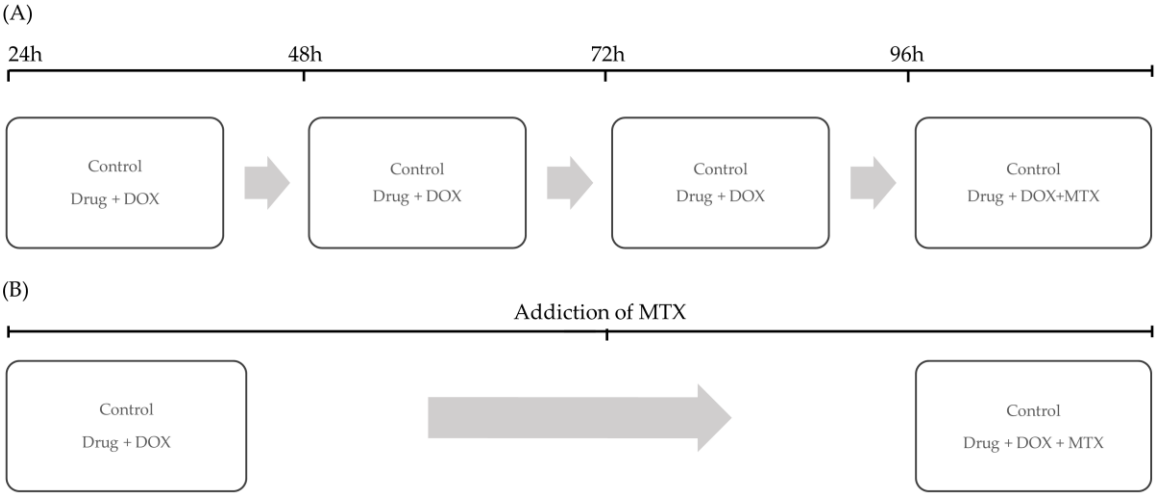

Figure 12: Experimental workflow for (A) single administration and (B) combined administration assays.

In order to evaluate cell viability, the MTT assay was used. Briefly, at each time-point, the growth media was removed, cells were washed with PBS and MTT solution (2.5 mg/mL) was added to each well (100 μL). After 3 h of incubation at 37 °C, the formazan crystals were solubilized in DMSO (100 μL), and the absorbance was measured at 570 nm.

2.2.5. Sample Preparation for Spectroscopy Analysis

Upon harvesting by trypsinization, MG-63 and HOb cell lines were centrifuged, and the pellet was resuspended in culture medium and seeded, at a concentration of 3×10^4 cells/cm^2 for MG-63 and 1.6×10^4 cells/cm^2 for HOb, on optical substrates suitable for either FTIR or Raman data collection, respectively, CaF_2 disks (Crystran UV-grade, 1 mm × 13 mm) or MgF_2 disks (Crystran Raman-grade, 1 mm × 13 mm), which were previously washed with 70% ethanol. After incubation for 24 h (allowing the cells to adhere), each of the tested single-drugs were added according to the respective 50% cell growth inhibition values (IC_{50}) for each cell line, and the cells were allowed to culture for a further 48 h. The samples tested with the combinations were incubated for 96h with each corresponding Pt/Pd drug in combination with DOX, and at 72 h after these two drugs combination exposure the MTX was added. The growth medium was then removed, the cells were washed twice with PBS 1x, fixed in 4% formalin (diluted in 0.9% ultrapure water from the commercial neutral buffered formaldehyde solution) for 10 min, and washed several times with deionized water (to remove any residual salt). The disks were allowed to air-dry prior to spectroscopic analysis.

All samples were prepared in duplicate, in two independent experiments.

2.2.6. Optical Vibrational Microspectroscopy

2.2.6.1. FTIR Microspectroscopy

FTIR acquisitions were carried out at B22 (MIRIAM) at Diamond Light Source (UK) using a Bruker Hyperion 3000 microscope with a liquid nitrogen-cooled mercury-cadmium-telluride (MCT) detector, in transmission mode using a 15× Cassegrain both condenser and objective, coupled to a Bruker Optics Vertex 80 spectrometer, both evacuated. In order to obtain more accurate spectral data from the whole cell, a slit size of

20x20 μm^2 was used and, depending on cell size and shape, several spectra where acquired, varying from 1 to 6 spectra for each cell, at 4 cm^{-1} spectral resolution and a sum of 128 scans *per* cell. Background was measured every 10 spectra.

2.2.6.2. Raman Microspectroscopy

Raman microspectroscopy acquisition was performed using a WITec confocal Raman microscopy system Alpha 300 R coupled to an ultra-high-throughput spectrometer (UHTS) 300 VIS-NIR, using a 532 nm diode-pumped solid-state laser. The laser power on the sample was kept at 16 mW and the measurements were achieved using a 100×/0.8 Zeiss Epiplan objective with 5 accumulations of 10 s per spectrum for MG-63 cell line control and single-drug treated, and 5 accumulations of 20 s per spectrum for HOb cell line and MG-63 cell line treated with the combinations.

2.2.7. Data Analysis

2.2.7.1. Statistical Analysis

Cells viability data results are expressed as mean ± standard deviation (SD) and compared with non-treated controls. Statistical analysis was carried out through one-way ANOVA followed by Dunnett's multiple comparison test. A p-value < 0.05 was considered statistically significant.

2.2.7.2. Data Pre-processing and Fitting Procedures

Synchrotron-microFTIR data acquisition was performed using OPUS 9.1 software. A Blackman-Harris 4-term apodization function was applied during the FT-processing, using a zero-filling factor of 2 and a Maths phase correction to yield a spectral data point spacing of 2 cm^{-1}. Infrared transmission spectra were obtained by rationing to a background measured from a clean area of the sample substrate (where no cells were present). To the microFTIR spectral data a data binning was performed for each cell which corresponds to the average of the spectra taken. The quality of the spectra was assessed based on the intensity of the amide I band. The spectra were corrected for Mie scattering

using the method created by J. Sulé-Suso and A. Kohler [71, 72]. The analysed spectra were truncated from 1050 cm^{-1} to 1800 cm^{-1} and vector normalized.

The microRaman spectral data were obtained using the Project FIVE software (WITec). In order to reduce the spectral noise, principal component noise removal was performed, retaining the first 20 principal components. The spectral data were cropped to the fingerprint region, 600 – 1800 cm^{-1}, and further corrected for cosmic ray removal, Savitzky–Golay smooth filtered (window width of 7 points), back-ground subtraction (polynomial order fitting of 2nd order), normalization and PCA denoising with 15 components.

Spectra were then cropped to the spectral ranges 1050 – 1800 cm^{-1} for microFTIR and 600 – 1800 cm^{-1} for microRaman, followed by multivariate analysis of the results – unsupervised PCA (principal component analysis) which was carried out (separately for each technique used) with standard singular value decomposition of the data. The order of the principal components (PC) denoted their importance in relation to the data set variance, PC1 corresponding to the highest variance present in the data. The data pre-processing and analysis was performed using the Quasar Spectroscopy 1.6.0 software [71, 72].

3. Results and Discussion

3.1. Characterisation of the Complexes

3.1.1. $Pd_3Spd_2Cl_6$

The most stable geometry calculated for the $Pd_3Spd_2Cl_6$ chelate (Figure 13) (Appendix A, Figure A1, Tables A1 and A2) corresponds to a C_2 symmetry, displaying 195 vibrational modes, 98 with A symmetry and 97 with B symmetry, all infrared and Raman active.

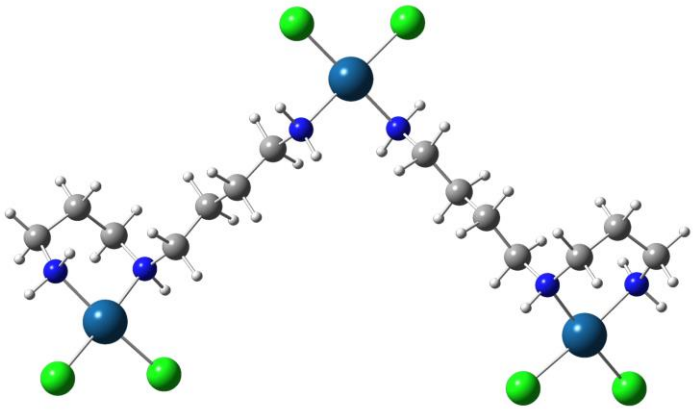

Figure 13: Structural representation of $Pd_3Spd_2Cl_6$.

The vibrational spectra obtained for $Pd_3Spd_2Cl_6$ (FTIR and Raman) both experimental and theorical are comprised in Figure 14, allowing access to a more detailed assignment of the experimental vibrational profile, described in Table 3.

The use of computational calculations allowed an interpretation of the experimental results obtained through Raman and ATR-FTIR where a good agreement between theoretical and experimental was found. The scaling of the calculated values is used to correct the known overestimation of the calculated harmonic vibrational frequencies due to the neglect of anharmonicity effects in the theoretical treatment [73].

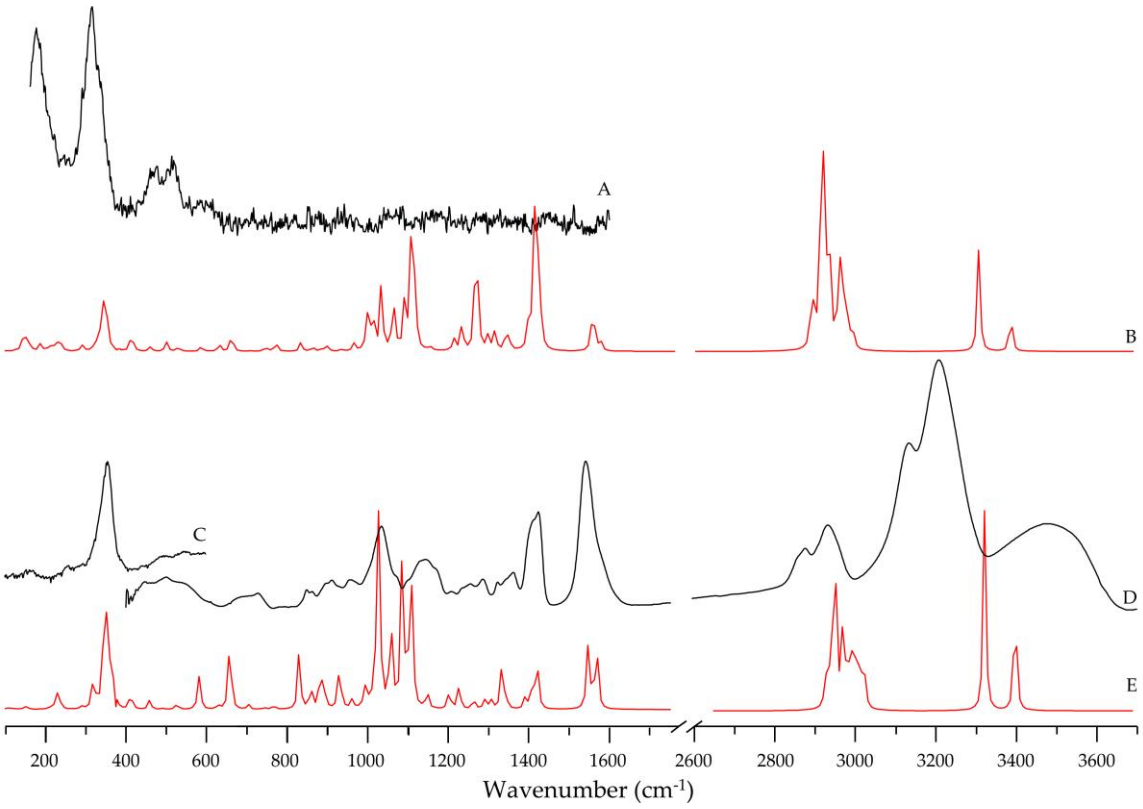

Figure 14: Vibrational spectra (100 – 1800 cm^{-1} and 2600 – 3700 cm^{-1}) for $Pd_3Spd_2Cl_6$: experimental (A) and calculated (B) Raman; experimental (C) FIR and (D) MIR and calculated (E), FTIR.

A special attention was given to bands that indicate metal coordination mainly through the characteristic Cl–Pd–Cl, N–Pd–N and N–Pd–Cl deformation and stretching bands, such as 545 cm^{-1}, 504 cm^{-1}, 418 cm^{-1}, 417 cm^{-1}, 379 cm^{-1}, 330 cm^{-1}, 327 cm^{-1}, 305 cm^{-1} and 166 cm^{-1} obtained from FTIR and Raman experimental results.

Table 3: Experimental and calculated vibrational wavenumbers (cm^{-1}) for $Pd_3Spd_2Cl_6$.

[b]Approximate description	Experimental		[a]Calculated	Sym. Species
	FTIR	Raman		
δN–Pd–Cl		166	160	B
ν_{as}Cl–Pd–Cl		305	335	B
ν_{as}Cl–Pd–Cl	327		322	B
ν_{s}Cl–Pd–Cl	330		346	A
ν_{s}Cl–Pd–Cl		379	350	A
δC–C–C		402	411	A
νPd–N	417	418	440	A
δC–C–N	504	473	492	A
ν_{s}Pd–N		504	535	A
δN–C–C + ν_{s}Pd–N	545		566	A
$\rho NH_{2(central)}$	699		669	A

$\rho CH_{2(chains)}$	738		719	A
$\rho CH_{2(rings)} + \tau NH_2 + \nu C{-}C_{(rings)} + \nu C{-}N_{(rings)}$	865		849	B
$\rho CH_2 + \omega NH_{2(rings)} + \tau NH_{2(central)}$	879		879	A
$\rho CH_{2(rings)} + \tau CH_{2(chains)} + \tau NH_{2(central)} + \gamma NH$	912		904	A
$\rho CH_{2(rings)}$	927		917	B
$\nu C{-}C + \nu C{-}N + \gamma NH$	975		953	B
$\omega NH + \nu C{-}C + \nu C{-}N_{(rings)}$	1057		1054	A
$\omega NH_{2(central)} + \nu C{-}NH{-}C$	1173		1114; 1139	A
$\tau CH_2 + \omega CH_2 + \tau NH_{2(central)}$	1238		1234	A
$\tau CH_{2(rings)}$	1286		1258	A
$\omega CH_{2(chains)}$	1318		1324	B
ωCH_2	1354		1368	A
$\omega CH_{2(rings)}$	1396		1381	A
$\delta NH + \alpha CH_{2(rings)}$	1445		1450	B
αCH_2	1462		1462	A
$\alpha NH_{2(chain)}$; $\alpha NH_{2(rings)}$	1581		1589; 1612	B
$\nu_s CH_{2(chains)}$	2880		2891	B
$\nu_s CH_{2(rings)}$	2936		2919; 2937	B
$\nu_{as} CH_2$	3133		2950; 2998	B
$\nu NH + \nu_s NH_2$	3211		3312	A
$\nu_{as} NH_2$	3482		3396	B

[a]At the wB97XD level. Scaled according to: 0.9475 for the bands in the 500 – 3700 cm^{-1} range; [b]Symbols for vibrational modes: ν stretching, α – scissoring, δ – in-plane deformation, τ – twisting, ρ – rocking, ω – wagging, γ – out-of-plane deformation, s, as, and a refer to symmetric, antisymmetric and asymmetric modes.

A blue shift was detected for the NH_2 asymmetric stretching and CH_2 asymmetric and symmetric stretching, occurring at 3482 cm^{-1}, 3133 cm^{-1} and 2880 – 2936 cm^{-1}, relative to the free spermidine ligand (Appendix B, Figure B1) at 3356 cm^{-1}, 2929 cm^{-1} and 2852 cm^{-1}, respectively. The bands corresponding to NH_2 symmetric stretching – 3211 cm^{-1}, NH_2 – 1581 cm^{-1} and CH_2 – 1445 – 1462 cm^{-1} scissoring modes, appeared shifted to lower frequencies when comparing to the ligand spectra, 3274 cm^{-1}, 1600 cm^{-1}, 1470 cm^{-1}, respectively. These observed changes were due to the metal chelate effect, proving metal-ligand coordination.

3.1.2. $Pt_3Spd_2Cl_6$

Like the $Pd_3Spd_2Cl_6$, the most stable geometry for the $Pt_3Spd_2Cl_6$ chelate (Figure 15) (Appendix A, Figure A2, Tables A3 and A4) agrees with a C_2 symmetry, and displays 195

vibrational modes, 98 with A symmetry and 97 with B symmetry, all infrared and Raman active.

The vibrational spectra obtained for $Pt_3Spd_2Cl_6$ (FTIR and Raman) both experimental and theorical are comprised in Figure 16, allowing access to a more detailed assignment of the experimental vibrational profile, described in Table 4.

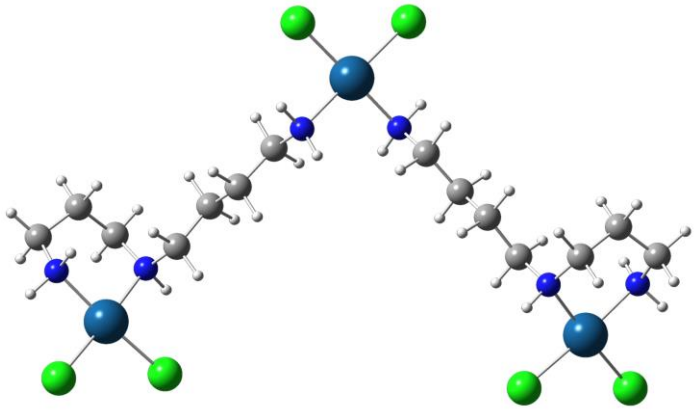

Figure 15: Structural representation of $Pt_3Spd_2Cl_6$

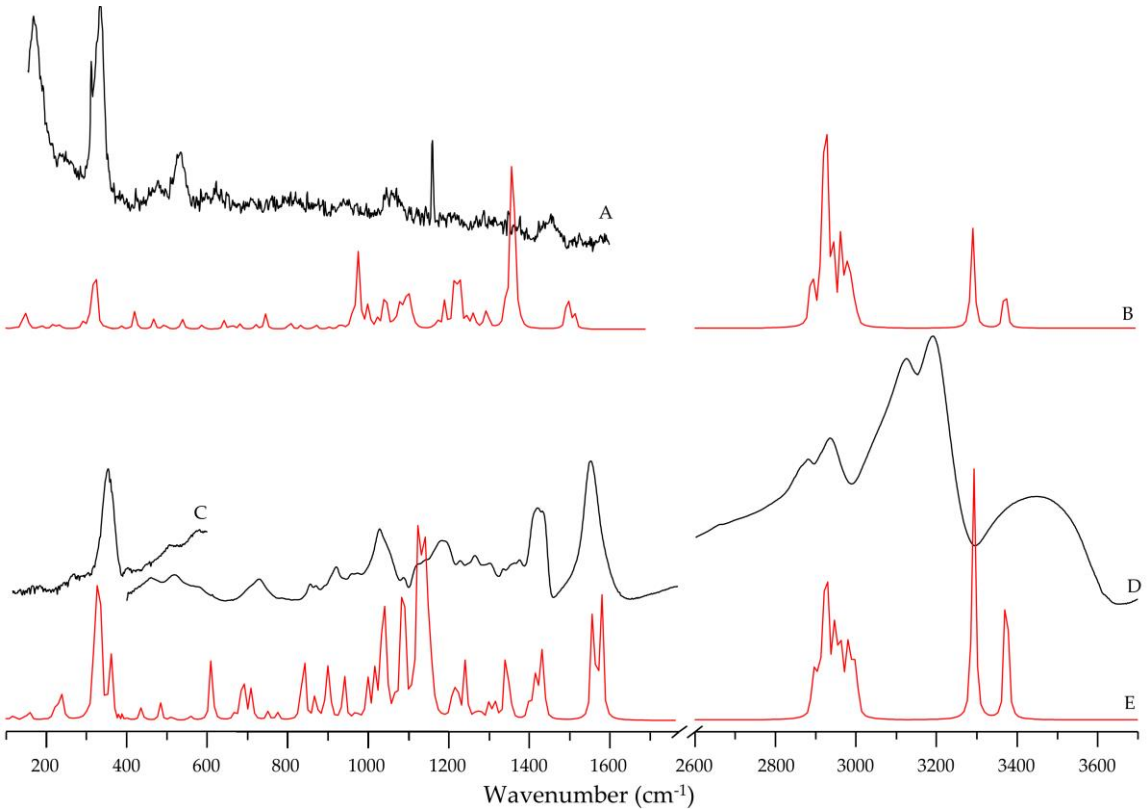

Figure 16: Vibrational spectra (100 – 1800 cm^{-1} and 2600 – 3700 cm^{-1}) for $Pt_3Spd_2Cl_6$: experimental (A) and calculated (B) Raman; experimental (C) FIR and (D) MIR and calculated (E), FTIR.

The bands indicating metal coordination resulting from the experimental results are: δN–Pt–Cl at 171 cm^{-1}, ν_{as}Cl–Pt–Cl at 326 cm^{-1}, ν_{s}Cl–Pd–Cl at 330 cm^{-1} and 331 cm^{-1}, νPt–$N_{(ring)}$ at 459 cm^{-1} and 475 cm^{-1}, νPt–Nat 528 cm^{-1}, 526 cm^{-1} and 475 cm^{-1}.

Table 4: Experimental and calculated vibrational wavenumbers (cm^{-1}) for $Pt_3Spd_2Cl_6$.

[b]Approximate description	Experimental		[a]Calculated	Sym. Species
	FTIR	Raman		
δN–Pt–Cl		171	156	B
δC–NH–C	312		302	B
ν_{as}Cl–Pt–Cl	326		324	B
ν_{s}Cl–Pt–Cl	330	331	334	A
δC–NH–C + δC–C–$C_{(ring)}$ + νPt–$N_{(ring)}$	459	475	464	A
νPt–N + δPt–N–C	526	528	516	A
ρ$NH_{2(central)}$	711		699	A
ρNH_2 + ρCH_2	735		720	A
ρCH_2 + τNH_2 + ν C–$C_{(ring)}$ + νC–N ring	866		853	B
ρ$CH_{2(rings)}$ + τ$CH_{2(chains)}$ + t$NH_{2(central)}$ + γNH	932	935	914	A
νC–C + νC–N + γNH	974	976	957	B
τCH_2 + τNH_2 + νC–N + νC–C	1040		1055	B
ωNH + νC–C + νC–$N_{(rings)}$		1055	1063	A
ωNH; ω$NH_{2(rings)}$; ω$NH_{2(chain)}$	1135		1108, 1150, 1167	B; A; B
τCH_2 + ωCH_2 + τ$NH_{2\ (central)}$	1249		1236	A
τ$CH_{2(rings)}$	1284		1268	A
ω$CH_{2(chain)}$	1320		1327	B
ω$CH_{2(rings)}$ + t$CH_{2(chain)}$ + τ$NH_{2(chain)}$	1356		1340	B
ωCH_2	1381		1371	B
ω$CH_{2(rings)}$	1398		1384	A
δNH + αCH_2	1440		1444	B
αCH_2		1445	1444	A
α$NH_{2(chain)}$; α$NH_{2(rings)}$	1577		1591; 1614	B
$\nu_{s}CH_2$	2881		2890; 2930	B
$\nu_{as}CH_2$	2935		2950; 2965	B
νNH; $\nu_{s}NH_2$	3192		3293; 3298	B
$\nu_{as}NH_2$	3449		3382	B
νCH	2881		2890	A
νCH + $\nu_{as}CH_2$	2935		2930	B
$\nu_{as}CH_2$	3126		3002	B
νNH	3192		3299	B
$\nu_{as}NH_2$	3449		3382	B

[a]At the wB97XD level. Scaled according to: 0.9475 for the bands in the 500 – 3700 cm^{-1} range; [b]Symbols for vibrational modes: ν stretching, α – scissoring, δ – in-plane deformation, τ – twisting, ρ – rocking, ω – wagging, γ – out-of-plane deformation, s, as, and a refer to symmetric, antisymmetric and asymmetric modes.

Exactly like the $Pd_3Spd_2Cl_6$ complex, $Pt_3Spd_2Cl_6$ presented a blue shift which was detected for the NH_2 asymmetric stretching and CH_2 asymmetric and symmetric stretching, occurring at 3449 cm^{-1}, 3126 cm^{-1} and 2881 – 2935 cm^{-1}, relative to the free spermidine ligand (Appendix B, Figure B1) at 3356 cm^{-1}, 2929 cm^{-1} and 2852 cm^{-1}, respectively. The bands corresponding to NH_2 symmetric stretching – 3192 cm^{-1}, NH_2 – 1577 cm^{-1} and CH_2 – 1440 – 1445 cm^{-1} scissoring modes, appeared shifted to lower frequencies comparing to the ligand spectra, 3274 cm^{-1}, 1600 cm^{-1}, 1470 cm^{-1}, respectively. These observed changes were due to the metal chelate effect, proving metal-ligand coordination.

3.1.3. $Pd_2Put_2Cl_4$

The conformation of the most stable geometry for the $Pd_2Put_2Cl_4$ chelate (Figure 17) (Appendix A, Figure A3, Tables A5 and A6) belongs to a C_i point group, displaying 120 vibrational modes, 60 with A_g symmetry Raman active and 60 with A_u symmetry infrared active.

The vibrational spectra obtained for $Pd_2Put_2Cl_4$ (FTIR and Raman) both experimental and theorical are comprised in Figure 18, allowing access to a more detailed assignment of the experimental vibrational profile, described in Table 5.

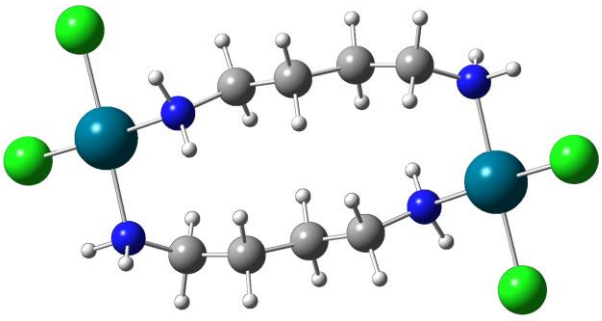

Figure 17: Structural representation of $Pd_2Put_2Cl_4$.

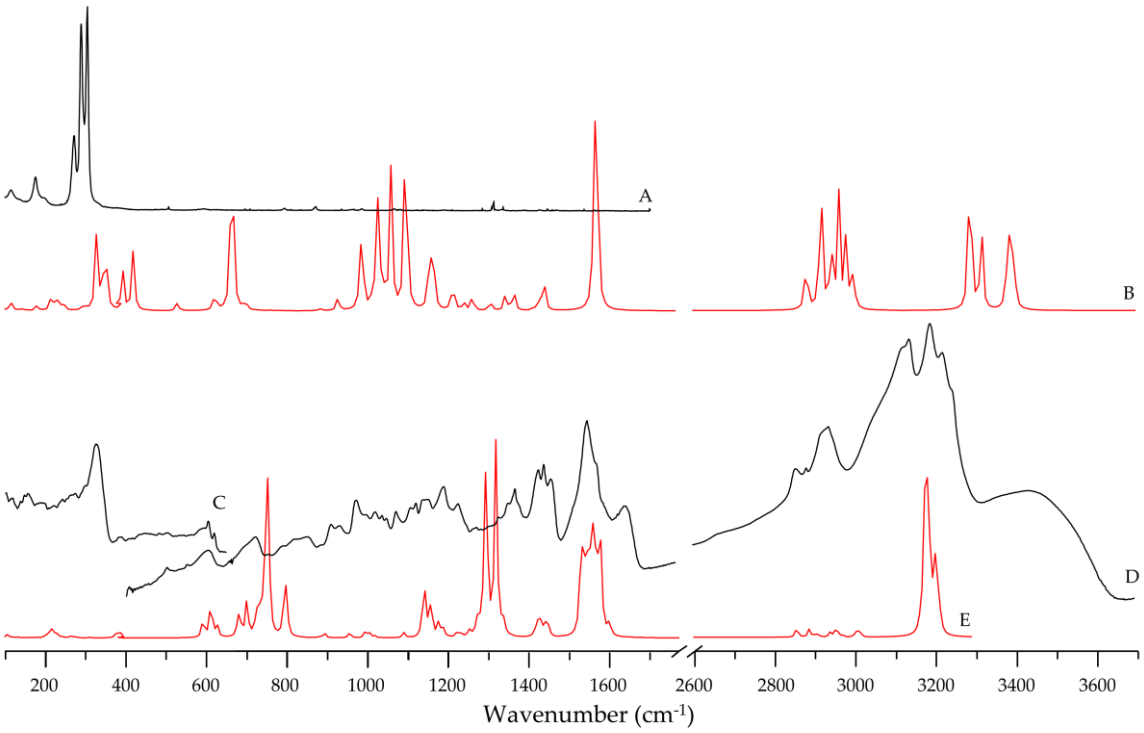

Figure 18: Vibrational spectra (100 – 1800 cm^{-1} and 2600 – 3700 cm^{-1}) for $Pd_2Put_2Cl_4$: experimental (A) and calculated (B) Raman; experimental (C) FIR and (D) MIR and calculated (E), FTIR.

The experimental results obtained: δN–Pd–N at 163 cm^{-1} and 195 cm^{-1}, ν_{as}Cl–Pd–Cl , at 302 cm^{-1} and 314 cm^{-1}, ν_{s}Cl–Pd–Cl at 332 cm^{-1}, and νPd–N at 427 cm^{-1}, indicate metal coordination.

Table 5: Experimental and calculated vibrational wavenumbers (cm^{-1}) for $Pd_2Put_2Cl_4$.

[b]Approximate description	Experimental		[a]Calculated	Sym. Species
	FTIR	Raman		
τN–C–C	112		113	A_u
τC–C–C + δN–Pd–N	163		177	A_u
τC–C–C + δN–Pd–N	195		215	A_u
ν_{as}Cl–Pd–Cl		302	332	A_g
ν_{as}Cl–Pd–Cl	314		329	A_u
ν_{s}Cl–Pd–Cl		332	353	A_g
νPd–N	427		416	A_u
δN–C–C		543	574	A_g
ρNH_2	609		630	A_u
ρNH_2	732		673	A_u
$\tau CH_2 + \rho CH_2 + \tau NH_2 + \omega NH_2$	923		897	A_u
ν_{s}N–C–C + $tNH_2 + \omega NH_2$	944		944	A_u
ν_{s}C–C–C + $tNH_2 + \omega NH_2$	987		1000	A_u
νC–C + νC–C	1012		1006	A_u

$\nu_{as}N{-}C{-}C$	1035		1045	A_u
$\tau CH_2 + \tau NH_2 + \omega NH_2$	1088		1078	A_u
$\rho CH_2 + \tau CH_2 + \tau NH_2 + \omega NH_2$	1169		1173	A_u
$\omega CH_2 + tNH_2 + \omega N^2H_2$	1210		1184	A_u
$\tau CH_2 + tNH_2 + \omega NH_2$	1245		1236	A_u
τCH_2	1291		1285	A_u
ωCH	1372		1370	A_u
ωCH_2	1390		1391	A_u
αCH_2	1448		1453	A_u
αCH_2	1464		1460	A_u
αCH_2	1484		1470	A_u
αNH_2	1576		1596; 1603	A_u
αNH_2		1660	1596; 1602	A_g
	1671			A_u
ν_sCH_2; $\nu_{as}CH_2$	2937		2919; 2963	A_u
ν_sNH_2	3138		3291	A_u
ν_sNH_2	3191		3319	A_u
$\nu_{as}NH_2$	3225		3386	A_u
OH	3435			

[a]At the wB97XD level. Scaled according to: 0.9475 for the bands in the 500 – 3700 cm^{-1} range; [b]Symbols for vibrational modes: ν stretching, α – scissoring, δ – in-plane deformation, τ – twisting, ρ – rocking, ω – wagging, γ – out-of-plane deformation, s, as, and a refer to symmetric, antisymmetric and asymmetric modes.

A shifted to lower frequencies was detected for the NH_2 symmetric stretching at 3191 – 3138 cm^{-1}, relative to the free putrescine hydrochloride ligand (Appendix B, Figure B2) at 3068 cm^{-1}. Other changes proving metal-ligand coordination are the CH_2 scissoring (1448 – 1484 cm^{-1}) and both stretching modes (2937 cm^{-1}) and the NH_2 asymmetric stretching (3225 cm^{-1}) and scissoring modes (1576 – 1671 cm^{-1}).

The OH band found in FTIR experimental results at 3435 cm^{-1} is means that the compound was not fully dry when the spectra was acquired.

3.1.4. $Pt_2Put_2(NH_3)_4^{4+}$

The conformation of the most stable geometry for the $Pt_2Put_2(NH_3)_4^{4+}$ chelate (Figure 19) (Appendix A, Figure A4, Tables A7 and A8) belongs to a C_i point group, displaying 156 vibrational modes, 78 with A_g symmetry Raman active and 78 with A_u symmetry infrared active.

In the calculation the chlorine anions were not considered, since their specific location was difficult to predict and, as reported in previous studies, the structure optimization was performed as if the molecule was inside the cells (physiologic pH = 7.4), with a charge of 4+ [74].

The vibrational spectra obtained for the $Pt_2Put_2(NH_3)_4^{4+}$ (FTIR and Raman) both experimental and theorical are comprised in Figure 20, leading to a more detailed assignment of the experimental vibrational profile, described in Table 6.

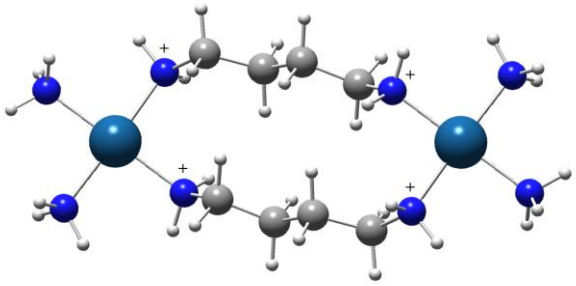

Figure 19: Structural representation of $Pt_2Put_2(NH_3)_4^{4+}$.

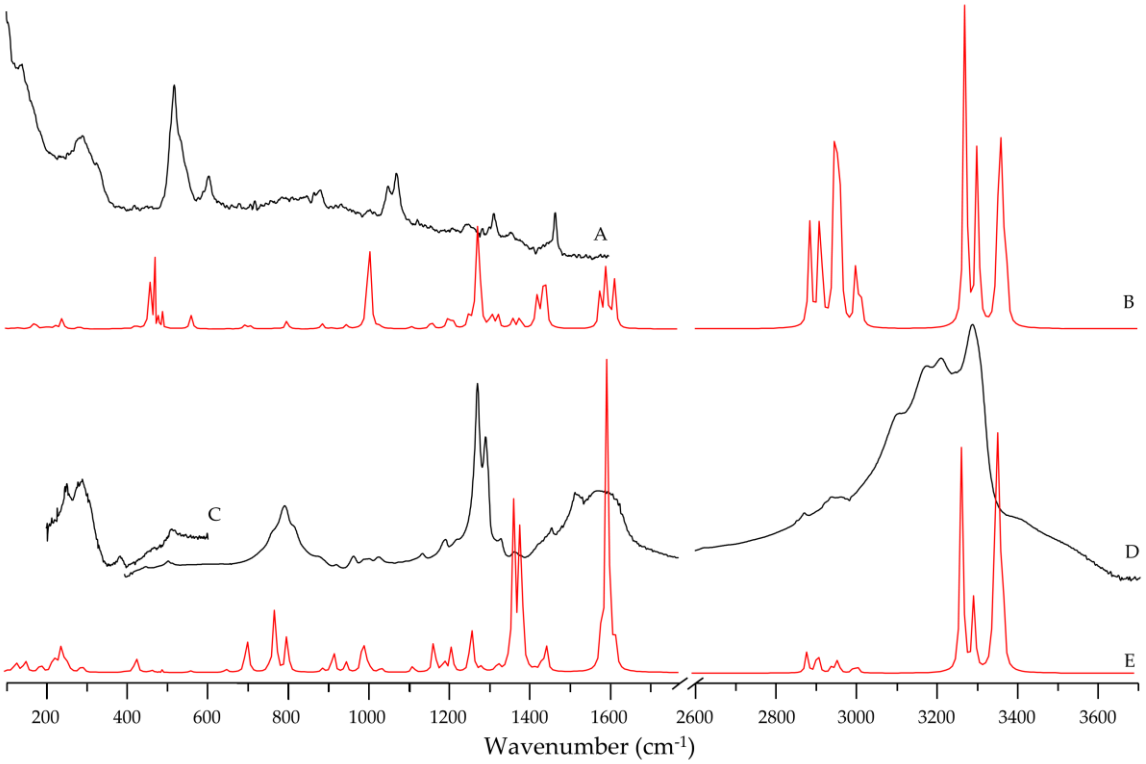

Figure 20: Vibrational spectra (100 – 1800 cm^{-1} and 2600 – 3700 cm^{-1}) for $Pt_2Put_2(NH_3)_4^{4+}$: experimental (A) and calculated (B) Raman; experimental (C) FIR and (D) MIR and calculated (E), FTIR.

The experimental results show a metal coordination through the Pt–N–C in plane deformation at 420 cm^{-1} and the H_2N–Pt–NH_3 symmetric stretching at 510 cm^{-1} and 523 cm^{-1}.

Table 6: Experimental and calculated vibrational wavenumbers (cm^{-1}) for $Pt_2Put_2(NH_3)_4^{4+}$.

[b]Approximate description	Experimental		[a]Calculated	Sym. Species
	FTIR	Raman		
τN–C–C		173	172	A_g
δC–C–C		381	403	A_g
	382		404	A_u
δPtNC		420	428	A_g
$\nu_s H_2N$–Pt–NH_3	510		496	A_u
$\nu_s H_2N$–Pt–NH_3		523	503	A_g
$\rho NH_3 + \rho NH_2$		647	664	A_g
$\rho NH_3 + \rho CH_2$		752	760	A_g
$\rho NH_3 + \rho CH_2$	804		783	A_u
$\rho CH_2 + tCH_2$	895		903	A_u
νC–NH_2	937		930	A_u
νC–NH_2 + ν_sCC–CC	979		962	A_u
ν_{as}N–C–C	1004		1005	A_u
ν_{as}CC–CC	1018		1020	A_u
$\tau CH_2 + \tau NH_2$	1043		1050	A_u
$\omega CH_2 + \tau NH_2 + \omega NH_2$	1151		1185	A_u
$\omega NH_2 + \tau CH_2$	1212		1210	A_u
$\omega NH_2 + \omega CH_2$	1291		1282	A_u
τCH_2	1312		1306	A_u
ωCH_2	1351		1346	A_u
ωCH_2	1387		1386	A_u
$\delta_s NH_3$	1404		1405	A_u
αCH_2	1456		1455	A_u
αCH_2	1464		1460	A_u
αCH_2	1480		1468	A_u
$\delta_{as} NH_3 + \alpha NH_2$	1538			
$\delta_{as} NH_3 + \alpha NH_2$	1556			
$\delta_{as} NH_3 + \alpha NH_2$	1597		1623	A_u
$\nu_s CH_2$	2872		2888	A_u
$\nu_s CH_2$	2936		2915	A_u
$\nu_{as} CH_2$	2959		2951 – 2966	A_u
$\nu_s NH_3$	3105			
$\nu_s NH_3$	3174			

$\nu_s NH_3$	3209		3274	A_u
$\nu_s NH_2$	3285		3306	A_u
$\nu_{as} NH_2 + \nu_{as} NH_3$	3396		3355 – 3378	A_u

[a]At the wB97XD level. Scaled according to: 0.9475 for the bands in the 500 – 3700 cm^{-1} range; [b]Symbols for vibrational modes: ν stretching, α – scissoring, δ – in-plane deformation, τ – twisting, ρ – rocking, ω – wagging, γ – out-of-plane deformation, s, as, and a refer to symmetric, antisymmetric and asymmetric modes

A blue shift was detected for the NH_2 asymmetric at 3396 cm^{-1} and symmetric stretching at 3285 cm^{-1}, and the CH_2 asymmetric and symmetric stretching at 2959 cm^{-1} and at 2872 – 2936 cm^{-1}, respectively, relative to the free putrescine hydrochloride ligand (Appendix B, Figure B3) at 3329 cm^{-1}, 3169 cm^{-1}, 2923 cm^{-1} and 2855 cm^{-1}. Other changes proving the metal-ligand coordination are the presence of the NH_2 scissoring mode at 1538 – 1597 cm^{-1} and the CH_2 scissoring mode at 1456 – 1495 cm^{-1} relative to the ligand at 1601 cm^{-1} for NH_2 scissoring mode and 1464 cm^{-1} for CH_2 scissoring mode.

The full conformational characterisation of this type of Pt(II)/Pd(II)-amine compounds, will be useful along this work, helping to clarify their mechanism of action within a cell and expose the molecular basis of their cytotoxicity. Another upside of this type of studies is their contribution to the rational design of new and more efficient cisplatin-like anticancer agents.

3.2. Cell Viability Evaluation

3.2.1. Single Drug

According to previous researches, $Pd_2Put_2Cl_4$, $Pt_2Put_2(NH_3)_4^{4+}$, $Pd_3Spd_2Cl_6$ and $Pt_3Spd_2Cl_6$ have reported results against cell lines such as HSC-3 (IC_{50} = 32 μM of $Pd_3Spd_2Cl_6$ at 48 h) oral squamous carcinoma cells [35], MDA-MB-468 (IC_{50} = 0.70 μM of $Pd_2Put_2Cl_4$ at 72 h; IC_{50} = 0.90 μM of $Pd_3Spd_2Cl_6$ at 72 h) and MDA-MB-231 (drug sensitive and drug-resistant, IC_{50} = 8.44 μM and 10.63 μM of $Pd_3Spd_2Cl_6$, respectively, and for both the IC_{50} for $Pt_3Spd_2Cl_6$ is higher than 100 μM for 24, 48 and 72 h) breast cancer cell lines [75, 76], HL-60 (IC_{50} = 0.53 μM of $Pd_2Put_2Cl_4$ at 24 h)[67] leukaemia cells and A549 (IC_{50} = 1.8 μM of $Pt_2Put_2(NH_3)_4^{4+}$ at 72 h) lung cancer [40]. Cisplatin, Pd_2SpmCl_4, and Pt_2SpmCl_4 were assessed in previous studies against the MG-63 cell line (IC_{50} = 12.0 μM, 14.9 μM, 240.2 μM at 48 h, respectively) [2].

Figure 21 comprises the MTT results for $Pd_3Spd_2Cl_6$ (A), $Pt_3Spd_2Cl_6$ (B), $Pd_2Put_2Cl_4$ (C), and $Pt_2Put_2(NH_3)_4^{4+}$(D) for MG-63 cell line, which showed to be sensitive in the presence of all the tested drugs.

For $Pd_3Spd_2Cl_6$ (A), a range of concentrations from 5.31 to 170 μM was tested in order to evaluate the cytotoxic effect. The MTT results present a continuous decrease in cell viability with increasing drug concentration, for each exposure time. The lowest IC_{50} found, which indicated the higher drug effect was 10.9 μM at 24 and 72 h (Table 8).

A range of concentrations from 18.3 to 300 μM was tested, for $Pt_3Spd_2Cl_6$ (B). The MTT results present a continuous decrease in cell viability with increasing drug concentration for each time point. The lowest IC_{50}, was 48.2 μM at 72 h, a lower value than what was obtained for MDA-MB-231 (IC_{50} > 100 μM) [75].

The analogue complexes, $Pd_3Spd_2Cl_6$ and $Pt_3Spd_2Cl_6$, present distinct IC_{50} values, Pd greatly surpasses the activity displayed by Pt. Comparing to other analogue complexes such as Pd_2SpmCl_4 and Pt_2SpmCl_4 the same is observed, in osteosarcoma [2], triple-negative breast cancer [77], and ovarian cancer [78].

The same range of concentrations of $Pt_3Spd_2Cl_6$ was used for $Pd_2Put_2Cl_4$. At 72 h of exposure the two lower concentrations presented an increase of cells viability than the

control. The lowest IC_{50}, was 91.9 μM at 48 h, which is very high and not suitable concentration to use in cancer treatment.

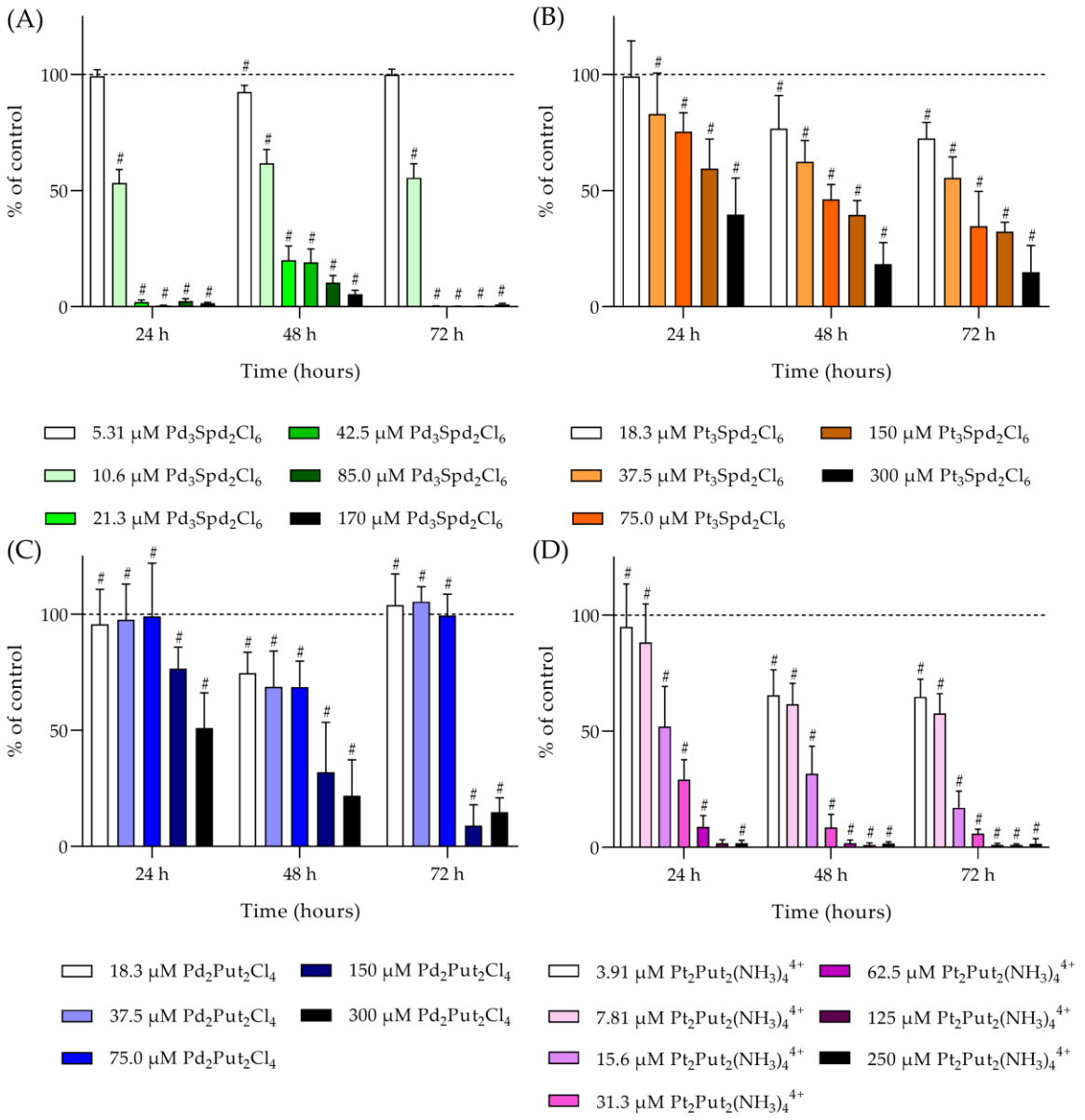

Figure 21: Effect on cell viability measured by the MTT assay of (A) $Pd_3Spd_2Cl_6$, (B) $Pt_3Spd_2Cl_6$, (C) $Pd_2Put_2Cl_4$ and (D) $Pt_2Put_2(NH_3)_4^{4+}$, against MG-63 cell line, after 24, 48 and 72 h of drug exposure, at concentrations ranging from 5.31 to 170 μM for $Pd_3Spd_2Cl_6$, 3.91 to 250 μM for $Pt_2Put_2(NH_3)_4^{4+}$, 18.3 to 300 μM for $Pt_3Spd_2Cl_6$ and $Pd_2Put_2Cl_4$. The results are expressed in % of control ± SD, obtained from four independent experiments, each with eight replicates. The one-way ANOVA statistical analysis was carried out to verify the significance of the obtained results (#p<0.0001) *vs*. the control for the same time-points followed by Dunnett's multiple comparison test.

Finally, $Pt_2Put_2(NH_3)_4^{4+}$ was tested with a concentration range of 3.91 to 250 μM The MTT results present a continuous decrease in cell viability at each time point with increasing drug concentration. The lowest IC_{50}, was 11.4 μM at 48 h, demonstrating

promising results, and enhance to be analyse in the future not only the evaluation of cells' viability in combination with doxorubicin and methotrexate, but also the metabolic impact caused in MG-63 and HOb cell lines. However, it was not chosen because, since it had almost identical results to the $Pd_3Spd_2Cl_6$ compound, and it was intended to compare with Pd_2SpmCl_4 and cisplatin it was opted for the more similar compound (overall structure and type of interactions with DNA).

The IC_{50} values summary for $Pd_3Spd_2Cl_6$, $Pt_3Spd_2Cl_6$, $Pd_2Put_2Cl_4$ and $Pt_2Put_2(NH_3)_4^{4+}$ against the MG-63 cell line for the three time points study are comprised in the Table 7.

Table 7: Half maximal inhibitory concentration (IC_{50}, μM) of $Pd_3Spd_2Cl_6$, $Pt_3Spd_2Cl_6$, $Pd_2Put_2Cl_4$ and $Pt_2Put_2(NH_3)_4^{4+}$ against osteosarcoma (MG-63) cell line, at 24, 48, and 72 h incubation times.

Drug	24 h	48 h	72 h
$Pd_3Spd_2Cl_6$	10.9 ± 2.1	13.5 ± 1.3	10.9 ± 1.1
$Pt_3Spd_2Cl_6$	207± 1	69.8 ± 1.4	48.2 ± 1.4
$Pd_2Put_2Cl_4$	301 ± 2	91.9 ± 1.1	121 ± 1
$Pt_2Put_2(NH_3)_4^{4+}$	19.6 ± 1.6	11.4 ± 1.5	11.8 ± 1.8

The HOb cells were administrated with the IC_{50} previously determined for the MG-63 cells at 48 h incubation time, for cisplatin, Pd_2SpmCl_4 and the drug that have exhibited promising results and have a similar mechanism of action, in this case, $Pd_3Spd_2Cl_6$. The results for the HOb cell line when incubated with the chosen complexes are depicted in Figure 22.

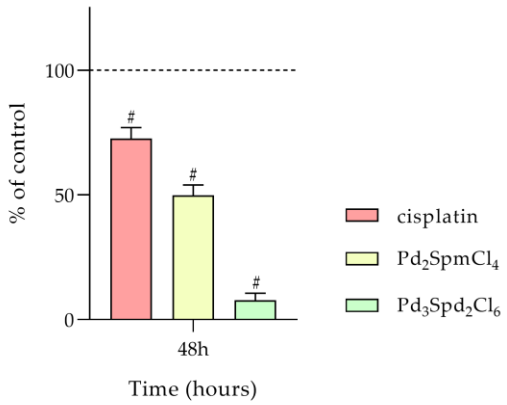

Figure 22: Effect on cell viability measured by the MTT assay of cisplatin (12 μM), Pd_2SpmCl_4 (14 μM) and $Pd_3Spd_2Cl_6$ (12 μM) in HOb cell line, after 48 h of exposure. The results are expressed in % of control ± SD, obtained from four independent experiments, each with eight replicates. The one-way ANOVA statistical analysis was carried out to verify the significance of the obtained results (#$p<0.0001$) *vs* the control for the same time-points followed by Dunnett's multiple comparison test.

Since in healthy cells the aim is having the higher percentage of control, the target is compound selectivity, maintaining the maximum integrity of the healthy cells, but simultaneously induce irreversible damages to cancer cells. In this case the concentration needed to produce half of the effect (IC_{50}) on MG-63 population was used. Comparing the results cisplatin have shown the best data in single drug administration with an IC_{50} of 12.0 μM at 48h.

3.2.2. Drug Combination

According to the EURAMOS-1 protocol, the combination of cisplatin with DOX and MTX has stunning results when compared to single drug administration. The same protocol was applied to the complexes under study, so they could be compared to cisplatin meaning that cells were allowed to incubate with the Pt/Pd drug in combination with DOX for 72 h prior to MTX administration and incubation for an additional 24 h period.

The evaluation of the effect of these drugs cocktails against MG-63 and HOb cell lines was caried out through the MTT assay (Figure 23). For the MG-63 cell line $Pd_3Spd_2Cl_6$, $Pt_3Spd_2Cl_6$, $Pd_2Put_2Cl_4$ or $Pt_2Put_2(NH_3)_4^{4+}$, in combination with DOX was added and cell viability evaluated at 24, 48, 72 and 96 h time points, in order to understand the combination of the Pt/Pd drug with DOX effect along all the exposure times and to compare with the 96 h time point also treated with MTX at 72 h after initial drug exposure. In HOb the combinations with cisplatin, Pd_2SpmCl_4 or $Pd_3Spd_2Cl_6$ was administrated and the 96 h time point from initial drug exposure (with and without MTX) was evaluated.

All the combinations used against MG-63 cells have exhibited promising results, and when compared to single drug, the outcome agrees to what is described in EURAMOS-1 protocol, other articles have presented increase the success rate when using more than one drug in the treatment [79-81]. The importance of performing single drug assays was allowing to prove the combination synergetic effects. The regimen needed to be investigated also against HOb cells, in order to understand if the combination have some type of selectivity, as a way to design more effective anti-cancer drugs with minimal toxic side effects.

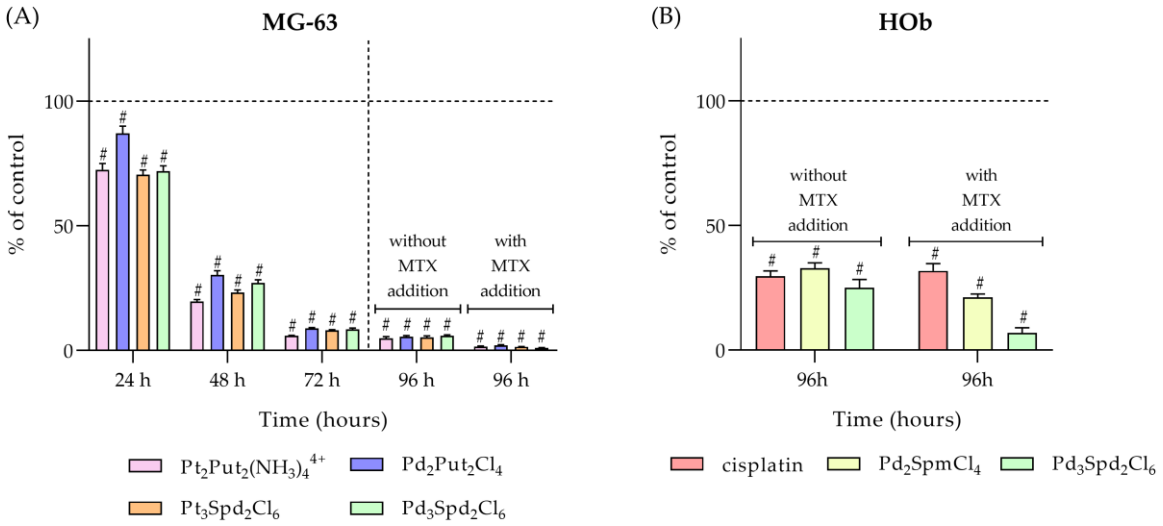

Figure 23: Effect on cell viability measured by the MTT assay of: (A) $Pd_2Put_2Cl_4$, $Pt_2Put_2(NH_3)_4^{4+}$, $Pd_3Spd_2Cl_6$ or $Pt_3Spd_2Cl_6$ in combination with DOX against MG-63 cell line after 24, 48 and 72 h of exposure, and with or without MTX after 96 h of exposure; (B) cisplatin, Pd_2SpmCl_4 or $Pd_3Spd_2Cl_6$ in combination with DOX and with or without MTX against HOb cell line after 96 h of exposure (B). The results are expressed in % of control ± SD, obtained from four independent experiments, each with eight replicates. The one-way ANOVA statistical analysis was carried out to verify the significance of the obtained results (#$p<0.0001$) *vs* the control for the same time-points followed by Dunnett's multiple comparison test.

3.3. Metabolic Impact

According to the results obtained in previous and already published studies regarding the evaluation of the antitumor effect of Pd_2SpmCl_4 and cisplatin against MG-63 cells carried out at QFM-UC, at different time-points and dosages, for a single drug administration a 48 h exposure period with the IC_{50} concentrations at this time (14 μM and 12 μM, respectively) was chosen. Since $Pd_3Spd_2Cl_6$, with a IC_{50} concentration of 12 μM at 48 h of drug exposure, has shown promising results, it was chosen to be compared to the drugs from previous studies [2, 39, 40, 75]. The drug exposure methodology was performed the same way for both MG-63 and HOb cell lines.

MG-63 and HOb cells were fixed according to a biocompatible preservation method, using formalin, a solution of formaldehyde in water, as a fixing agent. This is considered the best method of cell fixation, as a way to avoid contamination in the fixation and keeping the sample in a condition similar to the physiological state. Formalin allows the formation of methylene bridges between its aldehyde groups and the primary and secondary amine groups of the cell's proteins, which allows keeping the cell's constituents similar to those in *in vivo* cells. Due to the presence of this fixing agent, the intensity of the signal obtained by infrared is expected to be slightly lower, due to the conformational change of proteins and lipids breakdown.

For each experimental condition, an average spectrum (Figure 24) was obtained containing information from cells present in either MgF_2 and CaF_2 disks that describes the biochemical characteristics of the cells and type of single drug/combination. It is important to bear in mind that the result of these spectra will vary from cell to cell, so a high spectral heterogeneity is needed. That is, the cells will be in various stages of the cell cycle, opposing to single cell spectral acquisition, minimising the effect of the cell cycle profile, which in normal conditions is predominantly G_1.

The representation of the average spectrum obtained for both cell lines with the respective allocation of the most important bands from 1050 – 1800 cm^{-1} for FTIR and 600 – 1800 cm^{-1} for Raman (Figure 24).

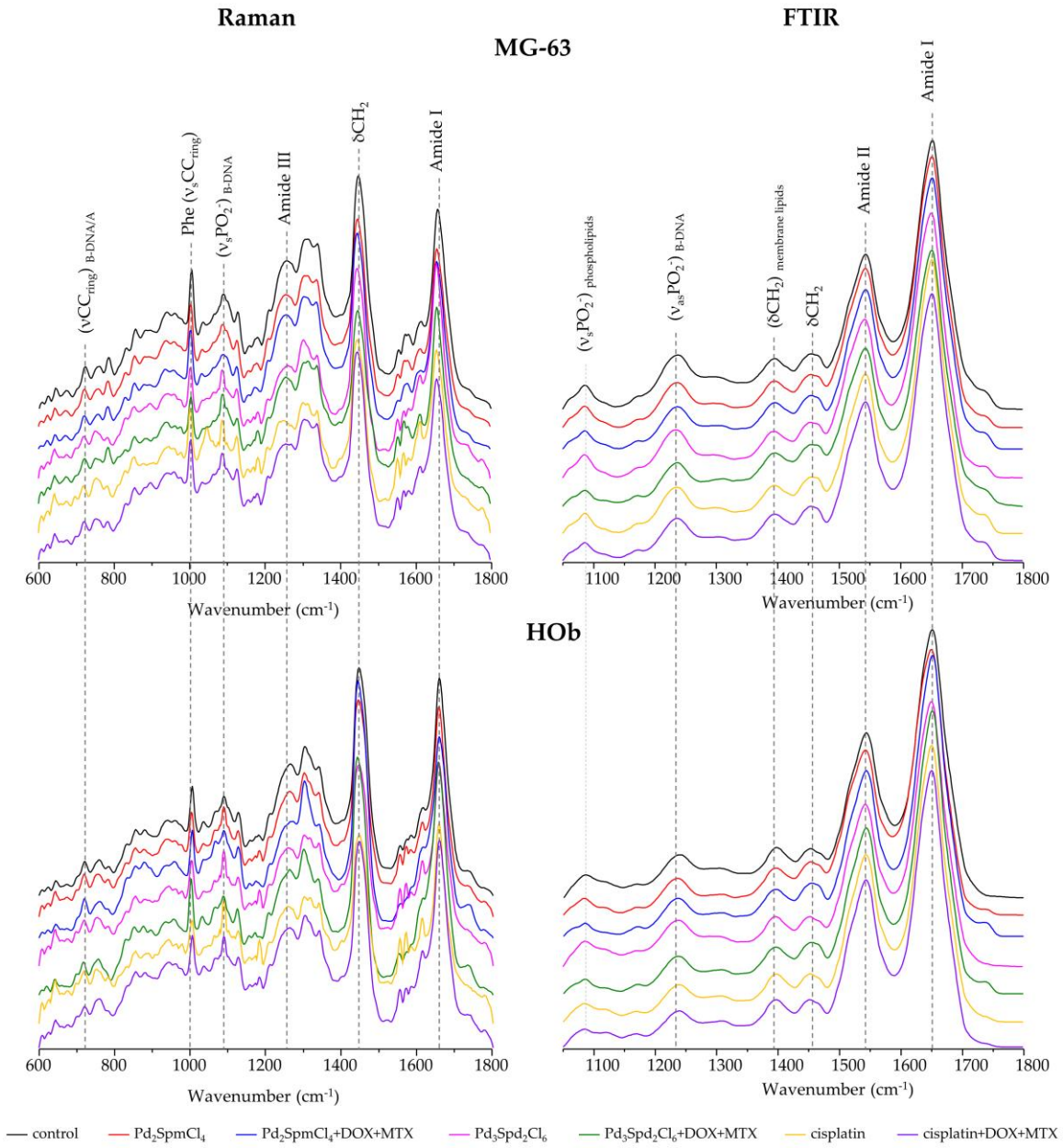

Figure 24: Mean Raman (600 – 1800 cm^{-1}) and FTIR (1050 – 1800 cm^{-1}) spectra of MG-63 and HOb cell lines for untreated/control (black line), Pd_2SpmCl_4-treated (red line), Combination of Pd_2SpmCl_4-treated (blue line), $Pd_3Spd_2Cl_6$-treated (pink line), Combination of $Pd_3Spd_2Cl_6$-treated (green line), cisplatin-treated (yellow line), and Combination of cisplatin-treated (purple line) cells.

Table 8 identifies the assignments for all bands present in the infrared and Raman spectrum of both cell lines, separated by nucleic acids, proteins, lipids, and carbohydrates, relied on reported studies on several cell lines and biomolecules [36, 38, 39, 82, 83].

Table 8: Raman and infrared bands for human healthy bone cells and osteosarcoma cells (HOb and MG-63). Features from specific drug-prompted DNA and protein conformational rearrangements are presented in red. The signals exclusively detected by infrared are shaded in grey.

Bands (cm^{-1})	[a]Assignment			
	Nucleic acids	**Proteins**	**Lipids**	**Carbohydrates**
1738			phospholipids ($\nu C{=}O_{ester}$)	
1714 – 1712	A-DNA ($\nu C{=}O$)			
1709	B-DNA ($\nu C{=}O$)			
1697		$\nu C{=}O_{amino\ acid\ side\ chain}$		
1692 – 1676		amide I/β-sheet, antiparallel		
1663 – 1648		amide I/random coil		
1660 – 1650	DNA (δNH)	amide I ($\nu C{=}O$)/α-helix	$\nu C{=}C$	
1668 – 1559	A,G (νCC_{ring})			
1633 – 1615		amide I/β-sheet, parallel		
1616 – 1615	A (νCC_{ring}), C (δNH_2)	Phe, Tyr, Trp ($\nu C{=}C$), δNH_2		
1585 – 1582		$\nu C{=}C$, $\nu C{=}N$	$\nu C{=}C$, $\nu C{=}N$	
1574 – 1573	A,G (νCC_{ring})			
1556	G (νCC_{ring})	Trp (νCC_{ring}), $\nu C{=}C_{porphyrin}$		
1543 – 1542		amide II (δCN-H/νCN)		
1523 – 1517		$\nu C{=}C_{porphyrin}$		
1509		Tyr (νCC_{ring})		
1483		δNH_3		
1467 – 1464		δCH_2, δCH_3	δCH_2, δCH_3, aromatic lipids	δCH_2
1454 – 1445			δCH_2	
1430 – 1427	Z-DNA (δCH_2)			
1420 – 1413	A-DNA (δCH_2)			
1410		δNH_3		
1403 – 1402		δNH_2		
1397 – 1395		δCH_2, ρCH_2	membrane lipids (δCH_2)	δCH_2, ρCH_2
1375	A,G,T (νCC_{ring})	glycoproteins (δCH_3)	lipids/acyl chains (δCH_3)	saccharides (δCH_2)
1344 – 1339	G (νCC_{ring})			
1316	G (νCC_{ring})	δCH_2	δCH_2	δCH_2
1307 – 1303	RNA/A,C (νCC_{ring})			
1293 – 1290		Amide III/α-helix	δCH_2, ωCH_2, τCH_2	δCH_2, ωCH_2, τCH_2
1265	A,T (νCC_{ring})	δCH_2, $\delta C{=}C{-}H$	δCH_2, $\delta C{=}C{-}H_{phospholipids}$	δCH_2, ωCH_2, τCH_2
1259	RNA/dT (νCC_{ring})			
1250 – 1240		amide III/random coil		
1239 – 1236	B-DNA ($\nu_{as}PO_2^-$)			
1235 – 1228		amide III/β-sheet		
1212 – 1211		Hyp, Phe, Tyr (νCC)		
1182 – 1168	C,G,T (νCC_{ring})	Tyr, Phe (δCH)		
1160 – 1157		νCC, νCN, δCH_2	δCH_2, $\nu{=}C{-}C{=}_{conjugated}$	δCH_2
1128 – 1120	RNA/ribose (νCO)	νCN	νCC_{acyl} (*trans* conformation)	νCO, νCC
1102			νCC, νCN	νCC, νCO
1099 – 1098	A-DNA ($\nu_sPO_2^-$)			
1096 – 1095	Z-DNA ($\nu_sPO_2^-$)			
1090 – 1089	B-DNA ($\nu_sPO_2^-$)			
1086 – 1085		νCC, νCN	phospholipids ($\nu_sPO_2^-$)	glycogen (νCC, νCO)
1070 – 1065	B-DNA/deoxyribose (νCO)	νCC, νCN	νCC, νCO	νCC, νCO, δOCH
1037 – 1035		Phe (δCH), $\nu O{-}CH_3$	νCC, phospholipids (δCH)	νCC, νCO, $\nu C{-}OH$
1006		Phe (ν_sCC_{ring})		
979 – 973	RNA (ribose, νCC_{ring})			
960	DNA ($\nu(CC)$/$\nu CO_{backbone}$)			polysaccharides ($\delta C{=}O$)
940	RNA/ribose (νCC_{ring})			polysaccharides (skeletal modes)
935 – 927	Z-DNA ($\nu OPO_{backbone}$)			
897	deoxyribose (νCC_{ring})	νCC	fatty acids (νCC, νCO)	νCOC
883-880		ρCH_2		
874 – 872	Z-DNA ($\nu OPO_{backbone}$)			
856		Pro, Tyr, Val (νCC, δCCH)		polysaccharides (γCOC)
848 – 839	Z-DNA ($\nu OPO_{backbone}$)			
833	B-DNA ($\nu OPO_{backbone}$)	Pro, Tyr (νCC)		
819 – 815	RNA ($\nu OPO_{backbone}$)	Pro, Tyr (νCC)		
785	B-DNA ($\nu OPO_{backbone}$)			
760 – 759	B-DNA/dT (νCC_{ring})	Trp (ν_sCC_{ring})		
748	Z-DNA ($\nu OPO_{backbone}$)			
723 – 721	B-DNA/A (νCC_{ring})	Trp (ν_sCC_{ring})		

703	B-DNA/dG (νCC_{ring})	Met (νCS)		
674	B-DNA/G,T (νCC_{ring})			
667	A-DNA/dG (νCC_{ring})			
646		νCS, Tyr (τCC)		
625		Phe (τCC)		
620	Z-DNA/dG (νCC_{ring})			

[a]A – adenine; C – cytosine; dG – deoxyguanine; dT – deoxythymine; G – guanine; Glu – glucose; Hyp – hydroxyproline; Met – methionine; Phe – phenylalanine; Pro – proline; T – thymine; Trp – tryptophan; Tyr – tyrosine; U – uracil; Val – valine. δ – in-plane deformation; γ – out-of-plane deformation; ν – stretching; ρ – rocking; τ – twisting; ω – wagging. s – symmetric; as – anti-symmetric.

Not only MG-63 cells, but also HOb cells were sensitive in the presence of single drug administration and combination, observed by each condition average spectra (Figure 24) and in more detailed by principal components analysis (PCA) (Figure 25, Figure 26 and Figure 27), of the FTIR and Raman spectroscopic results was performed in order to unveil the chemical differences between control and drug treated cells for each cell line under study (Figure 6). Overall, a good discrimination was attained for both spectroscopies between controls, single drug, and combination treated cells for each cell line. In order to help with the discrimination for the single drug *vs* combination, related figures are appended to Appendix C (Figures C1 to C12). A slight overlap between the scores of the control and drug treated classes was expected, evidencing that the drugs did not affect the cells substantially towards complete destruction, already proved in the literature [38, 39, 57].

Due to optical problems (FTIR) and fluorescence (Raman), the high wavenumber spectral region cannot be analysed.

In the same way as reported in other studies [38, 84, 85], the spectral results are different for each cell line, so a PCA was obtained for both untreated cells (Figure 25) to understand the specific biomarkers that differentiate them through both microspectroscopies, FTIR and Raman.

The main discrimination observed in the FTIR spectra was along principal component 2 (PC2) (explaining 12.7% of total variance) and in Raman spectra by principal component 1 (PC1) (explaining 38.5% of total variance). From these scores and loadings, it is possible to observe a clear discrimination between control MG-63 *vs* control HOb.

MG-63 have a higher contribution from DNA bands (νCC_{ring} – adenine, guanine and thymine bases) at 1375 cm^{-1}, (δNH) at 1651 cm^{-1} (IR) and ($\nu CC/\nu CO_{backbone}$) at 964 cm^{-1}, in deoxyribose (νCC_{ring}) at 898 cm^{-1} (Raman) and in the conformation B-DNA ($\nu C{=}O$) at 1712 cm^{-1}, ($\nu OPO_{backbone}$) at 833 cm^{-1} and 785 cm^{-1}, dG (νCC_{ring}) at 699 cm^{-1} (Raman), ($\nu_{as}PO_2^-$) at 1234 cm^{-1} (IR) and at 1239 cm^{-1} (Raman). In proteins, the α-helix of amide I at

1651 cm^{-1} and amide III at 1296 cm^{-1}, δNH_3 at 1416 cm^{-1} (IR), $\nu_s CC_{ring}$ of phenylalanine at 1006 cm^{-1}, in proline, tyrosine and valine (νCC and δCCH) at 857 cm^{-1} (Raman). In lipids phospholipids $\nu C{=}O_{ester}$ at 1734 cm^{-1} (IR) and $\nu_s PO_2^-$ at 1081 cm^{-1} (Raman), δCH_2 and δCH_3 from aromatic lipids, 1464 cm^{-1}, δCH_3 in acyl chains at 1375 cm^{-1}, fatty acids (νCC, νCO) at 1073 cm^{-1} (IR) and 898 cm^{-1}, νCC and νCN at 1101 cm^{-1} (Raman).

On contrary, HOb have a higher contribution in G (νCC_{ring}) of nucleic acids at 1553 cm^{-1} and 1334 cm^{-1} (Raman), in νCO of the ribose in RNA, 1128 cm^{-1}, and the deoxyribose of B-DNA, 1073 cm^{-1} (IR). The νCC_{ring} of tyrosine and the νC=C of porphyrins at 1553 cm^{-1} (Raman), in proteins. For lipids, in δCH_2 1438 cm^{-1} (Raman), and νCC_{acyl} from the trans conformation at 1128 cm^{-1} (IR).

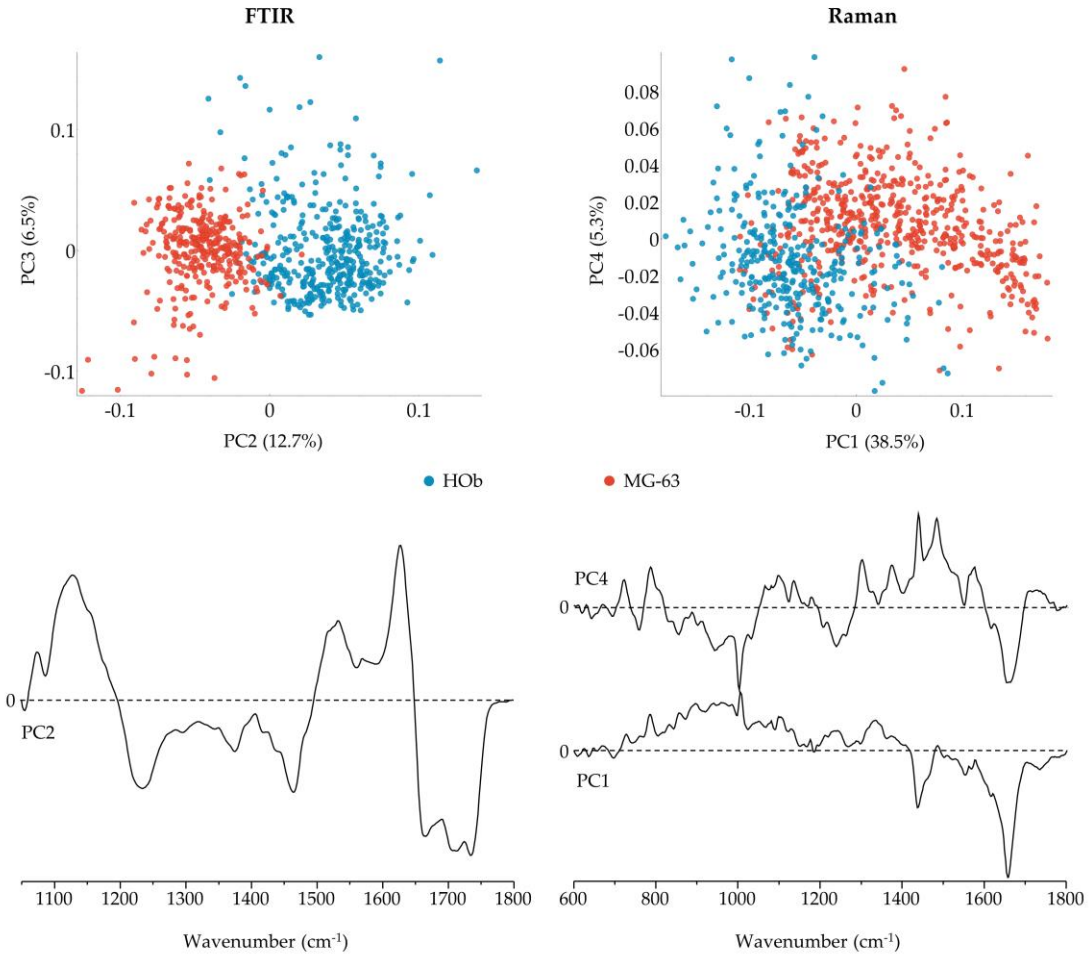

Figure 25: PCA scores and loading plots of FTIR (1050 – 1800 cm^{-1}) and Raman (600 – 1800 cm^{-1}) data for HOb *vs* MG-63 cell lines. (For clarity the loadings are offset, the dashed horizontal lines indicating zero loading).

By this clear discrimination between these two cell lines a direct comparison by PCA of the same drug condition in both cell lines cannot be performed, because the results will

not only be showing the effect cause by the drug exposure in different cell lines, but also the cell lines effect it selves.

3.3.1. MG-63 Cell Line

For cisplatin, the main discrimination observed in the FTIR spectra (Figure 26(A)) was along PC5 where there is a separation of cisplatin (with a slit overlap of the control) from the combination, which demonstrates the different mechanisms of action for each condition, and PC6 that separates treated from non-treated (explaining 1.6% and 1.0% of total variance, respectively).

In Raman (Figure 26(D)) spectra, the separation was obtained along PC3 and PC4 (explaining 14.1% and 4.5% of total variance, respectively). Due to fluorescence induced by the presence of MTX in the Raman spectra [86-88], a large amount of data was discarded in the pre-processing phase. Since the drug combination with cisplatin was greatly affected (Figure 26(D)), with only a few points left to analyse, it could not be considered for analysis.

Regarding the cisplatin combination *vs* cisplatin *vs* control discrimination, the combination presents a higher contribution from DNA bands (νCC_{ring} – adenine, guanine, and thymine bases) at 1341 cm^{-1}, 1314 cm^{-1}, 1268 cm^{-1} and from νCO of the ribose present in the RNA at 1128 cm^{-1}. It is expected that the combination has a higher impact on DNA bands, since DOX inhibits topoisomerase II, an enzyme essential for cutting both strands of the DNA, managing the entanglement and knots of the DNA helix, allowing its replication. At the proteins level, the β-sheets exhibited changes on the amide I (antiparallel) at 1678 cm^{-1} and (parallel) at 1623 cm^{-1}, the amide II (δCN–H/νCN) at 1560 cm^{-1}, δCH_2 at 1341 cm^{-1}, 1314 cm^{-1} and 1268 cm^{-1}, and the νCC_{ring} of tryptophan at 1341 cm^{-1}. The drug cocktail demonstrated higher contribution from δCH_2 of lipids at 1398 cm^{-1} (membrane lipids), 1314 cm^{-1}, 1268 cm^{-1} and 1151 cm^{-1}, and from νCC_{acyl} from the *trans* conformation at 1125 cm^{-1}. All the lipids' biomarkers show a higher impact in the presence of the combination.

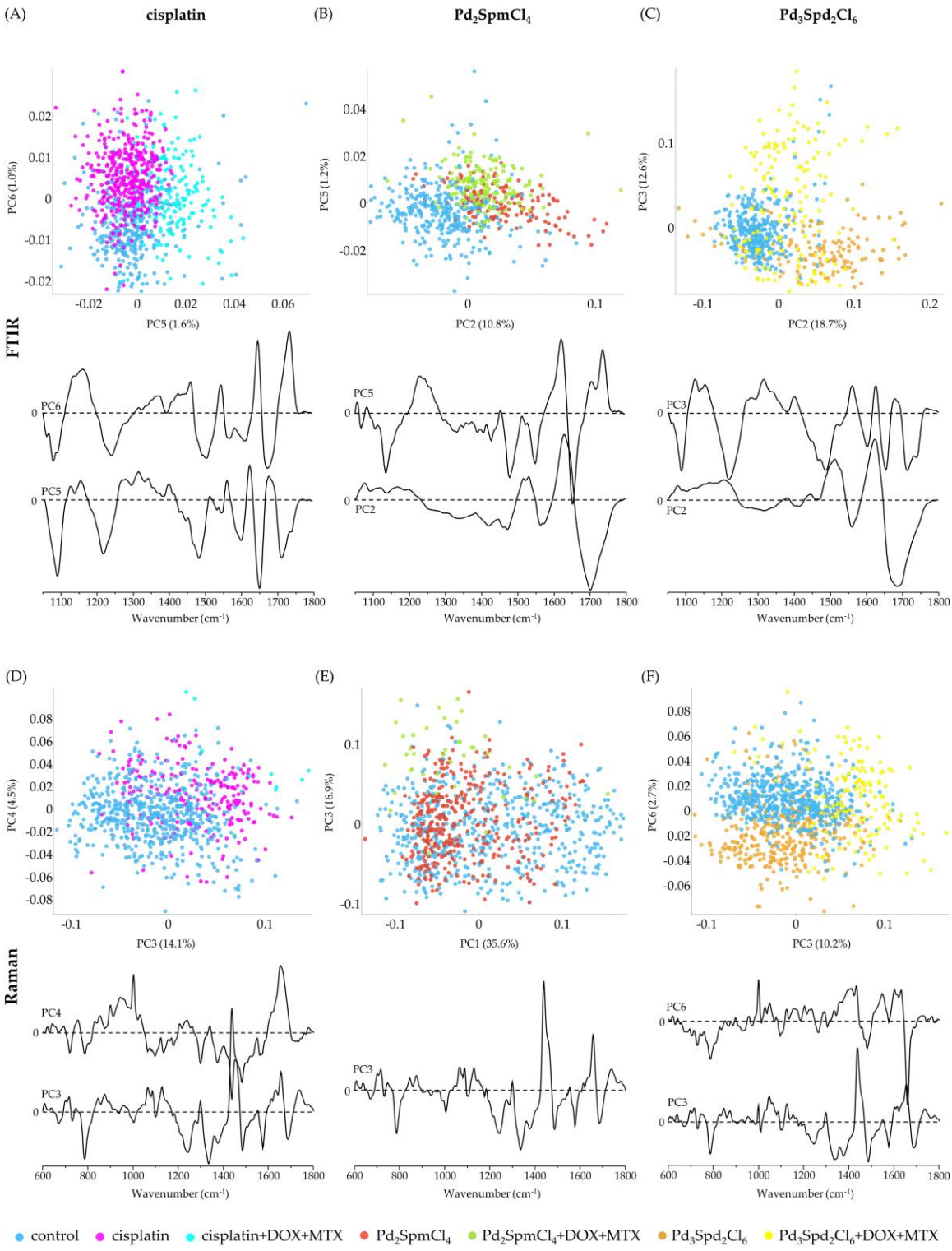

Figure 26: PCA scores and loading plots of FTIR (A,B,C; 1050 – 1800 cm^{-1}) and Raman (D,E,F; 600 – 1800 cm^{-1}) data for MG-63 cell line, cisplatin (A, D), Pd_2SpmCl_4 (B,E), and $Pd_3Spd_2Cl_6$-treated *vs.* their respective combination *vs* control. (For clarity the loadings are offset, the dashed horizontal lines indicating zero loading).

Single-drug administration contrary to drug combination presented changes in DNA native conformation from a B- to an A- at 1714 cm^{-1} and a Z- at 1428 cm^{-1}

conformations. On proteins changes were mainly found on amide I at the random coil level at 1652 cm^{-1} and in the δNH_3 at 1482 cm^{-1}. Concerning the lipids, the δCH_2 at 1446 cm^{-1}, the phospholipids $\nu C{=}O_{ester}$ at 1740 cm^{-1} and $\nu_s PO_2^-$ at 1088 cm^{-1}, may be indicative of a drug interaction with the cellular membrane (phospholipid moieties). Comparing cisplatin and drugs combination, the single drug administration demonstrates a higher damage to DNA while the combined administration showed a higher impact on proteins, both present severe alterations to lipids mainly regarding the membranes' integrity.

Pd_2SpmCl_4 single drug, drugs combination and control present some overlapping, observed in PC2 and PC5 (explaining 10.8% and 1.2% of total variance, respectively) in FTIR (Figure 26(B)) and PC3 (explaining 16.9% of total variance) in Raman (Figure 26(E)). The drug combination presented a higher contribution from B-DNA bands ($\nu C{=}O$) (IR) at 1706 cm^{-1}, ($\nu_s PO_2^-$) 1089 cm^{-1}, (deoxyribose νCO) 1066 cm^{-1}, and (adenine νCC_{ring}) (Raman) 717 cm^{-1}. Moreover, changes in the DNA native conformation were obtained due to the presence of A-DNA (δCH_2) at 1420 cm^{-1} (IR) and $\nu OPO_{backbone}$ of the Z-DNA at 874 cm^{-1} and 846 cm^{-1} (Raman). In proteins, the presence of $\nu C{=}O$ of the amino acids side chain at 1702 cm^{-1}, a band that can only be detected by IR, amide I (parallel β-sheet) at 1622 cm^{-1}, (random coil) 1654 cm^{-1} (IR) and 1658 cm^{-1} (Raman), amide III (random coil) at 1244 cm^{-1} (IR), 1242 cm^{-1} (Raman), and (β-sheet) at 1228 cm^{-1} (IR) showed a higher impact of the drug combination which can be explain by the MTX mechanism of action. This drug inhibits the dihydrofolate reductase (DHFR) enzyme, minimizing the cellular pools of thymidylate and purines, which leads to a decrease in the nucleic acid synthesis. The phospholipids ($\nu C{=}O_{ester}$) at 1738 cm^{-1} (IR) and δCH_2 at 1439 cm^{-1} (Raman) presented a higher contribution in the presence of Pd_2SpmCl_4 combination. In contrast, single drug administration has a higher impact on DNA bands (νCC_{ring} – adenine, guanine, and thymine bases) at 1551 cm^{-1} (IR), 1578 cm^{-1}, 1376 cm^{-1} and 1336 cm^{-1}, on deoxyguanine of A-DNA at 670 cm^{-1} and on δCH_2 of the Z-DNA at 1427 cm^{-1} (Raman). Regarding proteins the main discrimination observed was in the Amide I (random coil) at 1654 cm^{-1}, $\nu C{=}C_{porphyrin}$ at 1551 cm^{-1}(IR), phenylalanine ($\nu_s CC_{ring}$) at 1008 cm^{-1}, δNH_3 at 1487 cm^{-1} (Raman), 1479 cm^{-1} and 1407 cm^{-1} (IR). At the lipids level the δCH_2 of membrane lipids at 1389 cm^{-1} (IR), δCH_3 from lipids/acyl chains at 1376 cm^{-1} (Raman), νCC_{acyl} of the *trans* conformation at

1131 cm^{-1}, νCC at 1104 cm^{-1} and νCN at 1106 cm^{-1} (IR), revealed some degreed of single drug administration effect.

The discrimination for $Pd_3Spd_2Cl_6$ in MG-63 is obtained through PC2 e PC3 for FTIR (Figure 26(C)) (explaining 18.7% and 12.6% of total variance, respectively) where the control and single-drug are clearly separated, but the combinations overlaps both conditions. In Raman (Figure 26(F)), PC3 (explaining 10.2% of total variance), a good separation with only a small overlapping of all three conditions. Combination treated cells showed a higher discrimination for DNA biomarkers due to the presence of the νCC_{ring} of guanine at 1560 cm^{-1}, 1340 cm^{-1} and 1315 cm^{-1}, the νCO of RNA ribose at 1124 cm^{-1} (IR) and 1126 cm^{-1} (Raman), in the deoxyribose of B-DNA at 1060 cm^{-1} (IR), and the $\nu OPO_{backbone}$ of Z-DNA at 872 cm^{-1}, 846 cm^{-1} and 748 cm^{-1}(Raman). A higher presence of the Z conformation of DNA in treated cancer cells is desirable since a change of the native conformation to a destruct and irreversible will prevent DNA from replicate. Changes were also observed in proteins such as amide I (antiparallel) at 1677 cm^{-1} and (parallel) at 1625 cm^{-1} (IR), $\nu C{=}C_{porphyrin}$ at 1560 cm^{-1}, δNH_2 at 1401 cm^{-1} (IR) and phenylalanine at 1005 cm^{-1} (Raman). Regarding lipids changes were observed in the δCH_2 at 1315 cm^{-1} and 1152 cm^{-1}, the νCC_{acyl} of the *trans* conformation at 1124 cm^{-1} (IR). However, single drug administration has a higher impact on DNA bands (νCC_{ring} – adenine, guanine, cytosine, and thymine bases) at 1376 cm^{-1} ,1341 cm^{-1}(Raman), and 1165 cm^{-1}(IR), $\nu OPO_{backbone}$ of B-DNA at 786 cm^{-1} (Raman), and δCH_2 of A-DNA at 1712 cm^{-1}(IR). The variations in the nitrogenous bases put in evidence the presence of drug-DNA crosslinks, predominantly interstrand, leading to local unwinding of the native helix. Still, the DNA $OPO_{backbone}$ elongation is the most sensitive peak to recognize cell death since this indicates a collapse of the phosphodiester bonds in the double helix. In proteins, especially in the amide I (random coil) at 1656 cm^{-1} (Raman) and (δNH_3) at 1487 cm^{-1} presented a higher damage in the presence of single drug than with combination. Lipids revealed sensitivity to single drug administration, especially in phospholipids ($\nu C{=}O_{ester}$) at 1739 cm^{-1} (IR) and ($\nu_s PO_2^-$) at 1087 cm^{-1} (Raman), δCH_2 and δCH_3 from aromatic lipids at 1465 cm^{-1} (IR), δCH_3 in lipids and acyl chains at 1376 cm^{-1}, νCC and νCN at 1104 cm^{-1} (Raman).

As expected, polynuclear complexes have higher tendence to change the native DNA conformation to Z-DNA than A-DNA due to the metal atoms which can establish

several bonds with the DNA and the flexibility provided by the ligand chain, allowing not only intra but also inter chain crosslink. For the three cases presented, the drug combination administration has proved to have a higher impact in proteins then in single drug administration, as discussed previously, this may be due to the presence of methotrexate.

3.3.2. HOb Cell Line

For the osteoblasts cell line when treated with cisplatin, the main discrimination obtained for FTIR and Raman is through PC4 (Figure 27(A) and (D)) (explaining 1.5% and 4.8% of total variance, respectively), with some overlapping of all the three conditions. The administration of the drug combination with cisplatin showed impact in some DNA bands, such as RNA/ribose (νCC_{ring}) at 947 cm^{-1}, Z-DNA ($\nu OPO_{backbone}$) at 839 cm^{-1}, and B-DNA/dT (νCC_{ring}) at 786 cm^{-1}, as well as, in some proteins main bands as amide I random coil conformation at 1663 cm^{-1} (Raman) and 1652 cm^{-1} and in lipids bands like phospholipids ($\nu_s PO_2^-$) at 1080 cm^{-1} (IR) and 1086 cm^{-1} (Raman). Single-drug administration on the other hand presented a higher effect on adenine and guanine (νCC_{ring}) at 1573 cm^{-1} (Raman), 1575 cm^{-1}, 1338 cm^{-1} and 1315 cm^{-1}, on A-DNA (δCH_2) at 1423 cm^{-1} (IR), RNA/A,C (νCC_{ring}) at 1298 cm^{-1}, B-DNA ($\nu OPO_{backbone}$) at 786 cm^{-1} and (νCC_{ring}) 720 cm^{-1}(Raman). The presence of A-DNA in healthy cells is not an adversity, since the conformational change is reversable, despite the presence of $\nu OPO_{backbone}$ from DNA which is in an indicator of cell death. Regarding the proteins content the $\nu C{=}O$ of the amino acid side chain at 1699 cm^{-1}, a biomarker only detected by FTIR, the random coil conformation of amide III at 1241 cm^{-1}(IR), the δNH_3 at 1487 cm^{-1}, and the Phe ($\nu_s CC_{ring}$) at 1000 cm^{-1} (Raman), have shown discrimination in proteins in the presence of a sole administration of cisplatin. Also, in lipids, the δCH_2 at 1315 cm^{-1}, the δCH_3 from lipids and acyl chains at 1375 cm^{-1}, and the δCH_2 and δCH_3 from aromatic lipids, at 1460 cm^{-1}(IR) revealed some level of alteration.

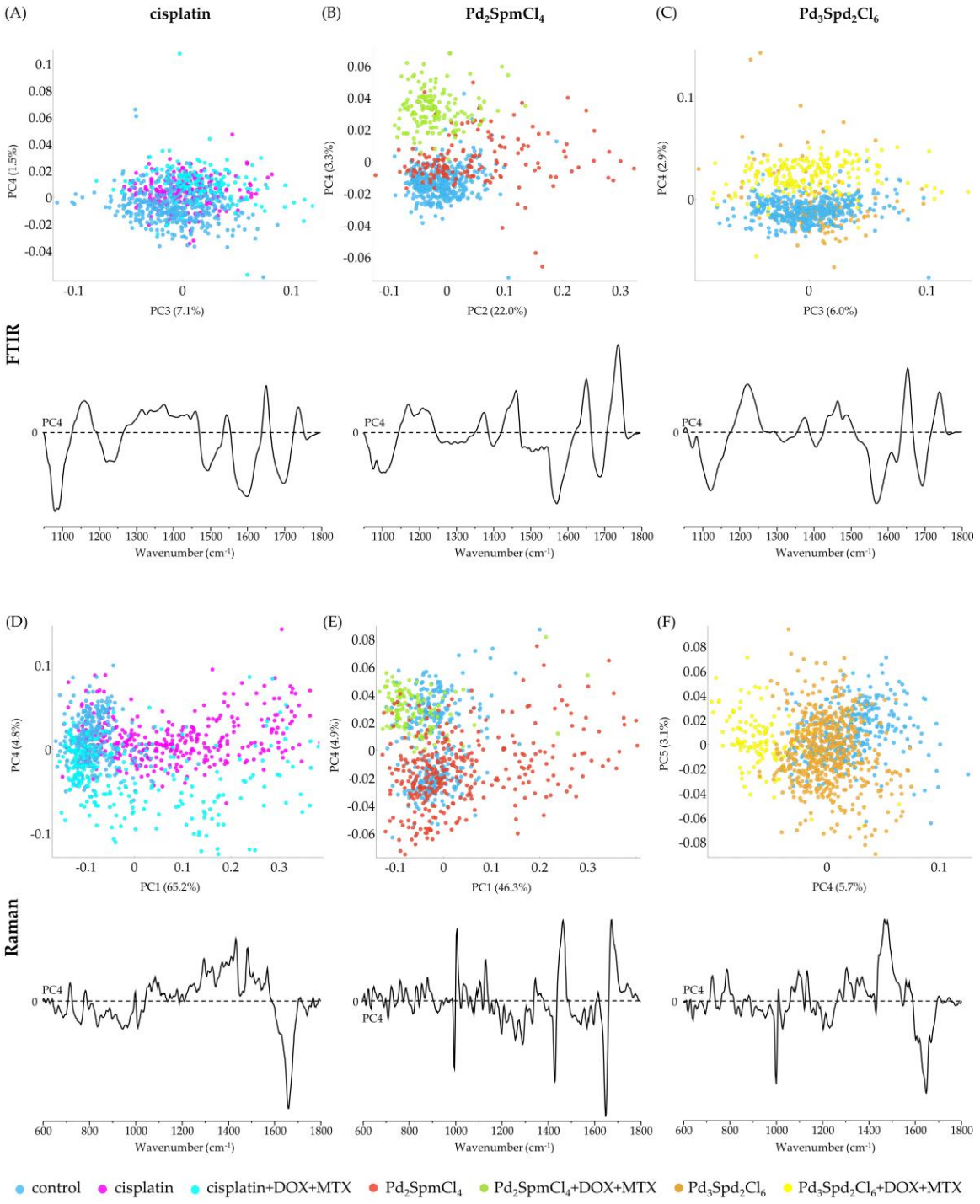

Figure 27: PCA scores and loading plots of FTIR (A,B,C; 1050 – 1800 cm^{-1}) and Raman (D,E,F; 600 – 1800 cm^{-1}) data for HOb cell line, cisplatin (A, D), Pd_2SpmCl_4 (B,E), and $Pd_3Spd_2Cl_6$-treated *vs* their respective combination *vs* control. (For clarity the loadings are offset, the dashed horizontal lines indicating zero loading).

For Pd_2SpmCl_4, PC4 represents the main discrimination for both FTIR and Raman (explaining 3.3% and 4.9% of total variance, respectively) (Figure 27(B) and (E)). For both methods, there is a very good separation of the three conditions under study, with a slight overlapping of Pd_2SpmCl_4 single drug administration with the control. The drug

combination has a higher contribution of DNA nucleobases bands (νCC_{ring} – adenine, guanine, cytosine, and thymine bases) at 1375 cm^{-1} (IR), 1573 cm^{-1} (Raman), 1262 cm^{-1} and 1172 cm^{-1} (IR), also $\nu OPO_{backbone}$ from Z-DNA at 928 cm^{-1} and from RNA at 821 cm^{-1} (Raman). Conformational changes in amide I were detected for random coil at 1653 cm^{-1} and amide III α-helix at 1293 cm^{-1} (Raman), and 1288 cm^{-1}, and δNH_2 at 1401 cm^{-1} (IR). Changes in phospholipids ($\nu C{=}O_{ester}$ and $\nu_s PO_2^-$) were also spotted at 1738 cm^{-1} (IR) and 1084 cm^{-1} (Raman), as well as in aromatic lipids (δCH_2, δCH_3) at 1463 cm^{-1}, lipids/acyl chains (δCH_3) at 1375 cm^{-1} and δCH_2 at 1440 cm^{-1}(IR). In the presence of Pd_2SpmCl_4 alone, discrimination in DNA was observed in A-DNA ($\nu_s PO_2^-$) at 1099 cm^{-1} and B-DNA (deoxyribose νCO) at 1076 cm^{-1} (IR), (dT νCC_{ring}) 765 cm^{-1}, and (A (νCC_{ring}) 728 cm^{-1} (Raman). Besides DNA, proteins were also affected, more precisely the amide I β-sheet (antiparallel) at 1689 cm^{-1} (IR), and the phenylalanine (δCH $\nu O–CH_3$) at 1041 cm^{-1} and ($\nu_s CC_{ring}$) 1004 cm^{-1} (Raman).

As for the principal components already analysed for HOb, PC4 represents the main discrimination obtained for FTIR and Raman for $Pd_3Spd_2Cl_6$ (explaining 2.9% and 5.7% of total variance, respectively) (Figure 27(C) and (F)). In the score obtained for the FTIR, the $Pd_3Spd_2Cl_6$ single drug administration is a little scattered, having the drug combination and the control a clear separation. On the other hand, in Raman drug combination and single drug administration are clearly separated, however the control and single drug administration are overlapped. By the loadings interpretation, the drug combination showed a higher impact in DNA guanine (νCC_{ring}) bands at 1319 cm^{-1} (IR), in Z-DNA conformation (δCH_2) at 1430 cm^{-1}, (dG νCC_{ring}) 620 cm^{-1} and ($\nu OPO_{backbone}$) 848 cm^{-1} (Raman), in B-DNA ($\nu_{as} PO_2^-$) at 1235 cm^{-1} (IR), and dG (νCC_{ring}) at 698 cm^{-1} (Raman). Regarding proteins, the β-sheet presented high intensity bands in amide I (antiparallel) at 1692 cm^{-1} (IR) and amide III at 1235 cm^{-1} (Raman), phenylalanine was also clearly discriminated ($\nu_s CC_{ring}$) at 1005 cm^{-1} and (tCC) 620 cm^{-1}, the νCS and tCC of tyrosine at 641 cm^{-1} (Raman), showed a greater effect with the drug combination treatment. Phospholipids ($\nu C{=}O_{ester}$) at 1739 cm^{-1} (IR), aromatic lipids (δCH_2 and δCH_3) at 1467 cm^{-1} (Raman) and 1465 cm^{-1} (IR), and lipids/acyl chains (δCH_3) at 1376 cm^{-1} (IR) and 1374 cm^{-1} (Raman), are the bands that represent the lipidic impact induced by the drug combination administration. The results from single drug ($Pd_3Spd_2Cl_6$) treated cells, suggest a higher

contribution of the adenine and guanine band (νCC_{ring}) at 1570 cm^{-1} (Raman), the B-DNA/deoxyribose (νCO) at 1074 cm^{-1}(IR) and Z-DNA ($\nu_s PO_2^-$) at 1096 cm^{-1} (Raman). At the proteins and lipids level, the most representative alterations were the δNH_3 at 1482 cm^{-1} (Raman), amide I (random coil) at 1653 cm^{-1} and (parallel) 1623 cm^{-1} (IR), and finally, the νCC_{acyl} from lipids *trans* conformation at 1134 cm^{-1} (Raman).

As reported before for the MG-63 cell line, in HOb cells, the drug combination administration has proved to have a higher impact in proteins when compared to single drug administration, as discussed previously, this may be due to the presence of the MTX.

Both approaches of single drug and drug combination administrations in the HOb cells presented severe damage, and since it is a healthy cell line issues such as secondary effects are implied. To understand the nature of this, result a good solution would be to see if the found effect is reversible meaning that healthy cells will be able to recover after drug removal. This will allow to understand if the deleterious effect is transitory while in presence of the drugs.

4. Conclusions

The present work aimed to explore the effect of polynuclear Pt(II)/Pd(II) complexes, with different types of polyamine ligands, on the cellular response at the biochemical level, through analysis of the vibrational spectral signature of treated (single drug and combined administration) and untreated cells (MG-63 and HOb cell lines). The multidisciplinary approach performed in this study, coupling biochemical cells' viability assay to vibrational spectroscopic techniques, aimed to link the biological response to the spectral signatures of cellular biochemistry, thus identifying spectral markers of drug activity.

The evaluation of the complexes' *in vitro* cytotoxic activity was performed by the MTT assay against the MG-63 cancer cell line, in order to determine their IC_{50} values and choose the best approach and drug concentrations to test against the HOb healthy cell line either alone or in combination with DOX and MTX. The results obtained were compared to cisplatin and Pd_2SpmCl_4. Although $Pt_2Put_2(NH_3)^{4+}$ presented a lower IC_{50} at 48h (11.4 μM) in single drug administration, $Pd_3Spd_2Cl_6$ (13.5 μM) was chosen duo to its mechanism of action similarity to Pd_2SpmCl_4. The outcome of the results of all the combinations used against MG-63 cells agrees to what is described in EURAMOS-1 protocol, the combined administration of Pt(II)/Pd(II) drugs with DOX and MTX presents a much lower cell viability when compared to single drug administration.

Both SR-FTIR and Raman optical spectroscopies allowed access to an accurate description of differences in cellular biochemistry, in the presence of each of the compounds under study and each drug regimen (single or in combination), unveiling vibrational bands assigned to specific spectral biomarkers affected by the compounds directly or indirectly as part of the cells' physiologic response. By analysing the spectral data through multivariate analysis, a clear difference between single drug-treated, combination drug treated and untreated cells was achieved. As expected, the polynuclear complexes under study presented higher DNA conformation changes from the B- native conformation to the Z- conformation while in the presence of cisplatin the native conformation alterations where to an A- conformation. For both cell lines, the drug

combination administration has proved to have a higher impact in proteins when compared to single drug administration.

Future work should focus on: analysing the effect of $Pt_2Put_2(NH_3)^{4+}$ single drug and combination in HOb cell line since have promising results followed by a metabolic impact study through vibrational spectroscopy. Also, a reversibility study should be performed, especially to the HOb cell line, in order to evaluate if the healthy cells can recover from the drug exposure damage after drug removal, not only from the single drug administration, but also the combination. Furthermore, probing the polynuclear complexes influence on DNA *via* THz spectroscopy is of utmost importance in order to evaluate the drug-DNA interaction, specifically the DNA's low frequency modes, comprising the SR-farIR results with the ones present in the work (SR-midIR).

5. References

1. Siegel, R.L., Miller, K. D., Wagle, N. S., Jemal, A., *Cancer statistics, 2023.* CA: A Cancer Journal for Clinicians, 2023. **73**(1): p. 17-48.
2. Martins, A.S., Batista de Carvalho, A. L. M., Lamego, I., Marques, M. P. M., Gil, A. M., *Cytotoxicity of Platinum and Palladium Chelates against Osteosarcoma.* ChemistrySelect, 2020. **5**(20): p. 5993-6000.
3. Florencio-Silva, R., Sasso, G., Sasso-Cerri, E., Simões, M. J., Cerri, P. S., *Biology of Bone Tissue: Structure, Function, and Factors That Influence Bone Cells.* BioMed Research International, 2015. **2015**: p. 1-17.
4. Feng, X., *Chemical and Biochemical Basis of Cell-Bone Matrix Interaction in Health and Disease.* Current Chemical Biology, 2009. **3**(2): p. 189-196.
5. Schaffler, M.B., Kennedy, O. D., *Osteocyte Signaling in Bone.* Current Osteoporosis Reports, 2012. **10**(2): p. 118-120.
6. Boyce, B., Yao, Z., Xing, L., *Osteoclasts have Multiple Roles in Bone in Addition to Bone Resorption.* Critical Reviews in Eukaryotic Gene Expression, 2009. **19**(3): p. 171-180.
7. Ottewell, P.D., *The role of osteoblasts in bone metastasis.* Journal of Bone Oncology, 2016. **5**(3): p. 124-127.
8. Hung, P.S., Kuo, Y. C., Chen, H. G., Chiang, H. H., Lee, O. K., *Detection of osteogenic differentiation by differential mineralized matrix production in mesenchymal stromal cells by Raman spectroscopy.* PLoS One, 2013. **8**(5): p. e65438.
9. Keil, L., *Bone Tumors: Primary Bone Cancers.* FP Essentials, 2020. **493**: p. 22-26.
10. Ferguson, J.L., Turner, S. P., *Bone Cancer: Diagnosis and Treatment Principles.* American Family Physician, 2018. **98**(4): p. 205-213.
11. Misaghi, A., Goldin, A., Awad, M., Kulidjian, A. A., *Osteosarcoma: a comprehensive review.* SICOT-J, 2018. **4**(12): p. 1-8.

12. Hu, Z., Wen, S., Huo, Z., Wang, Q., Zhao, J., Wang, Z., Chen, Y., Zhang, L., Zhou, F., Guo, Z., Liu, H., Zhou, S., *Current Status and Prospects of Targeted Therapy for Osteosarcoma.* Cells, 2022. **11**(21): p. 1-19.

13. Pilavaki, P., Gahanbani Ardakani, A., Gikas, P., Constantinidou, A., *Osteosarcoma: Current Concepts and Evolutions in Management Principles.* Journal of Clinical Medicine, 2023. **12**(2785): p. 2785.

14. Yu, D., Zhang, S., Feng, A., Xu, D., Zhu, Q., Mao, Y., Zhao, Y., Lv, Y., Han, C., Liu, R., Tian, Y., *Methotrexate, doxorubicin, and cisplatinum regimen is still the preferred option for osteosarcoma chemotherapy: A meta-analysis and clinical observation.* Medicine 2019. **98**(19): p. e15582.

15. Whelan, J.S., Bielack, S. S., Marina, N., Smeland, S., Jovic, G., Hook, J. M., Krailo, M., Anninga, J., Butterfass-Bahloul, T., Böhling, T., Calaminus, G., Capra, M., Deffenbaugh, C., Dhooge, C., Eriksson, M., Flanagan, A. M., Gelderblom, H., Goorin, A., Gorlick, R., Gosheger, G., Grimer, R. J., Hall, K. S., Helmke, K., Hogendoorn, P. C.W., Jundt, G., Kager, L., Kuehne, T., Lau, C. C., Letson, G. D., Meyer, J., Meyers, P. A., Morris, C., Mottl, H., Nadel, H., Nagarajan, R., Randall, R. L., Schomberg, P., Schwarz, R., Teot, L. A., Sydes, M. R., Bernstein, M., Pickering, J., Joffe, N., Kevric, M., Sorg, B., Villaluna, D., Wang, C. H., Perisoglou, M., Trani, L., Potratz, J., Carrle, D., Wilhelm, M., Zils, K., Teske, C., *EURAMOS-1, an international randomised study for osteosarcoma: results from pre-randomisation treatment.* Annals of Oncology, 2015. **26**(2): p. 407-414.

16. Isakoff, M.S., Bielack, S. S., Meltzer , P., Gorlick, R., *Osteosarcoma: Current Treatment and a Collaborative Pathway to Success.* Journal of Clinical Oncology, 2015. **33**(27): p. 3029-3035.

17. Fiuza, S.M., Holy, J., Batista de Carvalho, L. A. E., Marques, M. P. M., *Biologic activity of a dinuclear Pd(II)-spermine complex toward human breast cancer.* Chemical Biology & Drug Design, 2011. **77**(6): p. 477-488.

18. Rosa, N.M.P., Ferreira, Fhdc, Farrell, N. P., Costa, L. A. S., *TriplatinNC and Biomolecules: Building Models Based on Non-covalent Interactions.* Frontiers in Chemistry, 2019. **7**: p. 307.

19. Prince, S., Mapolie, S., Blanckenberg, A., *Palladium-Based Anti-Cancer Therapeutics*, in *Encyclopedia of Cancer*, M. Schwab, Editor. 2014, Springer Berlin Heidelberg: Berlin, Heidelberg. p. 1-9.

20. Abotaleb, M., Kubatka, P., Caprnda, M., Varghese, E., Zolakova, B., Zubor, P., Opatrilova, R., Kruzliak, P., Stefanicka, P., Busselberg, D., *Chemotherapeutic agents for the treatment of metastatic breast cancer: An update.* Biomed Pharmacother, 2018. **101**: p. 458-477.

21. Galluzzi, L., Senovilla, L., Vitale, I., Michels, J., Martins, I., Kepp, O., Castedo, M., Kroemer, G., *Molecular mechanisms of cisplatin resistance.* Oncogene, 2012. **31**(15): p. 1869-1883.

22. Komeda, S., *Unique platinum–DNA interactions may lead to more effective platinum-based antitumor drugs.* Metallomics, 2011. **3**(7): p. 650-655.

23. Komeda, S., Moulaei, T., Chikuma, M., Odani, A., Kipping, R., Farrell, N. P., Williams, L. D., *The phosphate clamp: a small and independent motif for nucleic acid backbone recognition.* Nucleic Acids Research, 2011. **39**(1): p. 325-336.

24. Komeda, S., Moulaei, T., Woods, K. K., Chikuma, M., Farrell, N. P., Williams, L. D., *A third mode of DNA binding: Phosphate clamps by a polynuclear platinum complex.* Journal of the American Chemical Society, 2006. **128**(50): p. 16092-16103.

25. Silva, J.D., *New Metal-based Strategies Against Lung Cancer – A Combined Cellular Biology and Vibrational Spectroscopy Approach*, in *Department of Life Sciences*. 2022, University of Coimbra (Master Thesis).

26. Alderden, R.A., Hall, M. D., Hambley, T. W., *The Discovery and Development of Cisplatin.* Journal of Chemical Education, 2006. **83**(5): p. 728.

27. Monneret, C., *Platinum anticancer drugs. From serendipity to rational design.* Annales pharmaceutiques françaises, 2011. **69**(6): p. 286-295.

28. Marques, M.P.M., *Platinum and Palladium Polyamine Complexes as Anticancer Agents: The Structural Factor.* ISRN Spectroscopy, 2013. **2013**: p. 1-29.

29. Carneiro, T.J., Martins, A. S., Marques, M. P. M., Gil, A. M., *Metabolic Aspects of Palladium(II) Potential Anti-Cancer Drugs.* Frontiers in Oncology, 2020. **10**: p. 1-8.

30. Ndagi, U., Mhlongo, N., Soliman, M. E., *Metal complexes in cancer therapy - an update from drug design perspective.* Drug Design, Development and Therapy, 2017. **11**: p. 599-616.

31. Marques, M. P. M., Gianolio, D., Cibin, G., Tomkinson, J., Parker, S. F., Valero, R., Pedro Lopes, R., Batista de Carvalho, L. A. E., *A molecular view of cisplatin's mode of action: interplay with DNA bases and acquired resistance.* Physical Chemistry Chemical Physics, 2015. **17**(7): p. 5155-5171.

32. Fiuza, S.M., Amado, A. M., Parker, S. F., Marques, M. P. M. , Batista de Carvalho, L. A. E., *Conformational Insights and Vibrational Study of a Promising Anticancer Agent:The Role of the Ligand in Pd(II)-Amine Complexes* New Journal of Chemistry, 2015. **39**(8): p. 6274-6283.

33. Batista de Carvalho, A. L. M., *Cisplatin-like Compounds as Potential Chemotherapeutics:from the Bench to the Cell*, in *Department of Life Sciences*. 2016, University of Coimbra (Doctoral Thesis).

34. Ivanov, A.V., Khomutov, A. R., *Biogenic Polyamines and Related Metabolites.* Biomolecules, 2021. **12**(1): p. 14.

35. Navarro-Ranninger, C., Zamora, F., Pérez, J. M., López-Solera, I., Martínez-Carrera, S., Masaguer, J. R., Alonso, C., *Palladium(II) salt and complexes of spermidine with a six-member chelate ring. Synthesis, characterization, and initial DNA-binding and antitumor studies.* Journal of Inorganic Biochemistry, 1992. **46**(4): p. 267-279.

36. Batista de Carvalho, A. L. M., Pilling, M., Gardner, P., Doherty, J., Cinque, G., Wehbe, K., Kelley, C., Batista de Carvalho, L. A. E. ,Marques, M. P. M., *Chemotherapeutic response to cisplatin-like drugs in human breast cancer cells probed by vibrational microspectroscopy.* Faraday Discussions, 2016. **187**: p. 273-298.

37. Farrell, N.P., *Platinum formulations as anticancer drugs clinical and pre-clinical studies.* Current topics in medicinal chemistry, 2011: p. 2623-2631.

38. Santos, I.P., Martins, C. B., Batista de Carvalho, L. A. E., Marques, M. P. M., Batista de Carvalho, A. L. M., *Who's Who? Discrimination of Human Breast Cancer Cell Lines by Raman and FTIR Microspectroscopy.* Cancers (Basel), 2022. **14**(2): p. 1-19.

39. Laginha, R.C., Martins, C. B., Brandao, A. L. C., Marques, J., Marques, M. P. M., Batista de Carvalho, L. A. E., Santos, I. P., Batista de Carvalho, A. L. M., *Evaluation of the Cytotoxic Effect of Pd_2Spm against Prostate Cancer through Vibrational Microspectroscopies.* International Journal of Molecular Sciences, 2023. **24**(3): p. 1888.

40. Silva, J.D., Marques, J., Santos, I. P., Batista de Carvalho, A. L. M., Martins, C. B., Laginha, R. C., Batista de Carvalho, L. A. E., Marques, M. P. M., *A Non-Conventional Platinum Drug against a Non-Small Cell Lung Cancer Line.* Molecules, 2023. **28**(4): p. 1698.

41. Matos, C.S., Batista de Carvalho, A. L. M., Lopes, R. P., Marques, M. P. M., *New strategies against prostate cancer--Pt(II)-based chemotherapy.* Current Medicinal Chemistry, 2012. **19**(27): p. 4678-4687.

42. Hehre, W.J., Radom, L., Schleyer, P. V. R., Pople, J. A., *Ab Initio Molecular Orbital Theory*. 1986: Wiley-Interscience publication.

43. Jensen, F., *Introduction to Computational Chemistry*. Second Edition ed. 2007: John Wiley & Sons Ltd.

44. Foresman, J.B., *Computational Chemistry: A Practical Guide for Applying Techniques to Real World Problems.* Journal of the American Chemical Society, 2001. **123**(41): p. 10142-10143.

45. Gil, V.M.S., *Orbitais em átomos e moléculas.* 1996: Fundação Calouste Gulbenkian.

46. Minenkov, Y., Singstad, A., Occhipinti, G., Jensen, V. R., *The accuracy of DFT-optimized geometries of functional transition metal compounds: a validation study of catalysts for olefin metathesis and other reactions in the homogeneous phase.* Dalton Trans, 2012. **41**(18): p. 5526-5541.

47. Lucaciu, R.L., Hangan, A. C., Sevastre, B., Oprean, L. S., *Metallo-Drugs in Cancer Therapy: Past, Present and Future.* Molecules, 2022. **27**(19): p. 6485.

48. Tzeliou, C.E., Tzeli, D., *Metallocene-Naphthalimide Derivatives: The Effect of Geometry, DFT Methodology, and Transition Metals on Absorption Spectra*. Molecules, 2023. **28**(8): p. 3565.

49. Halsey-Moore, C., Jena, P., Mcleskey, J. T., *Tuning range-separated DFT functionals for modeling the peak absorption of MEH-PPV polymer in various solvents.* Computational and Theoretical Chemistry, 2019. **1162**: p. 1-33.

50. Rossikhin, V.V., Kuz'menko, V. V., Voronkov, E. O., Zaslavskaya, L. I., *Improvement of STO and GTO Basis Set Quality in Calculations of Magnetic Properties by the Coupled and Uncoupled Hartree–Fock Perturbation Theory.* The Journal of Physical Chemistry, 1996. **100**(51): p. 19801-19807.

51. Dedieu, A., *Theoretical Studies in Palladium and Platinum Molecular Chemistry.* Chemical Reviews, 2000. **100**(2): p. 543-600.

52. Yang, Y., M.N. Weaver, and K.M. Merz, Jr., *Assessment of the "6-31+G** + LANL2DZ" Mixed Basis Set Coupled with Density Functional Theory Methods and the Effective Core Potential: Prediction of Heats of Formation and Ionization Potentials for First-Row-Transition-Metal Complexes.* The Journal of Physical Chemistry A, 2009. **113**(36): p. 9843-9851.

53. Liu, W., Franke, R, *Comprehensive relativistic ab initio and density functional theory studies on PtH, PtF, PtCl, and Pt(NH3)2Cl2.* Journal of Computational Chemistry, 2002. **23**(5): p. 564-575.

54. Burton, J.D., *The MTT assay to evaluate chemosensitivity.* Methods in Molecular Medicine, 2005. **110**: p. 69-78.

55. Machado, N.F.L., *Chromone Derivatives as Antioxidant Agents The Structural Variable*, in *Department of Life Sciences*. 2012, University of Coimbra (Doctoral Thesis).

56. Atkins, P.W., Shiver, D. F., Langford, C. H, *Inorganic Chemistry*. 2ª Edition ed. 1994: Oxford University Press.

57. Baker, M.J., Trevisan, J., Bassan, P., Bhargava, R., Butler, H. J., Dorling, K. M., Fielden, P. R., Fogarty, S. W., Fullwood, N. J., Heys, K. A., Hughes, C., Lasch, P., Martin-Hirsch, P. L., Obinaju, B., Sockalingum, G. D., Sule-Suso, J., Strong, R. J.,

Walsh, M. J., Wood, B. R., Gardner, P., Martin, F. L., *Using Fourier transform IR spectroscopy to analyze biological materials.* Nature Protocols, 2014. **9**(8): p. 1771-1791.

58. Carr, G.L., *Resolution limits for infrared microspectroscopy explored with synchrotron radiation.* Review of Scientific Instruments, 2001. **72**(3): p. 1613-1619.

59. Cinque, G., Frogley, M., Wehbe, K., Filik, J., Pijanka, J., *Multimode InfraRed Imaging and Microspectroscopy (MIRIAM) Beamline at Diamond.* Synchrotron Radiation News, 2011. **24**(5): p. 24.

60. Skoog, D.A., Hanlan, J., West, D.M., *Principles of Instrumental Analysis*. Seventh Edition ed. 2016: Cengage Learning.

61. Byrne, H.J., Bonnier, F., Casey, A., Maher, M., McIntyre, J., Efeoglu, E., Farhane, Z., *Advancing Raman microspectroscopy for cellular and subcellular analysis: towards in vitro high-content spectralomic analysis.* Applied Optics, 2018. **57**(22): p. E11-e19.

62. Spadea, A., Denbigh, J., Lawrence, M. J., Kansiz, M., Gardner, P., *Analysis of Fixed and Live Single Cells Using Optical Photothermal Infrared with Concomitant Raman Spectroscopy.* Analytical Chemistry, 2021. **93**(8): p. 3938-3950.

63. Quaroni, L., *Infrared microscopy in the study of cellular biochemistry.* Infrared Physics & Technology, 2020. **105**: p. 102779.

64. Wehbe, K., Filik, J., Frogley, M. D., Cinque, G., *The effect of optical substrates on micro-FTIR analysis of single mammalian cells.* Analytical and Bioanalytical Chemistry, 2013. **405**(4): p. 1311-1324.

65. Wehbe, K., Forfar, I., Eimer, S., Cinque, G., *Discrimination between two different grades of human glioma based on blood vessel infrared spectral imaging.* Analytical and Bioanalytical Chemistry, 2015. **407**(24): p. 7295-7305.

66. Navarro-Ranninger, C., Ochoa, P. A., Pérez, J. M., González, V. M., Masaguer, J. R., Alonso, C., *Platinum (II) and (IV) spermidine complexes. Synthesis, characterization, and biological studies.* Journal of Inorganic Biochemistry, 1994. **53**(3): p. 177-190.

67. Navarro-Ranninger, C., Pérez, J. M., Zamora, F., González, V. M., Masaguer, J. R., Alonso, C., *Palladium (II) compounds of putrescine and spermine. Synthesis,*

characterization, and DNA-binding and antitumor properties. Journal of Inorganic Biochemistry, 1993. **52**(1): p. 37-49.

68. Farrell, N., Qu, Y., *Chemistry of bis(platinum) complexes. Formation of trans derivatives from tetraamine complexes.* Inorganic Chemistry, 1989. **28**(18): p. 3416-3420.

69. Lamego, I.D., *Evaluation of the metabolomic responce of osteosarcoma cells to conventional and new anticancer drugs by NMR metabolomics*, in *Chemistry Department*. 2015, University of Aveiro (Doctoral Thesis).

70. Martins, A.S., *Metabolic biomarkers of platinum and palladium drugs in osteosarcoma: A nuclear magnetic resonance metabolomics study*, in *Chemistry Department*. 2022, University of Aveiro (Doctoral Thesis).

71. Toplak, M., Read, S. T., Sandt, C., Borondics, F., *Quasar: Easy Machine Learning for Biospectroscopy.* Cells, 2021. **10**(9): p. 2300.

72. Toplak, M., Birarda, G.,Read, S., Sandt, C., Rosendahl, S., Vaccari, L., Demšar, J., Borondics, F., *Infrared Orange: Connecting Hyperspectral Data with Machine Learning.* Synchrotron Radiation News, 2017. **30**: p. 40-45.

73. Zapata Trujillo, J.C., McKemmish, L. K., *Model Chemistry Recommendations for Scaled Harmonic Frequency Calculations: A Benchmark Study.* The Journal of Physical Chemistry A, 2023. **127**(7): p. 1715-1735.

74. Amado, A.M., Otero, J. C., Marques, M. P. M., Batista de Carvalho, L. A. E., *Spectroscopic and theoretical studies on solid 1,2-ethylenediamine dihydrochloride salt.* Chemphyschem, 2004. **5**(12): p. 1837-1847.

75. Vojtek, M., Martins, C. B., Ramos, R., Duarte, S. G., Ferreira, I., Batista de Carvalho, A. L. M., Marques, M. P. M., Diniz, C., *Pd(II) and Pt(II) Trinuclear Chelates with Spermidine: Selective Anticancer Activity towards TNBC-Sensitive and -Resistant to Cisplatin.* Pharmaceutics, 2023. **15**(4): p. 1205.

76. Fiuza, S. M., Amado, A. M., Oliveira, P. J., Sardao, V. A., Batista de Carvalho, L. A. E., Marques, M. P. M., *Pt(II) vs Pd(II) Polyamine Complexes as New Anticancer Drugs: A Structure- Activity Study.* Letters in Drug Design & Discovery, 2006. **3**(3): p. 149-151.

77. Batista de Carvalho, A. L. M., Medeiros, P. S., Costa, F. M., Ribeiro, V. P., Sousa, J. B., Diniz, C., Marques, M. P. M., *Anti-Invasive and Anti-Proliferative Synergism between Docetaxel and a Polynuclear Pd-Spermine Agent.* PLoS One, 2016. **11**(11): p. e0167218.

78. Tummala, R., Diegelman, P., Fiuza, S. M., Batista de Carvalho, L. A. E., Marques, M. P. M., Kramer, D. L., Clark, K., Vujcic, S., Porter, C. W., Pendyala, L., *Characterization of Pt-, Pd-spermine complexes for their effect on polyamine pathway and cisplatin resistance in A2780 ovarian carcinoma cells.* Oncology Reports, 2010. **24**(1): p. 15-24.

79. Sun, W., Sanderson, P. E., Zheng, W., *Drug combination therapy increases successful drug repositioning.* Drug Discovery Today, 2016. **21**(7): p. 1189-1195.

80. Malyutina, A., Majumder, M. M., Wang, W., Pessia, A., Heckman, C. A., Tang, J., *Drug combination sensitivity scoring facilitates the discovery of synergistic and efficacious drug combinations in cancer.* PLOS Computational Biology, 2019. **15**(5): p. e1006752.

81. Gilad, Y., Gellerman, G., Lonard, D. M., O'Malley, B. W., *Drug Combination in Cancer Treatment-From Cocktails to Conjugated Combinations.* Cancers (Basel), 2021. **13**(4): p. 669.

82. Perut, F., Graziani, G., Roncuzzi, L., Zini, N., Avnet, S., Baldini, N., *FT-IR Spectral Signature of Sensitive and Multidrug-Resistant Osteosarcoma Cell-Derived Extracellular Nanovesicles.* Cells, 2022. **11**(5): p. 778.

83. Wang, H., Li, J., Qin, J., Li, J., Chen, Y., Song, D., Zeng, H., Wang, S., *Investigating the cellular responses of osteosarcoma to cisplatin by confocal Raman microspectroscopy.* Journal of Photochemistry and Photobiology B: Biology, 2022. **226**: p. 112366.

84. Lasalvia, M., Capozzi, V., Perna, G., *Comparison of FTIR spectra of different breast cell lines to detect spectral biomarkers of pathology.* Infrared Physics & Technology, 2022. **120**: p. 103976.

85. Lasalvia, M., Capozzi, V., Perna, G., *Discrimination of Different Breast Cell Lines on Glass Substrate by Means of Fourier Transform Infrared Spectroscopy.* Sensors (Basel), 2021. **21**(21): p. 6992.

86. Mohammadzadeh, A., Jouyban, A., Hasanzadeh, M., Shafiei-Irannejad, V., Soleymani, J., *Ultrasensitive fluorescence detection of antitumor drug methotrexate based on a terbium-doped silica dendritic probe.* Analytical Methods, 2021. **13**(37): p. 4280-4289.

87. Pascu, M.L., Staicu, A., Voicu, L., Brezeanu, M., Carstocea, B., Pascu, R., Gazdaru, D., *Methotrexate as a photosensitiser.* Anticancer Research, 2004. **24**(5a): p. 2925-2930.

88. Poppitt, D.G., McGown, A. T., Fox, B. W., *The use of a fluorescent methotrexate probe to monitor the effects of three vinca alkaloids on a mixed population of parental L1210 and gene-amplified methotrexate-resistant cells by flow cytometry.* Cancer Chemotherapy and Pharmacology, 1984. **13**(1): p. 54-57.

Figures Index

Tables Index

Abbreviations

A	Adenine
ANOVA	Analysis of Variance
ATR	Attenuated Total Reflection
C	Cytosine
c.a.	*circa*
CCD	Charge-Coupled Device
DFT	Density functional theory
dG	Deoxyguanine
DHFR	Dihydrofolate Reductase
DMSO	Dimethyl Sulfoxide
DNA	Deoxyribonucleic Acid
DOX	Doxorubicin
dT	Deoxythymine
DTGS	Deuterated Triglycine Sulphate
ECPs	Effective Core Potentials
E.coli	Escherichia coli
EDTA	Ethylenediaminetetraacetic acid
e.g.	*exempli gratia* (for example)
EURAMOS-1	European and American Osteosarcoma Study
FBS	Fetal Bovine Serum
FIR	Far Infrared
FTIR	Fourier-Transform Infrared Spectroscopy
G	Guanine
Glu	Glucose
GTO	Gaussian Type Orbital
HBSS	Hanks' Balanced Salt Solution
HF	Hartree-Fock
Hyp	Hydroxyproline
IC_{50}	Half Maximal Inhibitory Concentration

ICCC	International Classification of Childhood Cancer
i.e.	*Id est*.
IR	Infrared
LCAO	Linear Combination of Atomic Orbitals
LDA	Local Density Approximation
LANL2DZ	Los Alamos National Laboratory 2 of Double Zeta
MAP	Methotrexate, Adriamycin and cisPlatin
MCT	Mercury Cadmium Telluride
MEM	Minimum Essential Medium
Met	Methionine
MIRIAM	Multimode InfraRed Imaging And Microspectroscopy
MO	Molecular Orbital
MTT	3-(4,5-Dimethylthiazol-2-yl)-2,5-Diphenyltetrazolium Bromide
MTX	Methotrexate
NADPH	Nicotinamide Adenine Dinucleotide Phosphate
NIR	Near Infrared
OS	Osteosarcoma
PBS	Phosphate-Buffered Saline
PC	Principal Component
PCA	Principal Component Analysis
Pen/Strep	Penicillin-Streptomycin
pH	Potential of Hydrogen
Phe	Phenylalanine
Pro	Proline
Put	Putrescine
QFM-UC	Unidade de I&D Química-Física Molecular
RECPs	Relativistic Effective Core Potentials
RNA	Ribonucleic Acid
RMieS	Resonant Mie Scattering
S/N	Signal to Noise

SARS	Structure-activity relationships
SCF	Self-Consistent Field
SD	Standard Deviation
Spd	Spermidine
Spm	Spermine
SR	Synchrotron Radiation
STO	Slater Type Orbital
Sym	Symmetric
T	Thymine
Trp	Tryptophan
Tyr	Tyrosine
U	Uracil
UHTS	Ultra-High-Throughput Spectrometer
UK	United Kingdom
UV	Ultraviolet
VIS-NIR	Visible and Near Infrared
vs	*versus*
WHO	World Health Organization

Appendices

Appendix A

$Pd_3Spd_2Cl_6$

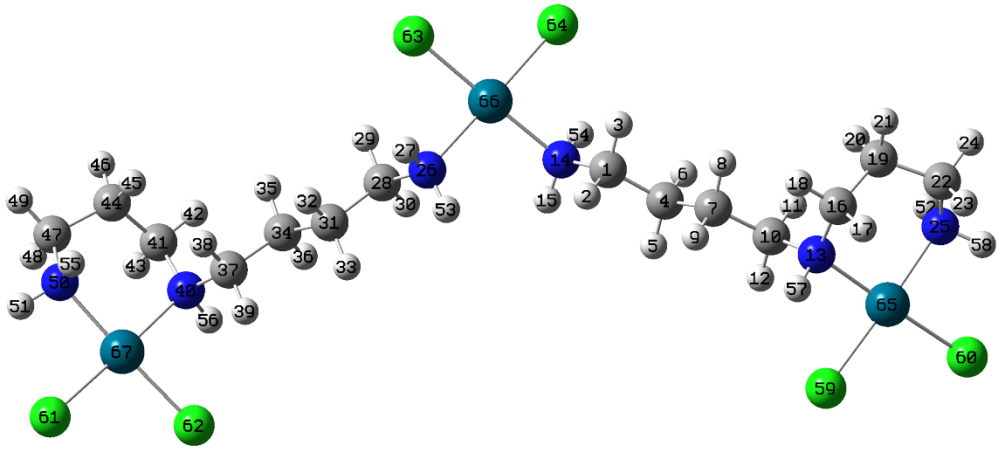

Figure A1: Structural representation of $Pd_3Spd_2Cl_6$ with the atoms numbering.

Table A1: Converging parameter for $Pd_3Spd_2Cl_6$.

Item	Value	Threshold	Converged?
Maximum Force	0.000000	0.000015	YES
RMS	0.000000	0.000010	YES
Maximum Displacement	0.000056	0.000060	YES
RMS Displacement	0.000016	0.000040	YES
Predicted change in Energy= - 3.369386D-11			
Stationary point found.			

Table A2: Optimized parameters for the stationary point geometry found for $Pd_3Spd_2Cl_6$.

Optimized Parameters				
(Angstroms and Degrees)				
***Name**	**Definition**	**Value**	**Derivative**	**Value**
R1	R(1,2)	1.0951	-DE/DX =	0.0
R2	R(1,3)	1.0932	-DE/DX =	0.0
R3	R(1,4)	1.5258	-DE/DX =	0.0
R4	R(1,14)	1.4791	-DE/DX =	0.0
R5	R(4,5)	1.0984	-DE/DX =	0.0
R6	R(4,6)	1.0986	-DE/DX =	0.0
R7	R(4,7)	1.5302	-DE/DX =	0.0

R8	R(7,8)	1.097	-DE/DX =	0.0
R9	R(7,9)	1.0986	-DE/DX =	0.0
R10	R(7,10)	1.5286	-DE/DX =	0.0
R11	R(10,11)	1.0949	-DE/DX =	0.0
R12	R(10,12)	1.0939	-DE/DX =	0.0
R13	R(10,13)	1.4794	-DE/DX =	0.0
R14	R(13,16)	1.4762	-DE/DX =	0.0
R15	R(13,57)	1.0223	-DE/DX =	0.0
R16	R(13,65)	2.1096	-DE/DX =	0.0
R17	R(14,15)	1.0191	-DE/DX =	0.0
R18	R(14,54)	1.0217	-DE/DX =	0.0
R19	R(14,66)	2.1163	-DE/DX =	0.0
R20	R(16,17)	1.0947	-DE/DX =	0.0
R21	R(16,18)	1.0965	-DE/DX =	0.0
R22	R(16,19)	1.5288	-DE/DX =	0.0
R23	R(19,20)	1.098	-DE/DX =	0.0
R24	R(19,21)	1.0954	-DE/DX =	0.0
R25	R(19,22)	1.5276	-DE/DX =	0.0
R26	R(22,23)	1.0942	-DE/DX =	0.0
R27	R(22,24)	1.0967	-DE/DX =	0.0
R28	R(22,25)	1.4737	-DE/DX =	0.0
R29	R(25,52)	1.0193	-DE/DX =	0.0
R30	R(25,58)	1.0221	-DE/DX =	0.0
R31	R(25,65)	2.1011	-DE/DX =	0.0
R32	R(26,27)	1.0217	-DE/DX =	0.0
R33	R(26,28)	1.4791	-DE/DX =	0.0
R34	R(26,53)	1.0191	-DE/DX =	0.0
R35	R(26,66)	2.1163	-DE/DX =	0.0
R36	R(28,29)	1.0932	-DE/DX =	0.0
R37	R(28,30)	1.0951	-DE/DX =	0.0
R38	R(28,31)	1.5258	-DE/DX =	0.0
R39	R(31,32)	1.0986	-DE/DX =	0.0
R40	R(31,33)	1.0984	-DE/DX =	0.0
R41	R(31,34)	1.5302	-DE/DX =	0.0
R42	R(34,35)	1.097	-DE/DX =	0.0
R43	R(34,36)	1.0986	-DE/DX =	0.0
R44	R(34,37)	1.5286	-DE/DX =	0.0
R45	R(37,38)	1.0949	-DE/DX =	0.0
R46	R(37,39)	1.0939	-DE/DX =	0.0
R47	R(37,40)	1.4794	-DE/DX =	0.0
R48	R(40,41)	1.4762	-DE/DX =	0.0

R49	R(40,56)	1.0223	-DE/DX =	0.0
R50	R(40,67)	2.1096	-DE/DX =	0.0
R51	R(41,42)	1.0965	-DE/DX =	0.0
R52	R(41,43)	1.0947	-DE/DX =	0.0
R53	R(41,44)	1.5288	-DE/DX =	0.0
R54	R(44,45)	1.098	-DE/DX =	0.0
R55	R(44,46)	1.0954	-DE/DX =	0.0
R56	R(44,47)	1.5276	-DE/DX =	0.0
R57	R(47,48)	1.0942	-DE/DX =	0.0
R58	R(47,49)	1.0967	-DE/DX =	0.0
R59	R(47,50)	1.4737	-DE/DX =	0.0
R60	R(50,51)	1.0221	-DE/DX =	0.0
R61	R(50,55)	1.0193	-DE/DX =	0.0
R62	R(50,67)	2.1011	-DE/DX =	0.0
R63	R(59,65)	2.3244	-DE/DX =	0.0
R64	R(60,65)	2.3163	-DE/DX =	0.0
R65	R(61,67)	2.3163	-DE/DX =	0.0
R66	R(62,67)	2.3244	-DE/DX =	0.0
R67	R(63,66)	2.3188	-DE/DX =	0.0
R68	R(64,66)	2.3188	-DE/DX =	0.0
A1	A(2,1,3)	107.7163	-DE/DX =	0.0
A2	A(2,1,4)	110.9659	-DE/DX =	0.0
A3	A(2,1,14)	107.8695	-DE/DX =	0.0
A4	A(3,1,4)	110.549	-DE/DX =	0.0
A5	A(3,1,14)	106.329	-DE/DX =	0.0
A6	A(4,1,14)	113.1527	-DE/DX =	0.0
A7	A(1,4,5)	110.2196	-DE/DX =	0.0
A8	A(1,4,6)	108.8491	-DE/DX =	0.0
A9	A(1,4,7)	111.6636	-DE/DX =	0.0
A10	A(5,4,6)	106.922	-DE/DX =	0.0
A11	A(5,4,7)	109.5981	-DE/DX =	0.0
A12	A(6,4,7)	109.4665	-DE/DX =	0.0
A13	A(4,7,8)	108.9053	-DE/DX =	0.0
A14	A(4,7,9)	109.6677	-DE/DX =	0.0
A15	A(4,7,10)	110.9547	-DE/DX =	0.0
A16	A(8,7,9)	107.0879	-DE/DX =	0.0
A17	A(8,7,10)	110.8291	-DE/DX =	0.0
A18	A(9,7,10)	109.3128	-DE/DX =	0.0
A19	A(7,10,11)	110.387	-DE/DX =	0.0
A20	A(7,10,12)	110.0238	-DE/DX =	0.0
A21	A(7,10,13)	114.8108	-DE/DX =	0.0

A22	A(11,10,12)	107.175	-DE/DX =	0.0
A23	A(11,10,13)	108.6046	-DE/DX =	0.0
A24	A(12,10,13)	105.4745	-DE/DX =	0.0
A25	A(10,13,16)	116.34	-DE/DX =	0.0
A26	A(10,13,57)	107.1457	-DE/DX =	0.0
A27	A(10,13,65)	110.2449	-DE/DX =	0.0
A28	A(16,13,57)	108.9542	-DE/DX =	0.0
A29	A(16,13,65)	113.7783	-DE/DX =	0.0
A30	A(57,13,65)	98.6859	-DE/DX =	0.0
A31	A(1,14,15)	110.6937	-DE/DX =	0.0
A32	A(1,14,54)	108.8385	-DE/DX =	0.0
A33	A(1,14,66)	113.1812	-DE/DX =	0.0
A34	A(15,14,54)	107.4093	-DE/DX =	0.0
A35	A(15,14,66)	114.9808	-DE/DX =	0.0
A36	A(54,14,66)	100.9863	-DE/DX =	0.0
A37	A(13,16,17)	106.5773	-DE/DX =	0.0
A38	A(13,16,18)	109.9141	-DE/DX =	0.0
A39	A(13,16,19)	114.0806	-DE/DX =	0.0
A40	A(17,16,18)	107.2556	-DE/DX =	0.0
A41	A(17,16,19)	109.5623	-DE/DX =	0.0
A42	A(18,16,19)	109.2116	-DE/DX =	0.0
A43	A(16,19,20)	110.5783	-DE/DX =	0.0
A44	A(16,19,21)	107.3196	-DE/DX =	0.0
A45	A(16,19,22)	115.1945	-DE/DX =	0.0
A46	A(20,19,21)	105.7572	-DE/DX =	0.0
A47	A(20,19,22)	109.9948	-DE/DX =	0.0
A48	A(21,19,22)	107.4848	-DE/DX =	0.0
A49	A(19,22,23)	110.0311	-DE/DX =	0.0
A50	A(19,22,24)	109.3684	-DE/DX =	0.0
A51	A(19,22,25)	112.5353	-DE/DX =	0.0
A52	A(23,22,24)	107.7618	-DE/DX =	0.0
A53	A(23,22,25)	107.141	-DE/DX =	0.0
A54	A(24,22,25)	109.8748	-DE/DX =	0.0
A55	A(22,25,52)	110.8449	-DE/DX =	0.0
A56	A(22,25,58)	111.8033	-DE/DX =	0.0
A57	A(22,25,65)	116.4607	-DE/DX =	0.0
A58	A(52,25,58)	106.2598	-DE/DX =	0.0
A59	A(52,25,65)	108.6908	-DE/DX =	0.0
A60	A(58,25,65)	102.0131	-DE/DX =	0.0
A61	A(27,26,28)	108.8385	-DE/DX =	0.0
A62	A(27,26,53)	107.4093	-DE/DX =	0.0

A63	A(27,26,66)	100.9863	-DE/DX =	0.0
A64	A(28,26,53)	110.6937	-DE/DX =	0.0
A65	A(28,26,66)	113.1812	-DE/DX =	0.0
A66	A(53,26,66)	114.9808	-DE/DX =	0.0
A67	A(26,28,29)	106.329	-DE/DX =	0.0
A68	A(26,28,30)	107.8695	-DE/DX =	0.0
A69	A(26,28,31)	113.1527	-DE/DX =	0.0
A70	A(29,28,30)	107.7163	-DE/DX =	0.0
A71	A(29,28,31)	110.549	-DE/DX =	0.0
A72	A(30,28,31)	110.9659	-DE/DX =	0.0
A73	A(28,31,32)	108.8491	-DE/DX =	0.0
A74	A(28,31,33)	110.2196	-DE/DX =	0.0
A75	A(28,31,34)	111.6636	-DE/DX =	0.0
A76	A(32,31,33)	106.922	-DE/DX =	0.0
A77	A(32,31,34)	109.4665	-DE/DX =	0.0
A78	A(33,31,34)	109.5981	-DE/DX =	0.0
A79	A(31,34,35)	108.9053	-DE/DX =	0.0
A80	A(31,34,36)	109.6677	-DE/DX =	0.0
A81	A(31,34,37)	110.9547	-DE/DX =	0.0
A82	A(35,34,36)	107.0879	-DE/DX =	0.0
A83	A(35,34,37)	110.8291	-DE/DX =	0.0
A84	A(36,34,37)	109.3128	-DE/DX =	0.0
A85	A(34,37,38)	110.387	-DE/DX =	0.0
A86	A(34,37,39)	110.0238	-DE/DX =	0.0
A87	A(34,37,40)	114.8108	-DE/DX =	0.0
A88	A(38,37,39)	107.175	-DE/DX =	0.0
A89	A(38,37,40)	108.6046	-DE/DX =	0.0
A90	A(39,37,40)	105.4745	-DE/DX =	0.0
A91	A(37,40,41)	116.34	-DE/DX =	0.0
A92	A(37,40,56)	107.1457	-DE/DX =	0.0
A93	A(37,40,67)	110.2449	-DE/DX =	0.0
A94	A(41,40,56)	108.9542	-DE/DX =	0.0
A95	A(41,40,67)	113.7783	-DE/DX =	0.0
A96	A(56,40,67)	98.6859	-DE/DX =	0.0
A97	A(40,41,42)	109.9141	-DE/DX =	0.0
A98	A(40,41,43)	106.5773	-DE/DX =	0.0
A99	A(40,41,44)	114.0806	-DE/DX =	0.0
A100	A(42,41,43)	107.2556	-DE/DX =	0.0
A101	A(42,41,44)	109.2116	-DE/DX =	0.0
A102	A(43,41,44)	109.5623	-DE/DX =	0.0
A103	A(41,44,45)	110.5783	-DE/DX =	0.0

A104	A(41,44,46)	107.3196	-DE/DX =	0.0
A105	A(41,44,47)	115.1945	-DE/DX =	0.0
A106	A(45,44,46)	105.7572	-DE/DX =	0.0
A107	A(45,44,47)	109.9948	-DE/DX =	0.0
A108	A(46,44,47)	107.4848	-DE/DX =	0.0
A109	A(44,47,48)	110.0311	-DE/DX =	0.0
A110	A(44,47,49)	109.3684	-DE/DX =	0.0
A111	A(44,47,50)	112.5353	-DE/DX =	0.0
A112	A(48,47,49)	107.7618	-DE/DX =	0.0
A113	A(48,47,50)	107.141	-DE/DX =	0.0
A114	A(49,47,50)	109.8748	-DE/DX =	0.0
A115	A(47,50,51)	111.8033	-DE/DX =	0.0
A116	A(47,50,55)	110.8449	-DE/DX =	0.0
A117	A(47,50,67)	116.4607	-DE/DX =	0.0
A118	A(51,50,55)	106.2598	-DE/DX =	0.0
A119	A(51,50,67)	102.0131	-DE/DX =	0.0
A120	A(55,50,67)	108.6908	-DE/DX =	0.0
A121	A(13,65,25)	92.8726	-DE/DX =	0.0
A122	A(13,65,59)	84.5968	-DE/DX =	0.0
A123	A(25,65,60)	85.5048	-DE/DX =	0.0
A124	A(59,65,60)	97.0263	-DE/DX =	0.0
A125	A(14,66,26)	96.9772	-DE/DX =	0.0
A126	A(14,66,64)	83.7175	-DE/DX =	0.0
A127	A(26,66,63)	83.7175	-DE/DX =	0.0
A128	A(63,66,64)	95.5991	-DE/DX =	0.0
A129	A(40,67,50)	92.8726	-DE/DX =	0.0
A130	A(40,67,62)	84.5968	-DE/DX =	0.0
A131	A(50,67,61)	85.5048	-DE/DX =	0.0
A132	A(61,67,62)	97.0263	-DE/DX =	0.0
D1	D(2,1,4,5)	61.1547	-DE/DX =	0.0
D2	D(2,1,4,6)	178.123	-DE/DX =	0.0
D3	D(2,1,4,7)	-60.9126	-DE/DX =	0.0
D4	D(3,1,4,5)	-179.3954	-DE/DX =	0.0
D5	D(3,1,4,6)	-62.4271	-DE/DX =	0.0
D6	D(3,1,4,7)	58.5373	-DE/DX =	0.0
D7	D(14,1,4,5)	-60.2612	-DE/DX =	0.0
D8	D(14,1,4,6)	56.7071	-DE/DX =	0.0
D9	D(14,1,4,7)	177.6715	-DE/DX =	0.0
D10	D(2,1,14,15)	-62.4303	-DE/DX =	0.0
D11	D(2,1,14,54)	179.7423	-DE/DX =	0.0
D12	D(2,1,14,66)	68.326	-DE/DX =	0.0

D13	D(3,1,14,15)	-177.747	-DE/DX =	0.0
D14	D(3,1,14,54)	64.4256	-DE/DX =	0.0
D15	D(3,1,14,66)	-46.9907	-DE/DX =	0.0
D16	D(4,1,14,15)	60.7139	-DE/DX =	0.0
D17	D(4,1,14,54)	-57.1136	-DE/DX =	0.0
D18	D(4,1,14,66)	-168.5298	-DE/DX =	0.0
D19	D(1,4,7,8)	-54.7017	-DE/DX =	0.0
D20	D(1,4,7,9)	62.186	-DE/DX =	0.0
D21	D(1,4,7,10)	-176.9527	-DE/DX =	0.0
D22	D(5,4,7,8)	-177.1257	-DE/DX =	0.0
D23	D(5,4,7,9)	-60.2381	-DE/DX =	0.0
D24	D(5,4,7,10)	60.6233	-DE/DX =	0.0
D25	D(6,4,7,8)	65.9027	-DE/DX =	0.0
D26	D(6,4,7,9)	-177.2097	-DE/DX =	0.0
D27	D(6,4,7,10)	-56.3484	-DE/DX =	0.0
D28	D(4,7,10,11)	66.5708	-DE/DX =	0.0
D29	D(4,7,10,12)	-51.511	-DE/DX =	0.0
D30	D(4,7,10,13)	-170.2834	-DE/DX =	0.0
D31	D(8,7,10,11)	-54.554	-DE/DX =	0.0
D32	D(8,7,10,12)	-172.6359	-DE/DX =	0.0
D33	D(8,7,10,13)	68.5918	-DE/DX =	0.0
D34	D(9,7,10,11)	-172.3585	-DE/DX =	0.0
D35	D(9,7,10,12)	69.5597	-DE/DX =	0.0
D36	D(9,7,10,13)	-49.2127	-DE/DX =	0.0
D37	D(7,10,13,16)	-57.1388	-DE/DX =	0.0
D38	D(7,10,13,57)	65.0048	-DE/DX =	0.0
D39	D(7,10,13,65)	171.3982	-DE/DX =	0.0
D40	D(11,10,13,16)	66.9561	-DE/DX =	0.0
D41	D(11,10,13,57)	-170.9003	-DE/DX =	0.0
D42	D(11,10,13,65)	-64.5069	-DE/DX =	0.0
D43	D(12,10,13,16)	-178.431	-DE/DX =	0.0
D44	D(12,10,13,57)	-56.2874	-DE/DX =	0.0
D45	D(12,10,13,65)	50.1061	-DE/DX =	0.0
D46	D(10,13,16,17)	168.2631	-DE/DX =	0.0
D47	D(10,13,16,18)	52.3489	-DE/DX =	0.0
D48	D(10,13,16,19)	-70.6931	-DE/DX =	0.0
D49	D(57,13,16,17)	47.0751	-DE/DX =	0.0
D50	D(57,13,16,18)	-68.8391	-DE/DX =	0.0
D51	D(57,13,16,19)	168.1189	-DE/DX =	0.0
D52	D(65,13,16,17)	-61.9391	-DE/DX =	0.0
D53	D(65,13,16,18)	-177.8533	-DE/DX =	0.0

D54	D(65,13,16,19)	59.1047	-DE/DX =	0.0
D55	D(10,13,65,25)	91.3414	-DE/DX =	0.0
D56	D(10,13,65,59)	-88.5447	-DE/DX =	0.0
D57	D(16,13,65,25)	-41.4461	-DE/DX =	0.0
D58	D(16,13,65,59)	138.6677	-DE/DX =	0.0
D59	D(57,13,65,25)	-156.6835	-DE/DX =	0.0
D60	D(57,13,65,59)	23.4303	-DE/DX =	0.0
D61	D(1,14,66,26)	-97.7605	-DE/DX =	0.0
D62	D(1,14,66,64)	83.0433	-DE/DX =	0.0
D63	D(15,14,66,26)	30.8179	-DE/DX =	0.0
D64	D(15,14,66,64)	-148.3783	-DE/DX =	0.0
D65	D(54,14,66,26)	146.0752	-DE/DX =	0.0
D66	D(54,14,66,64)	-33.121	-DE/DX =	0.0
D67	D(13,16,19,20)	54.9371	-DE/DX =	0.0
D68	D(13,16,19,21)	169.8301	-DE/DX =	0.0
D69	D(13,16,19,22)	-70.5321	-DE/DX =	0.0
D70	D(17,16,19,20)	174.3078	-DE/DX =	0.0
D71	D(17,16,19,21)	-70.7992	-DE/DX =	0.0
D72	D(17,16,19,22)	48.8386	-DE/DX =	0.0
D73	D(18,16,19,20)	-68.4859	-DE/DX =	0.0
D74	D(18,16,19,21)	46.4071	-DE/DX =	0.0
D75	D(18,16,19,22)	166.0449	-DE/DX =	0.0
D76	D(16,19,22,23)	-51.4947	-DE/DX =	0.0
D77	D(16,19,22,24)	-169.6813	-DE/DX =	0.0
D78	D(16,19,22,25)	67.9059	-DE/DX =	0.0
D79	D(20,19,22,23)	-177.2649	-DE/DX =	0.0
D80	D(20,19,22,24)	64.5485	-DE/DX =	0.0
D81	D(20,19,22,25)	-57.8643	-DE/DX =	0.0
D82	D(21,19,22,23)	68.052	-DE/DX =	0.0
D83	D(21,19,22,24)	-50.1347	-DE/DX =	0.0
D84	D(21,19,22,25)	-172.5475	-DE/DX =	0.0
D85	D(19,22,25,52)	67.8809	-DE/DX =	0.0
D86	D(19,22,25,58)	-173.7594	-DE/DX =	0.0
D87	D(19,22,25,65)	-57.047	-DE/DX =	0.0
D88	D(23,22,25,52)	-171.0508	-DE/DX =	0.0
D89	D(23,22,25,58)	-52.6911	-DE/DX =	0.0
D90	D(23,22,25,65)	64.0213	-DE/DX =	0.0
D91	D(24,22,25,52)	-54.246	-DE/DX =	0.0
D92	D(24,22,25,58)	64.1137	-DE/DX =	0.0
D93	D(24,22,25,65)	-179.1739	-DE/DX =	0.0
D94	D(22,25,65,13)	41.599	-DE/DX =	0.0

D95	D(22,25,65,60)	-138.159	-DE/DX =	0.0
D96	D(52,25,65,13)	-84.4155	-DE/DX =	0.0
D97	D(52,25,65,60)	95.8265	-DE/DX =	0.0
D98	D(58,25,65,13)	163.6103	-DE/DX =	0.0
D99	D(58,25,65,60)	-16.1477	-DE/DX =	0.0
D100	D(27,26,28,29)	64.4256	-DE/DX =	0.0
D101	D(27,26,28,30)	179.7423	-DE/DX =	0.0
D102	D(27,26,28,31)	-57.1136	-DE/DX =	0.0
D103	D(53,26,28,29)	-177.747	-DE/DX =	0.0
D104	D(53,26,28,30)	-62.4303	-DE/DX =	0.0
D105	D(53,26,28,31)	60.7139	-DE/DX =	0.0
D106	D(66,26,28,29)	-46.9907	-DE/DX =	0.0
D107	D(66,26,28,30)	68.326	-DE/DX =	0.0
D108	D(66,26,28,31)	-168.5298	-DE/DX =	0.0
D109	D(27,26,66,14)	146.0752	-DE/DX =	0.0
D110	D(27,26,66,63)	-33.121	-DE/DX =	0.0
D111	D(28,26,66,14)	-97.7605	-DE/DX =	0.0
D112	D(28,26,66,63)	83.0433	-DE/DX =	0.0
D113	D(53,26,66,14)	30.8179	-DE/DX =	0.0
D114	D(53,26,66,63)	-148.3783	-DE/DX =	0.0
D115	D(26,28,31,32)	56.7071	-DE/DX =	0.0
D116	D(26,28,31,33)	-60.2612	-DE/DX =	0.0
D117	D(26,28,31,34)	177.6715	-DE/DX =	0.0
D118	D(29,28,31,32)	-62.4271	-DE/DX =	0.0
D119	D(29,28,31,33)	-179.3954	-DE/DX =	0.0
D120	D(29,28,31,34)	58.5373	-DE/DX =	0.0
D121	D(30,28,31,32)	178.123	-DE/DX =	0.0
D122	D(30,28,31,33)	61.1547	-DE/DX =	0.0
D123	D(30,28,31,34)	-60.9126	-DE/DX =	0.0
D124	D(28,31,34,35)	-54.7017	-DE/DX =	0.0
D125	D(28,31,34,36)	62.186	-DE/DX =	0.0
D126	D(28,31,34,37)	-176.9527	-DE/DX =	0.0
D127	D(32,31,34,35)	65.9027	-DE/DX =	0.0
D128	D(32,31,34,36)	-177.2097	-DE/DX =	0.0
D129	D(32,31,34,37)	-56.3484	-DE/DX =	0.0
D130	D(33,31,34,35)	-177.1257	-DE/DX =	0.0
D131	D(33,31,34,36)	-60.2381	-DE/DX =	0.0
D132	D(33,31,34,37)	60.6233	-DE/DX =	0.0
D133	D(31,34,37,38)	66.5708	-DE/DX =	0.0
D134	D(31,34,37,39)	-51.511	-DE/DX =	0.0
D135	D(31,34,37,40)	-170.2834	-DE/DX =	0.0

D136	D(35,34,37,38)	-54.554	-DE/DX =	0.0
D137	D(35,34,37,39)	-172.6359	-DE/DX =	0.0
D138	D(35,34,37,40)	68.5918	-DE/DX =	0.0
D139	D(36,34,37,38)	-172.3585	-DE/DX =	0.0
D140	D(36,34,37,39)	69.5597	-DE/DX =	0.0
D141	D(36,34,37,40)	-49.2127	-DE/DX =	0.0
D142	D(34,37,40,41)	-57.1388	-DE/DX =	0.0
D143	D(34,37,40,56)	65.0048	-DE/DX =	0.0
D144	D(34,37,40,67)	171.3982	-DE/DX =	0.0
D145	D(38,37,40,41)	66.9561	-DE/DX =	0.0
D146	D(38,37,40,56)	-170.9003	-DE/DX =	0.0
D147	D(38,37,40,67)	-64.5069	-DE/DX =	0.0
D148	D(39,37,40,41)	-178.431	-DE/DX =	0.0
D149	D(39,37,40,56)	-56.2874	-DE/DX =	0.0
D150	D(39,37,40,67)	50.1061	-DE/DX =	0.0
D151	D(37,40,41,42)	52.3489	-DE/DX =	0.0
D152	D(37,40,41,43)	168.2631	-DE/DX =	0.0
D153	D(37,40,41,44)	-70.6931	-DE/DX =	0.0
D154	D(56,40,41,42)	-68.8391	-DE/DX =	0.0
D155	D(56,40,41,43)	47.0751	-DE/DX =	0.0
D156	D(56,40,41,44)	168.1189	-DE/DX =	0.0
D157	D(67,40,41,42)	-177.8533	-DE/DX =	0.0
D158	D(67,40,41,43)	-61.9391	-DE/DX =	0.0
D159	D(67,40,41,44)	59.1047	-DE/DX =	0.0
D160	D(37,40,67,50)	91.3414	-DE/DX =	0.0
D161	D(37,40,67,62)	-88.5447	-DE/DX =	0.0
D162	D(41,40,67,50)	-41.4461	-DE/DX =	0.0
D163	D(41,40,67,62)	138.6677	-DE/DX =	0.0
D164	D(56,40,67,50)	-156.6835	-DE/DX =	0.0
D165	D(56,40,67,62)	23.4303	-DE/DX =	0.0
D166	D(40,41,44,45)	54.9371	-DE/DX =	0.0
D167	D(40,41,44,46)	169.8301	-DE/DX =	0.0
D168	D(40,41,44,47)	-70.5321	-DE/DX =	0.0
D169	D(42,41,44,45)	-68.4859	-DE/DX =	0.0
D170	D(42,41,44,46)	46.4071	-DE/DX =	0.0
D171	D(42,41,44,47)	166.0449	-DE/DX =	0.0
D172	D(43,41,44,45)	174.3078	-DE/DX =	0.0
D173	D(43,41,44,46)	-70.7992	-DE/DX =	0.0
D174	D(43,41,44,47)	48.8386	-DE/DX =	0.0
D175	D(41,44,47,48)	-51.4947	-DE/DX =	0.0
D176	D(41,44,47,49)	-169.6813	-DE/DX =	0.0

D177	D(41,44,47,50)	67.9059	-DE/DX =	0.0
D178	D(45,44,47,48)	-177.2649	-DE/DX =	0.0
D179	D(45,44,47,49)	64.5485	-DE/DX =	0.0
D180	D(45,44,47,50)	-57.8643	-DE/DX =	0.0
D181	D(46,44,47,48)	68.052	-DE/DX =	0.0
D182	D(46,44,47,49)	-50.1347	-DE/DX =	0.0
D183	D(46,44,47,50)	-172.5475	-DE/DX =	0.0
D184	D(44,47,50,51)	-173.7594	-DE/DX =	0.0
D185	D(44,47,50,55)	67.8809	-DE/DX =	0.0
D186	D(44,47,50,67)	-57.047	-DE/DX =	0.0
D187	D(48,47,50,51)	-52.6911	-DE/DX =	0.0
D188	D(48,47,50,55)	-171.0508	-DE/DX =	0.0
D189	D(48,47,50,67)	64.0213	-DE/DX =	0.0
D190	D(49,47,50,51)	64.1137	-DE/DX =	0.0
D191	D(49,47,50,55)	-54.246	-DE/DX =	0.0
D192	D(49,47,50,67)	-179.1739	-DE/DX =	0.0
D193	D(47,50,67,40)	41.599	-DE/DX =	0.0
D194	D(47,50,67,61)	-138.159	-DE/DX =	0.0
D195	D(51,50,67,40)	163.6103	-DE/DX =	0.0
D196	D(51,50,67,61)	-16.1477	-DE/DX =	0.0
D197	D(55,50,67,40)	-84.4155	-DE/DX =	0.0
D198	D(55,50,67,61)	95.8265	-DE/DX =	0.0

*R bond length, A angles, D dihedral angles for the numbered atoms present in the Figure A1.

$Pt_3Spd_2Cl_6$

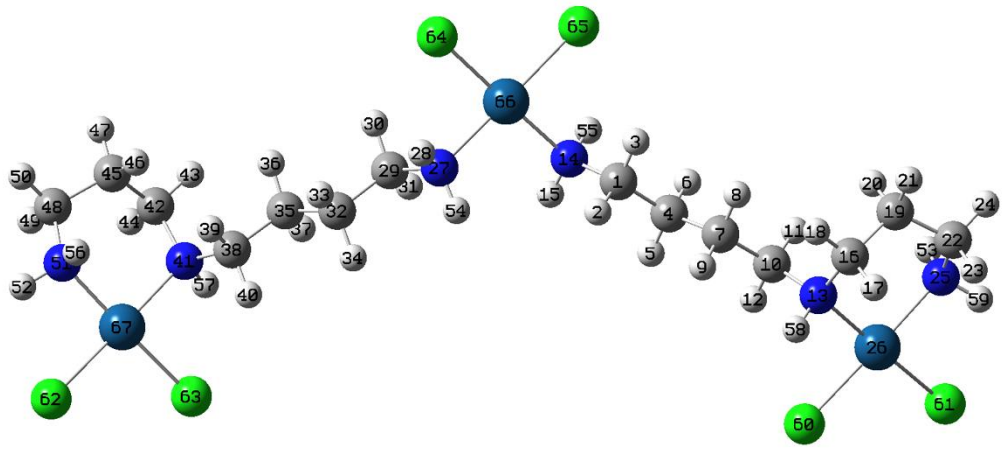

Figure A2: Structural representation of $Pt_3Spd_2Cl_6$ with the atoms numbering.

Table A3: Converging parameter for $Pt_3Spd_2Cl_6$.

Item	Value	Threshold	Converged?

Maximum Force	0.000000	0.000015	YES
RMS	0.000000	0.000010	YES
Maximum Displacement	0.000031	0.000060	YES
RMS Displacement	0.000007	0.000040	YES
Predicted change in Energy= - 1.992362D-10			
Stationary point found.			

Table A4: Optimized parameters for the stationary point geometry found for $Pt_3Spd_2Cl_6$.

Optimized Parameters				
(Angstroms and Degrees)				
***Name**	**Definition**	**Value**	**Derivative**	**Info.**
R1	R(1,2)	1.0947	-DE/DX =	0.0
R2	R(1,3)	1.0928	-DE/DX =	0.0
R3	R(1,4)	1.5245	-DE/DX =	0.0
R4	R(1,14)	1.483	-DE/DX =	0.0
R5	R(4,5)	1.0985	-DE/DX =	0.0
R6	R(4,6)	1.0986	-DE/DX =	0.0
R7	R(4,7)	1.5303	-DE/DX =	0.0
R8	R(7,8)	1.0967	-DE/DX =	0.0
R9	R(7,9)	1.0986	-DE/DX =	0.0
R10	R(7,10)	1.5276	-DE/DX =	0.0
R11	R(10,11)	1.0944	-DE/DX =	0.0
R12	R(10,12)	1.0934	-DE/DX =	0.0
R13	R(10,13)	1.4843	-DE/DX =	0.0
R14	R(13,16)	1.4809	-DE/DX =	0.0
R15	R(13,26)	2.0992	-DE/DX =	0.0
R16	R(13,58)	1.0238	-DE/DX =	0.0
R17	R(14,15)	1.0197	-DE/DX =	0.0
R18	R(14,55)	1.0233	-DE/DX =	0.0
R19	R(14,66)	2.1011	-DE/DX =	0.0
R20	R(16,17)	1.0942	-DE/DX =	0.0
R21	R(16,18)	1.0956	-DE/DX =	0.0
R22	R(16,19)	1.5288	-DE/DX =	0.0
R23	R(19,20)	1.0979	-DE/DX =	0.0
R24	R(19,21)	1.0953	-DE/DX =	0.0
R25	R(19,22)	1.5275	-DE/DX =	0.0
R26	R(22,23)	1.0937	-DE/DX =	0.0
R27	R(22,24)	1.0961	-DE/DX =	0.0
R28	R(22,25)	1.4775	-DE/DX =	0.0

R29	R(25,26)	2.0883	-DE/DX =	0.0
R30	R(25,53)	1.0203	-DE/DX =	0.0
R31	R(25,59)	1.0239	-DE/DX =	0.0
R32	R(26,60)	2.3431	-DE/DX =	0.0
R33	R(26,61)	2.3372	-DE/DX =	0.0
R34	R(27,28)	1.0233	-DE/DX =	0.0
R35	R(27,29)	1.483	-DE/DX =	0.0
R36	R(27,54)	1.0197	-DE/DX =	0.0
R37	R(27,66)	2.1011	-DE/DX =	0.0
R38	R(29,30)	1.0928	-DE/DX =	0.0
R39	R(29,31)	1.0947	-DE/DX =	0.0
R40	R(29,32)	1.5245	-DE/DX =	0.0
R41	R(32,33)	1.0986	-DE/DX =	0.0
R42	R(32,34)	1.0985	-DE/DX =	0.0
R43	R(32,35)	1.5303	-DE/DX =	0.0
R44	R(35,36)	1.0967	-DE/DX =	0.0
R45	R(35,37)	1.0986	-DE/DX =	0.0
R46	R(35,38)	1.5276	-DE/DX =	0.0
R47	R(38,39)	1.0944	-DE/DX =	0.0
R48	R(38,40)	1.0934	-DE/DX =	0.0
R49	R(38,41)	1.4843	-DE/DX =	0.0
R50	R(41,42)	1.4809	-DE/DX =	0.0
R51	R(41,57)	1.0238	-DE/DX =	0.0
R52	R(41,67)	2.0992	-DE/DX =	0.0
R53	R(42,43)	1.0956	-DE/DX =	0.0
R54	R(42,44)	1.0942	-DE/DX =	0.0
R55	R(42,45)	1.5288	-DE/DX =	0.0
R56	R(45,46)	1.0979	-DE/DX =	0.0
R57	R(45,47)	1.0953	-DE/DX =	0.0
R58	R(45,48)	1.5275	-DE/DX =	0.0
R59	R(48,49)	1.0937	-DE/DX =	0.0
R60	R(48,50)	1.0961	-DE/DX =	0.0
R61	R(48,51)	1.4775	-DE/DX =	0.0
R62	R(51,52)	1.0239	-DE/DX =	0.0
R63	R(51,56)	1.0203	-DE/DX =	0.0
R64	R(51,67)	2.0883	-DE/DX =	0.0
R65	R(62,67)	2.3372	-DE/DX =	0.0
R66	R(63,67)	2.3431	-DE/DX =	0.0
R67	R(64,66)	2.3396	-DE/DX =	0.0
R68	R(65,66)	2.3396	-DE/DX =	0.0
A1	A(2,1,3)	107.6857	-DE/DX =	0.0

A2	A(2,1,4)	111.1762	-DE/DX =	0.0
A3	A(2,1,14)	107.8131	-DE/DX =	0.0
A4	A(3,1,4)	110.8808	-DE/DX =	0.0
A5	A(3,1,14)	106.3005	-DE/DX =	0.0
A6	A(4,1,14)	112.7225	-DE/DX =	0.0
A7	A(1,4,5)	110.2431	-DE/DX =	0.0
A8	A(1,4,6)	108.9996	-DE/DX =	0.0
A9	A(1,4,7)	111.5905	-DE/DX =	0.0
A10	A(5,4,6)	106.924	-DE/DX =	0.0
A11	A(5,4,7)	109.5315	-DE/DX =	0.0
A12	A(6,4,7)	109.4343	-DE/DX =	0.0
A13	A(4,7,8)	108.8716	-DE/DX =	0.0
A14	A(4,7,9)	109.5756	-DE/DX =	0.0
A15	A(4,7,10)	110.767	-DE/DX =	0.0
A16	A(8,7,9)	107.1112	-DE/DX =	0.0
A17	A(8,7,10)	111.0699	-DE/DX =	0.0
A18	A(9,7,10)	109.3663	-DE/DX =	0.0
A19	A(7,10,11)	110.7487	-DE/DX =	0.0
A20	A(7,10,12)	110.0301	-DE/DX =	0.0
A21	A(7,10,13)	114.6355	-DE/DX =	0.0
A22	A(11,10,12)	107.1625	-DE/DX =	0.0
A23	A(11,10,13)	108.483	-DE/DX =	0.0
A24	A(12,10,13)	105.4025	-DE/DX =	0.0
A25	A(10,13,16)	115.6967	-DE/DX =	0.0
A26	A(10,13,26)	111.2114	-DE/DX =	0.0
A27	A(10,13,58)	106.4456	-DE/DX =	0.0
A28	A(16,13,26)	113.6222	-DE/DX =	0.0
A29	A(16,13,58)	108.1537	-DE/DX =	0.0
A30	A(26,13,58)	100.2235	-DE/DX =	0.0
A31	A(1,14,15)	110.1719	-DE/DX =	0.0
A32	A(1,14,55)	108.3363	-DE/DX =	0.0
A33	A(1,14,66)	114.2985	-DE/DX =	0.0
A34	A(15,14,55)	106.7473	-DE/DX =	0.0
A35	A(15,14,66)	114.1988	-DE/DX =	0.0
A36	A(55,14,66)	102.3659	-DE/DX =	0.0
A37	A(13,16,17)	106.47	-DE/DX =	0.0
A38	A(13,16,18)	109.6375	-DE/DX =	0.0
A39	A(13,16,19)	113.9903	-DE/DX =	0.0
A40	A(17,16,18)	107.4811	-DE/DX =	0.0
A41	A(17,16,19)	109.6562	-DE/DX =	0.0
A42	A(18,16,19)	109.3811	-DE/DX =	0.0

A43	A(16,19,20)	110.6011	-DE/DX =	0.0
A44	A(16,19,21)	107.2615	-DE/DX =	0.0
A45	A(16,19,22)	115.2451	-DE/DX =	0.0
A46	A(20,19,21)	105.803	-DE/DX =	0.0
A47	A(20,19,22)	109.985	-DE/DX =	0.0
A48	A(21,19,22)	107.4299	-DE/DX =	0.0
A49	A(19,22,23)	110.1898	-DE/DX =	0.0
A50	A(19,22,24)	109.5675	-DE/DX =	0.0
A51	A(19,22,25)	112.3785	-DE/DX =	0.0
A52	A(23,22,24)	108.0352	-DE/DX =	0.0
A53	A(23,22,25)	107.0808	-DE/DX =	0.0
A54	A(24,22,25)	109.4709	-DE/DX =	0.0
A55	A(22,25,26)	116.4367	-DE/DX =	0.0
A56	A(22,25,53)	110.3047	-DE/DX =	0.0
A57	A(22,25,59)	111.1753	-DE/DX =	0.0
A58	A(26,25,53)	108.8543	-DE/DX =	0.0
A59	A(26,25,59)	103.5623	-DE/DX =	0.0
A60	A(53,25,59)	105.8256	-DE/DX =	0.0
A61	A(13,26,25)	93.9201	-DE/DX =	0.0
A62	A(13,26,60)	84.1917	-DE/DX =	0.0
A63	A(25,26,61)	84.9613	-DE/DX =	0.0
A64	A(60,26,61)	96.9267	-DE/DX =	0.0
A65	A(28,27,29)	108.3363	-DE/DX =	0.0
A66	A(28,27,54)	106.7473	-DE/DX =	0.0
A67	A(28,27,66)	102.3659	-DE/DX =	0.0
A68	A(29,27,54)	110.1719	-DE/DX =	0.0
A69	A(29,27,66)	114.2985	-DE/DX =	0.0
A70	A(54,27,66)	114.1988	-DE/DX =	0.0
A71	A(27,29,30)	106.3005	-DE/DX =	0.0
A72	A(27,29,31)	107.8131	-DE/DX =	0.0
A73	A(27,29,32)	112.7225	-DE/DX =	0.0
A74	A(30,29,31)	107.6857	-DE/DX =	0.0
A75	A(30,29,32)	110.8808	-DE/DX =	0.0
A76	A(31,29,32)	111.1762	-DE/DX =	0.0
A77	A(29,32,33)	108.9996	-DE/DX =	0.0
A78	A(29,32,34)	110.2431	-DE/DX =	0.0
A79	A(29,32,35)	111.5905	-DE/DX =	0.0
A80	A(33,32,34)	106.924	-DE/DX =	0.0
A81	A(33,32,35)	109.4343	-DE/DX =	0.0
A82	A(34,32,35)	109.5315	-DE/DX =	0.0
A83	A(32,35,36)	108.8716	-DE/DX =	0.0

A84	A(32,35,37)	109.5756	-DE/DX =	0.0
A85	A(32,35,38)	110.767	-DE/DX =	0.0
A86	A(36,35,37)	107.1112	-DE/DX =	0.0
A87	A(36,35,38)	111.0699	-DE/DX =	0.0
A88	A(37,35,38)	109.3663	-DE/DX =	0.0
A89	A(35,38,39)	110.7487	-DE/DX =	0.0
A90	A(35,38,40)	110.0301	-DE/DX =	0.0
A91	A(35,38,41)	114.6355	-DE/DX =	0.0
A92	A(39,38,40)	107.1625	-DE/DX =	0.0
A93	A(39,38,41)	108.483	-DE/DX =	0.0
A94	A(40,38,41)	105.4025	-DE/DX =	0.0
A95	A(38,41,42)	115.6967	-DE/DX =	0.0
A96	A(38,41,57)	106.4456	-DE/DX =	0.0
A97	A(38,41,67)	111.2114	-DE/DX =	0.0
A98	A(42,41,57)	108.1537	-DE/DX =	0.0
A99	A(42,41,67)	113.6222	-DE/DX =	0.0
A100	A(57,41,67)	100.2235	-DE/DX =	0.0
A101	A(41,42,43)	109.6375	-DE/DX =	0.0
A102	A(41,42,44)	106.47	-DE/DX =	0.0
A103	A(41,42,45)	113.9903	-DE/DX =	0.0
A104	A(43,42,44)	107.4811	-DE/DX =	0.0
A105	A(43,42,45)	109.3811	-DE/DX =	0.0
A106	A(44,42,45)	109.6562	-DE/DX =	0.0
A107	A(42,45,46)	110.6011	-DE/DX =	0.0
A108	A(42,45,47)	107.2615	-DE/DX =	0.0
A109	A(42,45,48)	115.2451	-DE/DX =	0.0
A110	A(46,45,47)	105.803	-DE/DX =	0.0
A111	A(46,45,48)	109.985	-DE/DX =	0.0
A112	A(47,45,48)	107.4299	-DE/DX =	0.0
A113	A(45,48,49)	110.1898	-DE/DX =	0.0
A114	A(45,48,50)	109.5675	-DE/DX =	0.0
A115	A(45,48,51)	112.3785	-DE/DX =	0.0
A116	A(49,48,50)	108.0352	-DE/DX =	0.0
A117	A(49,48,51)	107.0808	-DE/DX =	0.0
A118	A(50,48,51)	109.4709	-DE/DX =	0.0
A119	A(48,51,52)	111.1753	-DE/DX =	0.0
A120	A(48,51,56)	110.3047	-DE/DX =	0.0
A121	A(48,51,67)	116.4367	-DE/DX =	0.0
A122	A(52,51,56)	105.8256	-DE/DX =	0.0
A123	A(52,51,67)	103.5623	-DE/DX =	0.0
A124	A(56,51,67)	108.8543	-DE/DX =	0.0

A125	A(14,66,27)	97.6798	-DE/DX =	0.0
A126	A(14,66,65)	83.2041	-DE/DX =	0.0
A127	A(27,66,64)	83.2041	-DE/DX =	0.0
A128	A(64,66,65)	95.9191	-DE/DX =	0.0
A129	A(41,67,51)	93.9201	-DE/DX =	0.0
A130	A(41,67,63)	84.1917	-DE/DX =	0.0
A131	A(51,67,62)	84.9613	-DE/DX =	0.0
A132	A(62,67,63)	96.9267	-DE/DX =	0.0
D1	D(2,1,4,5)	60.7562	-DE/DX =	0.0
D2	D(2,1,4,6)	177.8291	-DE/DX =	0.0
D3	D(2,1,4,7)	-61.1928	-DE/DX =	0.0
D4	D(3,1,4,5)	-179.4764	-DE/DX =	0.0
D5	D(3,1,4,6)	-62.4035	-DE/DX =	0.0
D6	D(3,1,4,7)	58.5746	-DE/DX =	0.0
D7	D(14,1,4,5)	-60.4354	-DE/DX =	0.0
D8	D(14,1,4,6)	56.6375	-DE/DX =	0.0
D9	D(14,1,4,7)	177.6156	-DE/DX =	0.0
D10	D(2,1,14,15)	-63.4157	-DE/DX =	0.0
D11	D(2,1,14,55)	-179.8489	-DE/DX =	0.0
D12	D(2,1,14,66)	66.7498	-DE/DX =	0.0
D13	D(3,1,14,15)	-178.6562	-DE/DX =	0.0
D14	D(3,1,14,55)	64.9106	-DE/DX =	0.0
D15	D(3,1,14,66)	-48.4907	-DE/DX =	0.0
D16	D(4,1,14,15)	59.6714	-DE/DX =	0.0
D17	D(4,1,14,55)	-56.7618	-DE/DX =	0.0
D18	D(4,1,14,66)	-170.1631	-DE/DX =	0.0
D19	D(1,4,7,8)	-55.4243	-DE/DX =	0.0
D20	D(1,4,7,9)	61.4202	-DE/DX =	0.0
D21	D(1,4,7,10)	-177.8327	-DE/DX =	0.0
D22	D(5,4,7,8)	-177.7828	-DE/DX =	0.0
D23	D(5,4,7,9)	-60.9383	-DE/DX =	0.0
D24	D(5,4,7,10)	59.8088	-DE/DX =	0.0
D25	D(6,4,7,8)	65.3002	-DE/DX =	0.0
D26	D(6,4,7,9)	-177.8554	-DE/DX =	0.0
D27	D(6,4,7,10)	-57.1082	-DE/DX =	0.0
D28	D(4,7,10,11)	67.3127	-DE/DX =	0.0
D29	D(4,7,10,12)	-50.98	-DE/DX =	0.0
D30	D(4,7,10,13)	-169.5472	-DE/DX =	0.0
D31	D(8,7,10,11)	-53.8054	-DE/DX =	0.0
D32	D(8,7,10,12)	-172.098	-DE/DX =	0.0
D33	D(8,7,10,13)	69.3347	-DE/DX =	0.0

D34	D(9,7,10,11)	-171.816	-DE/DX =	0.0
D35	D(9,7,10,12)	69.8913	-DE/DX =	0.0
D36	D(9,7,10,13)	-48.6759	-DE/DX =	0.0
D37	D(7,10,13,16)	-58.4797	-DE/DX =	0.0
D38	D(7,10,13,26)	169.9336	-DE/DX =	0.0
D39	D(7,10,13,58)	61.6892	-DE/DX =	0.0
D40	D(11,10,13,16)	65.8692	-DE/DX =	0.0
D41	D(11,10,13,26)	-65.7174	-DE/DX =	0.0
D42	D(11,10,13,58)	-173.9618	-DE/DX =	0.0
D43	D(12,10,13,16)	-179.6234	-DE/DX =	0.0
D44	D(12,10,13,26)	48.7899	-DE/DX =	0.0
D45	D(12,10,13,58)	-59.4545	-DE/DX =	0.0
D46	D(10,13,16,17)	166.753	-DE/DX =	0.0
D47	D(10,13,16,18)	50.7714	-DE/DX =	0.0
D48	D(10,13,16,19)	-72.2159	-DE/DX =	0.0
D49	D(26,13,16,17)	-62.8039	-DE/DX =	0.0
D50	D(26,13,16,18)	-178.7854	-DE/DX =	0.0
D51	D(26,13,16,19)	58.2273	-DE/DX =	0.0
D52	D(58,13,16,17)	47.5167	-DE/DX =	0.0
D53	D(58,13,16,18)	-68.4649	-DE/DX =	0.0
D54	D(58,13,16,19)	168.5478	-DE/DX =	0.0
D55	D(10,13,26,25)	92.3813	-DE/DX =	0.0
D56	D(10,13,26,60)	-87.6463	-DE/DX =	0.0
D57	D(16,13,26,25)	-40.2589	-DE/DX =	0.0
D58	D(16,13,26,60)	139.7134	-DE/DX =	0.0
D59	D(58,13,26,25)	-155.3732	-DE/DX =	0.0
D60	D(58,13,26,60)	24.5991	-DE/DX =	0.0
D61	D(1,14,66,27)	-96.7374	-DE/DX =	0.0
D62	D(1,14,66,65)	83.8989	-DE/DX =	0.0
D63	D(15,14,66,27)	31.4109	-DE/DX =	0.0
D64	D(15,14,66,65)	-147.9529	-DE/DX =	0.0
D65	D(55,14,66,27)	146.3679	-DE/DX =	0.0
D66	D(55,14,66,65)	-32.9959	-DE/DX =	0.0
D67	D(13,16,19,20)	54.4451	-DE/DX =	0.0
D68	D(13,16,19,21)	169.3717	-DE/DX =	0.0
D69	D(13,16,19,22)	-71.0703	-DE/DX =	0.0
D70	D(17,16,19,20)	173.6859	-DE/DX =	0.0
D71	D(17,16,19,21)	-71.3874	-DE/DX =	0.0
D72	D(17,16,19,22)	48.1705	-DE/DX =	0.0
D73	D(18,16,19,20)	-68.6818	-DE/DX =	0.0
D74	D(18,16,19,21)	46.2449	-DE/DX =	0.0

D75	D(18,16,19,22)	165.8028	-DE/DX =	0.0
D76	D(16,19,22,23)	-50.9293	-DE/DX =	0.0
D77	D(16,19,22,24)	-169.6667	-DE/DX =	0.0
D78	D(16,19,22,25)	68.401	-DE/DX =	0.0
D79	D(20,19,22,23)	-176.7621	-DE/DX =	0.0
D80	D(20,19,22,24)	64.5006	-DE/DX =	0.0
D81	D(20,19,22,25)	-57.4318	-DE/DX =	0.0
D82	D(21,19,22,23)	68.5357	-DE/DX =	0.0
D83	D(21,19,22,24)	-50.2017	-DE/DX =	0.0
D84	D(21,19,22,25)	-172.1341	-DE/DX =	0.0
D85	D(19,22,25,26)	-56.2036	-DE/DX =	0.0
D86	D(19,22,25,53)	68.4618	-DE/DX =	0.0
D87	D(19,22,25,59)	-174.4626	-DE/DX =	0.0
D88	D(23,22,25,26)	64.9261	-DE/DX =	0.0
D89	D(23,22,25,53)	-170.4085	-DE/DX =	0.0
D90	D(23,22,25,59)	-53.3329	-DE/DX =	0.0
D91	D(24,22,25,26)	-178.1909	-DE/DX =	0.0
D92	D(24,22,25,53)	-53.5255	-DE/DX =	0.0
D93	D(24,22,25,59)	63.5501	-DE/DX =	0.0
D94	D(22,25,26,13)	40.4327	-DE/DX =	0.0
D95	D(22,25,26,61)	-139.0694	-DE/DX =	0.0
D96	D(53,25,26,13)	-84.9686	-DE/DX =	0.0
D97	D(53,25,26,61)	95.5292	-DE/DX =	0.0
D98	D(59,25,26,13)	162.7712	-DE/DX =	0.0
D99	D(59,25,26,61)	-16.731	-DE/DX =	0.0
D100	D(28,27,29,30)	64.9106	-DE/DX =	0.0
D101	D(28,27,29,31)	-179.8489	-DE/DX =	0.0
D102	D(28,27,29,32)	-56.7618	-DE/DX =	0.0
D103	D(54,27,29,30)	-178.6562	-DE/DX =	0.0
D104	D(54,27,29,31)	-63.4157	-DE/DX =	0.0
D105	D(54,27,29,32)	59.6714	-DE/DX =	0.0
D106	D(66,27,29,30)	-48.4907	-DE/DX =	0.0
D107	D(66,27,29,31)	66.7498	-DE/DX =	0.0
D108	D(66,27,29,32)	-170.1631	-DE/DX =	0.0
D109	D(28,27,66,14)	146.3679	-DE/DX =	0.0
D110	D(28,27,66,64)	-32.9959	-DE/DX =	0.0
D111	D(29,27,66,14)	-96.7374	-DE/DX =	0.0
D112	D(29,27,66,64)	83.8989	-DE/DX =	0.0
D113	D(54,27,66,14)	31.4109	-DE/DX =	0.0
D114	D(54,27,66,64)	-147.9529	-DE/DX =	0.0
D115	D(27,29,32,33)	56.6375	-DE/DX =	0.0

D116	D(27,29,32,34)	-60.4354	-DE/DX =	0.0
D117	D(27,29,32,35)	177.6156	-DE/DX =	0.0
D118	D(30,29,32,33)	-62.4035	-DE/DX =	0.0
D119	D(30,29,32,34)	-179.4764	-DE/DX =	0.0
D120	D(30,29,32,35)	58.5746	-DE/DX =	0.0
D121	D(31,29,32,33)	177.8291	-DE/DX =	0.0
D122	D(31,29,32,34)	60.7562	-DE/DX =	0.0
D123	D(31,29,32,35)	-61.1928	-DE/DX =	0.0
D124	D(29,32,35,36)	-55.4243	-DE/DX =	0.0
D125	D(29,32,35,37)	61.4202	-DE/DX =	0.0
D126	D(29,32,35,38)	-177.8327	-DE/DX =	0.0
D127	D(33,32,35,36)	65.3002	-DE/DX =	0.0
D128	D(33,32,35,37)	-177.8554	-DE/DX =	0.0
D129	D(33,32,35,38)	-57.1082	-DE/DX =	0.0
D130	D(34,32,35,36)	-177.7828	-DE/DX =	0.0
D131	D(34,32,35,37)	-60.9383	-DE/DX =	0.0
D132	D(34,32,35,38)	59.8088	-DE/DX =	0.0
D133	D(32,35,38,39)	67.3127	-DE/DX =	0.0
D134	D(32,35,38,40)	-50.98	-DE/DX =	0.0
D135	D(32,35,38,41)	-169.5472	-DE/DX =	0.0
D136	D(36,35,38,39)	-53.8054	-DE/DX =	0.0
D137	D(36,35,38,40)	-172.098	-DE/DX =	0.0
D138	D(36,35,38,41)	69.3347	-DE/DX =	0.0
D139	D(37,35,38,39)	-171.816	-DE/DX =	0.0
D140	D(37,35,38,40)	69.8913	-DE/DX =	0.0
D141	D(37,35,38,41)	-48.6759	-DE/DX =	0.0
D142	D(35,38,41,42)	-58.4797	-DE/DX =	0.0
D143	D(35,38,41,57)	61.6892	-DE/DX =	0.0
D144	D(35,38,41,67)	169.9336	-DE/DX =	0.0
D145	D(39,38,41,42)	65.8692	-DE/DX =	0.0
D146	D(39,38,41,57)	-173.9618	-DE/DX =	0.0
D147	D(39,38,41,67)	-65.7174	-DE/DX =	0.0
D148	D(40,38,41,42)	-179.6234	-DE/DX =	0.0
D149	D(40,38,41,57)	-59.4545	-DE/DX =	0.0
D150	D(40,38,41,67)	48.7899	-DE/DX =	0.0
D151	D(38,41,42,43)	50.7714	-DE/DX =	0.0
D152	D(38,41,42,44)	166.753	-DE/DX =	0.0
D153	D(38,41,42,45)	-72.2159	-DE/DX =	0.0
D154	D(57,41,42,43)	-68.4649	-DE/DX =	0.0
D155	D(57,41,42,44)	47.5167	-DE/DX =	0.0
D156	D(57,41,42,45)	168.5478	-DE/DX =	0.0

D157	D(67,41,42,43)	-178.7854	-DE/DX =	0.0
D158	D(67,41,42,44)	-62.8039	-DE/DX =	0.0
D159	D(67,41,42,45)	58.2273	-DE/DX =	0.0
D160	D(38,41,67,51)	92.3813	-DE/DX =	0.0
D161	D(38,41,67,63)	-87.6463	-DE/DX =	0.0
D162	D(42,41,67,51)	-40.2589	-DE/DX =	0.0
D163	D(42,41,67,63)	139.7134	-DE/DX =	0.0
D164	D(57,41,67,51)	-155.3732	-DE/DX =	0.0
D165	D(57,41,67,63)	24.5991	-DE/DX =	0.0
D166	D(41,42,45,46)	54.4451	-DE/DX =	0.0
D167	D(41,42,45,47)	169.3717	-DE/DX =	0.0
D168	D(41,42,45,48)	-71.0703	-DE/DX =	0.0
D169	D(43,42,45,46)	-68.6818	-DE/DX =	0.0
D170	D(43,42,45,47)	46.2449	-DE/DX =	0.0
D171	D(43,42,45,48)	165.8028	-DE/DX =	0.0
D172	D(44,42,45,46)	173.6859	-DE/DX =	0.0
D173	D(44,42,45,47)	-71.3874	-DE/DX =	0.0
D174	D(44,42,45,48)	48.1705	-DE/DX =	0.0
D175	D(42,45,48,49)	-50.9293	-DE/DX =	0.0
D176	D(42,45,48,50)	-169.6667	-DE/DX =	0.0
D177	D(42,45,48,51)	68.401	-DE/DX =	0.0
D178	D(46,45,48,49)	-176.7621	-DE/DX =	0.0
D179	D(46,45,48,50)	64.5006	-DE/DX =	0.0
D180	D(46,45,48,51)	-57.4318	-DE/DX =	0.0
D181	D(47,45,48,49)	68.5357	-DE/DX =	0.0
D182	D(47,45,48,50)	-50.2017	-DE/DX =	0.0
D183	D(47,45,48,51)	-172.1341	-DE/DX =	0.0
D184	D(45,48,51,52)	-174.4626	-DE/DX =	0.0
D185	D(45,48,51,56)	68.4618	-DE/DX =	0.0
D186	D(45,48,51,67)	-56.2036	-DE/DX =	0.0
D187	D(49,48,51,52)	-53.3329	-DE/DX =	0.0
D188	D(49,48,51,56)	-170.4085	-DE/DX =	0.0
D189	D(49,48,51,67)	64.9261	-DE/DX =	0.0
D190	D(50,48,51,52)	63.5501	-DE/DX =	0.0
D191	D(50,48,51,56)	-53.5255	-DE/DX =	0.0
D192	D(50,48,51,67)	-178.1909	-DE/DX =	0.0
D193	D(48,51,67,41)	40.4327	-DE/DX =	0.0
D194	D(48,51,67,62)	-139.0694	-DE/DX =	0.0
D195	D(52,51,67,41)	162.7712	-DE/DX =	0.0
D196	D(52,51,67,62)	-16.731	-DE/DX =	0.0
D197	D(56,51,67,41)	-84.9686	-DE/DX =	0.0

D198	D(56,51,67,62)	95.5292	-DE/DX =	0.0

*R bond length, A angles, D dihedral angles for the numbered atoms present in the Figure A2.

$Pd_2Put_2Cl_4$

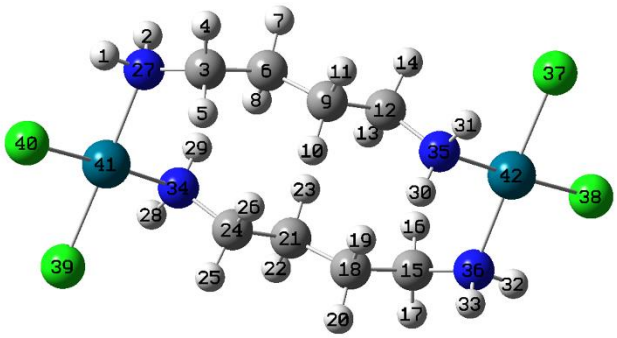

Figure A3: Structural representation of $Pd_2Put_2Cl_4$ with the atoms numbering.

Table A5: Converging parameter for $Pd_2Put_2Cl_4$.

Item	Value	Threshold	Converged?
Maximum Force	0.000011	0.000450	YES
RMS	0.0000002	0.000300	YES
Maximum Displacement	0.001011	0.001800	YES
RMS Displacement	0.000235	0.001200	YES
Predicted change in Energy= - 9.284677D-09			
Stationary point found.			

Table A6: Optimized parameters for the stationary point geometry found for $Pd_2Put_2Cl_4$.

Optimized Parameters				
(Angstroms and Degrees)				
*Name	Definition	Value	Derivative	Info.
R1	R(1,27)	1.0235	-DE/DX =	0.0
R2	R(2,27)	1.0193	-DE/DX =	0.0
R3	R(3,4)	1.0964	-DE/DX =	0.0
R4	R(3,5)	1.0936	-DE/DX =	0.0
R5	R(3,6)	1.528	-DE/DX =	0.0
R6	R(3,27)	1.4806	-DE/DX =	0.0
R7	R(6,7)	1.0971	-DE/DX =	0.0
R8	R(6,8)	1.0961	-DE/DX =	0.0
R9	R(6,9)	1.5298	-DE/DX =	0.0
R10	R(9,10)	1.1004	-DE/DX =	0.0

R11	R(9,11)	1.0969	-DE/DX =	0.0
R12	R(9,12)	1.5271	-DE/DX =	0.0
R13	R(12,13)	1.0946	-DE/DX =	0.0
R14	R(12,14)	1.093	-DE/DX =	0.0
R15	R(12,35)	1.4784	-DE/DX =	0.0
R16	R(15,16)	1.0936	-DE/DX =	0.0
R17	R(15,17)	1.0964	-DE/DX =	0.0
R18	R(15,18)	1.528	-DE/DX =	0.0
R19	R(15,36)	1.4806	-DE/DX =	0.0
R20	R(18,19)	1.0961	-DE/DX =	0.0
R21	R(18,20)	1.0971	-DE/DX =	0.0
R22	R(18,21)	1.5298	-DE/DX =	0.0
R23	R(21,22)	1.0969	-DE/DX =	0.0
R24	R(21,23)	1.1004	-DE/DX =	0.0
R25	R(21,24)	1.5271	-DE/DX =	0.0
R26	R(24,25)	1.093	-DE/DX =	0.0
R27	R(24,26)	1.0946	-DE/DX =	0.0
R28	R(24,34)	1.4784	-DE/DX =	0.0
R29	R(27,41)	2.1422	-DE/DX =	0.0
R30	R(28,34)	1.0211	-DE/DX =	0.0
R31	R(29,34)	1.0187	-DE/DX =	0.0
R32	R(30,35)	1.0187	-DE/DX =	0.0
R33	R(31,35)	1.0211	-DE/DX =	0.0
R34	R(32,36)	1.0235	-DE/DX =	0.0
R35	R(33,36)	1.0193	-DE/DX =	0.0
R36	R(34,41)	2.1212	-DE/DX =	0.0
R37	R(35,42)	2.1212	-DE/DX =	0.0
R38	R(36,42)	2.1422	-DE/DX =	0.0
R39	R(37,42)	2.3158	-DE/DX =	0.0
R40	R(38,42)	2.3157	-DE/DX =	0.0
R41	R(39,41)	2.3158	-DE/DX =	0.0
R42	R(40,41)	2.3157	-DE/DX =	0.0
A1	A(4,3,5)	107.3541	-DE/DX =	0.0
A2	A(4,3,6)	110.072	-DE/DX =	0.0
A3	A(4,3,27)	110.0496	-DE/DX =	0.0
A4	A(5,3,6)	111.0067	-DE/DX =	0.0
A5	A(5,3,27)	106.7476	-DE/DX =	0.0
A6	A(6,3,27)	111.4798	-DE/DX =	0.0
A7	A(3,6,7)	110.2082	-DE/DX =	0.0
A8	A(3,6,8)	108.7168	-DE/DX =	0.0
A9	A(3,6,9)	113.0005	-DE/DX =	0.0

A10	A(7,6,8)	106.2473	-DE/DX =	0.0
A11	A(7,6,9)	110.1461	-DE/DX =	0.0
A12	A(8,6,9)	108.2662	-DE/DX =	0.0
A13	A(6,9,10)	108.4763	-DE/DX =	0.0
A14	A(6,9,11)	110.7352	-DE/DX =	0.0
A15	A(6,9,12)	111.405	-DE/DX =	0.0
A16	A(10,9,11)	106.5862	-DE/DX =	0.0
A17	A(10,9,12)	109.0595	-DE/DX =	0.0
A18	A(11,9,12)	110.4257	-DE/DX =	0.0
A19	A(9,12,13)	109.6054	-DE/DX =	0.0
A20	A(9,12,14)	112.1989	-DE/DX =	0.0
A21	A(9,12,35)	113.6369	-DE/DX =	0.0
A22	A(13,12,14)	106.8266	-DE/DX =	0.0
A23	A(13,12,35)	107.7569	-DE/DX =	0.0
A24	A(14,12,35)	106.4887	-DE/DX =	0.0
A25	A(16,15,17)	107.3541	-DE/DX =	0.0
A26	A(16,15,18)	111.0067	-DE/DX =	0.0
A27	A(16,15,36)	106.7476	-DE/DX =	0.0
A28	A(17,15,18)	110.072	-DE/DX =	0.0
A29	A(17,15,36)	110.0496	-DE/DX =	0.0
A30	A(18,15,36)	111.4798	-DE/DX =	0.0
A31	A(15,18,19)	108.7168	-DE/DX =	0.0
A32	A(15,18,20)	110.2082	-DE/DX =	0.0
A33	A(15,18,21)	113.0005	-DE/DX =	0.0
A34	A(19,18,20)	106.2473	-DE/DX =	0.0
A35	A(19,18,21)	108.2662	-DE/DX =	0.0
A36	A(20,18,21)	110.1461	-DE/DX =	0.0
A37	A(18,21,22)	110.7352	-DE/DX =	0.0
A38	A(18,21,23)	108.4763	-DE/DX =	0.0
A39	A(18,21,24)	111.405	-DE/DX =	0.0
A40	A(22,21,23)	106.5862	-DE/DX =	0.0
A41	A(22,21,24)	110.4257	-DE/DX =	0.0
A42	A(23,21,24)	109.0595	-DE/DX =	0.0
A43	A(21,24,25)	112.1989	-DE/DX =	0.0
A44	A(21,24,26)	109.6054	-DE/DX =	0.0
A45	A(21,24,34)	113.6369	-DE/DX =	0.0
A46	A(25,24,26)	106.8266	-DE/DX =	0.0
A47	A(25,24,34)	106.4887	-DE/DX =	0.0
A48	A(26,24,34)	107.7569	-DE/DX =	0.0
A49	A(1,27,2)	106.9068	-DE/DX =	0.0
A50	A(1,27,3)	109.6114	-DE/DX =	0.0

A51	A(1,27,41)	97.2493	-DE/DX =	0.0
A52	A(2,27,3)	110.6423	-DE/DX =	0.0
A53	A(2,27,41)	114.0093	-DE/DX =	0.0
A54	A(3,27,41)	117.08	-DE/DX =	0.0
A55	A(24,34,28)	109.5335	-DE/DX =	0.0
A56	A(24,34,29)	110.9614	-DE/DX =	0.0
A57	A(24,34,41)	112.4343	-DE/DX =	0.0
A58	A(28,34,29)	107.5278	-DE/DX =	0.0
A59	A(28,34,41)	102.2566	-DE/DX =	0.0
A60	A(29,34,41)	113.6077	-DE/DX =	0.0
A61	A(12,35,30)	110.9614	-DE/DX =	0.0
A62	A(12,35,31)	109.5335	-DE/DX =	0.0
A63	A(12,35,42)	112.4343	-DE/DX =	0.0
A64	A(30,35,31)	107.5278	-DE/DX =	0.0
A65	A(30,35,42)	113.6077	-DE/DX =	0.0
A66	A(31,35,42)	102.2566	-DE/DX =	0.0
A67	A(15,36,32)	109.6114	-DE/DX =	0.0
A68	A(15,36,33)	110.6423	-DE/DX =	0.0
A69	A(15,36,42)	117.08	-DE/DX =	0.0
A70	A(32,36,33)	106.9068	-DE/DX =	0.0
A71	A(32,36,42)	97.2493	-DE/DX =	0.0
A72	A(33,36,42)	114.0093	-DE/DX =	0.0
A73	A(27,41,34)	98.7178	-DE/DX =	0.0
A74	A(27,41,40)	83.3885	-DE/DX =	0.0
A75	A(34,41,39)	83.1822	-DE/DX =	0.0
A76	A(39,41,40)	94.7045	-DE/DX =	0.0
A77	A(35,42,36)	98.7178	-DE/DX =	0.0
A78	A(35,42,37)	83.1822	-DE/DX =	0.0
A79	A(36,42,38)	83.3885	-DE/DX =	0.0
A80	A(37,42,38)	94.7045	-DE/DX =	0.0
D1	D(4,3,6,7)	-39.9161	-DE/DX =	0.0
D2	D(4,3,6,8)	-155.9878	-DE/DX =	0.0
D3	D(4,3,6,9)	83.7914	-DE/DX =	0.0
D4	D(5,3,6,7)	-158.6331	-DE/DX =	0.0
D5	D(5,3,6,8)	85.2953	-DE/DX =	0.0
D6	D(5,3,6,9)	-34.9256	-DE/DX =	0.0
D7	D(27,3,6,7)	82.4976	-DE/DX =	0.0
D8	D(27,3,6,8)	-33.574	-DE/DX =	0.0
D9	D(27,3,6,9)	-153.7949	-DE/DX =	0.0
D10	D(4,3,27,1)	-41.6832	-DE/DX =	0.0
D11	D(4,3,27,2)	75.971	-DE/DX =	0.0

D12	D(4,3,27,41)	-151.1114	-DE/DX =	0.0
D13	D(5,3,27,1)	74.5104	-DE/DX =	0.0
D14	D(5,3,27,2)	-167.8355	-DE/DX =	0.0
D15	D(5,3,27,41)	-34.9179	-DE/DX =	0.0
D16	D(6,3,27,1)	-164.1098	-DE/DX =	0.0
D17	D(6,3,27,2)	-46.4556	-DE/DX =	0.0
D18	D(6,3,27,41)	86.462	-DE/DX =	0.0
D19	D(3,6,9,10)	52.7156	-DE/DX =	0.0
D20	D(3,6,9,11)	-63.9197	-DE/DX =	0.0
D21	D(3,6,9,12)	172.7675	-DE/DX =	0.0
D22	D(7,6,9,10)	176.4573	-DE/DX =	0.0
D23	D(7,6,9,11)	59.822	-DE/DX =	0.0
D24	D(7,6,9,12)	-63.4908	-DE/DX =	0.0
D25	D(8,6,9,10)	-67.7626	-DE/DX =	0.0
D26	D(8,6,9,11)	175.6021	-DE/DX =	0.0
D27	D(8,6,9,12)	52.2893	-DE/DX =	0.0
D28	D(6,9,12,13)	-47.4628	-DE/DX =	0.0
D29	D(6,9,12,14)	71.0427	-DE/DX =	0.0
D30	D(6,9,12,35)	-168.079	-DE/DX =	0.0
D31	D(10,9,12,13)	72.2443	-DE/DX =	0.0
D32	D(10,9,12,14)	-169.2503	-DE/DX =	0.0
D33	D(10,9,12,35)	-48.372	-DE/DX =	0.0
D34	D(11,9,12,13)	-170.9518	-DE/DX =	0.0
D35	D(11,9,12,14)	-52.4463	-DE/DX =	0.0
D36	D(11,9,12,35)	68.432	-DE/DX =	0.0
D37	D(9,12,35,30)	41.939	-DE/DX =	0.0
D38	D(9,12,35,31)	-76.6235	-DE/DX =	0.0
D39	D(9,12,35,42)	170.4111	-DE/DX =	0.0
D40	D(13,12,35,30)	-79.7119	-DE/DX =	0.0
D41	D(13,12,35,31)	161.7255	-DE/DX =	0.0
D42	D(13,12,35,42)	48.7601	-DE/DX =	0.0
D43	D(14,12,35,30)	165.9711	-DE/DX =	0.0
D44	D(14,12,35,31)	47.4085	-DE/DX =	0.0
D45	D(14,12,35,42)	-65.5568	-DE/DX =	0.0
D46	D(16,15,18,19)	-85.2953	-DE/DX =	0.0
D47	D(16,15,18,20)	158.6331	-DE/DX =	0.0
D48	D(16,15,18,21)	34.9256	-DE/DX =	0.0
D49	D(17,15,18,19)	155.9878	-DE/DX =	0.0
D50	D(17,15,18,20)	39.9161	-DE/DX =	0.0
D51	D(17,15,18,21)	-83.7914	-DE/DX =	0.0
D52	D(36,15,18,19)	33.574	-DE/DX =	0.0

D53	D(36,15,18,20)	-82.4976	-DE/DX =	0.0
D54	D(36,15,18,21)	153.7949	-DE/DX =	0.0
D55	D(16,15,36,32)	-74.5104	-DE/DX =	0.0
D56	D(16,15,36,33)	167.8355	-DE/DX =	0.0
D57	D(16,15,36,42)	34.9179	-DE/DX =	0.0
D58	D(17,15,36,32)	41.6832	-DE/DX =	0.0
D59	D(17,15,36,33)	-75.971	-DE/DX =	0.0
D60	D(17,15,36,42)	151.1114	-DE/DX =	0.0
D61	D(18,15,36,32)	164.1098	-DE/DX =	0.0
D62	D(18,15,36,33)	46.4556	-DE/DX =	0.0
D63	D(18,15,36,42)	-86.462	-DE/DX =	0.0
D64	D(15,18,21,22)	63.9197	-DE/DX =	0.0
D65	D(15,18,21,23)	-52.7156	-DE/DX =	0.0
D66	D(15,18,21,24)	-172.7675	-DE/DX =	0.0
D67	D(19,18,21,22)	-175.6021	-DE/DX =	0.0
D68	D(19,18,21,23)	67.7626	-DE/DX =	0.0
D69	D(19,18,21,24)	-52.2893	-DE/DX =	0.0
D70	D(20,18,21,22)	-59.822	-DE/DX =	0.0
D71	D(20,18,21,23)	-176.4573	-DE/DX =	0.0
D72	D(20,18,21,24)	63.4908	-DE/DX =	0.0
D73	D(18,21,24,25)	-71.0427	-DE/DX =	0.0
D74	D(18,21,24,26)	47.4628	-DE/DX =	0.0
D75	D(18,21,24,34)	168.079	-DE/DX =	0.0
D76	D(22,21,24,25)	52.4463	-DE/DX =	0.0
D77	D(22,21,24,26)	170.9518	-DE/DX =	0.0
D78	D(22,21,24,34)	-68.432	-DE/DX =	0.0
D79	D(23,21,24,25)	169.2503	-DE/DX =	0.0
D80	D(23,21,24,26)	-72.2443	-DE/DX =	0.0
D81	D(23,21,24,34)	48.372	-DE/DX =	0.0
D82	D(21,24,34,28)	76.6235	-DE/DX =	0.0
D83	D(21,24,34,29)	-41.939	-DE/DX =	0.0
D84	D(21,24,34,41)	-170.4111	-DE/DX =	0.0
D85	D(25,24,34,28)	-47.4085	-DE/DX =	0.0
D86	D(25,24,34,29)	-165.9711	-DE/DX =	0.0
D87	D(25,24,34,41)	65.5568	-DE/DX =	0.0
D88	D(26,24,34,28)	-161.7255	-DE/DX =	0.0
D89	D(26,24,34,29)	79.7119	-DE/DX =	0.0
D90	D(26,24,34,41)	-48.7601	-DE/DX =	0.0
D91	D(1,27,41,34)	170.6807	-DE/DX =	0.0
D92	D(1,27,41,40)	-10.6448	-DE/DX =	0.0
D93	D(2,27,41,34)	58.4965	-DE/DX =	0.0

D94	D(2,27,41,40)	-122.829	-DE/DX =	0.0
D95	D(3,27,41,34)	-72.8934	-DE/DX =	0.0
D96	D(3,27,41,40)	105.7811	-DE/DX =	0.0
D97	D(24,34,41,27)	95.1915	-DE/DX =	0.0
D98	D(24,34,41,39)	-84.4791	-DE/DX =	0.0
D99	D(28,34,41,27)	-147.4302	-DE/DX =	0.0
D100	D(28,34,41,39)	32.8993	-DE/DX =	0.0
D101	D(29,34,41,27)	-31.8809	-DE/DX =	0.0
D102	D(29,34,41,39)	148.4486	-DE/DX =	0.0
D103	D(12,35,42,36)	-95.1915	-DE/DX =	0.0
D104	D(12,35,42,37)	84.4791	-DE/DX =	0.0
D105	D(30,35,42,36)	31.8809	-DE/DX =	0.0
D106	D(30,35,42,37)	-148.4486	-DE/DX =	0.0
D107	D(31,35,42,36)	147.4302	-DE/DX =	0.0
D108	D(31,35,42,37)	-32.8993	-DE/DX =	0.0
D109	D(15,36,42,35)	72.8934	-DE/DX =	0.0
D110	D(15,36,42,38)	-105.7811	-DE/DX =	0.0
D111	D(32,36,42,35)	-170.6807	-DE/DX =	0.0
D112	D(32,36,42,38)	10.6448	-DE/DX =	0.0
D113	D(33,36,42,35)	-58.4965	-DE/DX =	0.0
D114	D(33,36,42,38)	122.829	-DE/DX =	0.0

*R bond length, A angles, D dihedral angles for the numbered atoms present in the Figure A3.

$Pt_2Put_2(NH_3)_4^{4+}$

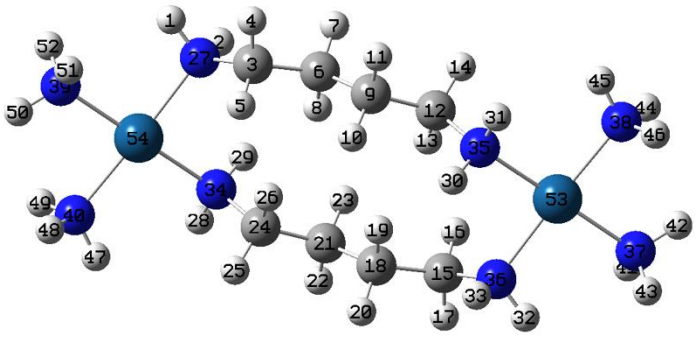

Figure A4: Structural representation of $Pt_2Put_2(NH_3)_4^{4+}$ with the atoms numbering.

Table A7: Converging parameter for $Pt_2Put_2(NH_3)_4^{4+}$.

Item	Value	Threshold	Converged?
Maximum Force	0.000004	0.000450	YES
RMS	0.0000001	0.000300	YES

Maximum Displacement	0.000626	0.001800	YES
RMS Displacement	0.000106	0.001200	YES
Predicted change in Energy= - 1.588085D-09			
Stationary point found.			

Table A8: Optimized parameters for the stationary point geometry found for $Pt_2Put_2(NH_3)_4^{4+}$.

Optimized Parameters				
(Angstroms and Degrees)				
***Name**	**Definition**	**Value**	**Derivative**	**Info.**
R1	R(1,2)	1.5312	-DE/DX =	0.0
R2	R(1,3)	1.536	-DE/DX =	0.0
R3	R(1,7)	1.1003	-DE/DX =	0.0
R4	R(1,8)	1.0958	-DE/DX =	0.0
R5	R(2,4)	1.5073	-DE/DX =	0.0
R6	R(2,5)	1.0925	-DE/DX =	0.0
R7	R(2,6)	1.0931	-DE/DX =	0.0
R8	R(3,9)	1.5274	-DE/DX =	0.0
R9	R(3,10)	1.0964	-DE/DX =	0.0
R10	R(3,11)	1.099	-DE/DX =	0.0
R11	R(4,12)	1.0216	-DE/DX =	0.0
R12	R(4,13)	1.0228	-DE/DX =	0.0
R13	R(4,54)	2.1051	-DE/DX =	0.0
R14	R(9,14)	1.4998	-DE/DX =	0.0
R15	R(9,15)	1.0929	-DE/DX =	0.0
R16	R(9,16)	1.0943	-DE/DX =	0.0
R17	R(14,17)	1.0253	-DE/DX =	0.0
R18	R(14,18)	1.0234	-DE/DX =	0.0
R19	R(14,53)	2.1236	-DE/DX =	0.0
R20	R(19,20)	1.5327	-DE/DX =	0.0
R21	R(19,21)	1.5466	-DE/DX =	0.0
R22	R(19,22)	1.0951	-DE/DX =	0.0
R23	R(19,23)	1.0986	-DE/DX =	0.0
R24	R(20,24)	1.0938	-DE/DX =	0.0
R25	R(20,25)	1.0917	-DE/DX =	0.0
R26	R(20,28)	1.5012	-DE/DX =	0.0
R27	R(21,26)	1.0947	-DE/DX =	0.0
R28	R(21,27)	1.0977	-DE/DX =	0.0
R29	R(21,34)	1.531	-DE/DX =	0.0
R30	R(28,29)	1.0226	-DE/DX =	0.0

R31	R(28,30)	1.0241	-DE/DX =	0.0
R32	R(28,53)	2.1118	-DE/DX =	0.0
R33	R(31,32)	1.0236	-DE/DX =	0.0
R34	R(31,33)	1.0248	-DE/DX =	0.0
R35	R(31,34)	1.4966	-DE/DX =	0.0
R36	R(31,54)	2.1323	-DE/DX =	0.0
R37	R(34,35)	1.0904	-DE/DX =	0.0
R38	R(34,36)	1.0945	-DE/DX =	0.0
R39	R(37,38)	1.0265	-DE/DX =	0.0
R40	R(37,39)	1.0243	-DE/DX =	0.0
R41	R(37,52)	1.0243	-DE/DX =	0.0
R42	R(37,53)	2.0762	-DE/DX =	0.0
R43	R(40,41)	1.0251	-DE/DX =	0.0
R44	R(40,42)	1.025	-DE/DX =	0.0
R45	R(40,51)	1.0255	-DE/DX =	0.0
R46	R(40,53)	2.0762	-DE/DX =	0.0
R47	R(43,44)	1.0253	-DE/DX =	0.0
R48	R(43,45)	1.0252	-DE/DX =	0.0
R49	R(43,50)	1.0246	-DE/DX =	0.0
R50	R(43,54)	2.0873	-DE/DX =	0.0
R51	R(46,47)	1.0246	-DE/DX =	0.0
R52	R(46,48)	1.0267	-DE/DX =	0.0
R53	R(46,49)	1.0241	-DE/DX =	0.0
R54	R(46,54)	2.0657	-DE/DX =	0.0
A1	A(2,1,3)	112.5266	-DE/DX =	0.0
A2	A(2,1,7)	108.8387	-DE/DX =	0.0
A3	A(2,1,8)	110.2928	-DE/DX =	0.0
A4	A(3,1,7)	108.2391	-DE/DX =	0.0
A5	A(3,1,8)	110.299	-DE/DX =	0.0
A6	A(7,1,8)	106.4252	-DE/DX =	0.0
A7	A(1,2,4)	111.7382	-DE/DX =	0.0
A8	A(1,2,5)	111.6636	-DE/DX =	0.0
A9	A(1,2,6)	110.7949	-DE/DX =	0.0
A10	A(4,2,5)	107.8616	-DE/DX =	0.0
A11	A(4,2,6)	107.8723	-DE/DX =	0.0
A12	A(5,2,6)	106.6852	-DE/DX =	0.0
A13	A(1,3,9)	110.3352	-DE/DX =	0.0
A14	A(1,3,10)	110.1882	-DE/DX =	0.0
A15	A(1,3,11)	109.9655	-DE/DX =	0.0
A16	A(9,3,10)	109.7874	-DE/DX =	0.0
A17	A(9,3,11)	109.9312	-DE/DX =	0.0

A18	A(10,3,11)	106.5631	-DE/DX =	0.0
A19	A(2,4,12)	109.1917	-DE/DX =	0.0
A20	A(2,4,13)	108.7978	-DE/DX =	0.0
A21	A(2,4,54)	116.5228	-DE/DX =	0.0
A22	A(12,4,13)	102.9026	-DE/DX =	0.0
A23	A(12,4,54)	108.1741	-DE/DX =	0.0
A24	A(13,4,54)	110.3766	-DE/DX =	0.0
A25	A(3,9,14)	112.5829	-DE/DX =	0.0
A26	A(3,9,15)	111.3211	-DE/DX =	0.0
A27	A(3,9,16)	110.2015	-DE/DX =	0.0
A28	A(14,9,15)	108.0171	-DE/DX =	0.0
A29	A(14,9,16)	107.8436	-DE/DX =	0.0
A30	A(15,9,16)	106.6296	-DE/DX =	0.0
A31	A(9,14,17)	106.7919	-DE/DX =	0.0
A32	A(9,14,18)	106.6259	-DE/DX =	0.0
A33	A(9,14,53)	125.4064	-DE/DX =	0.0
A34	A(17,14,18)	104.4836	-DE/DX =	0.0
A35	A(17,14,53)	102.8366	-DE/DX =	0.0
A36	A(18,14,53)	108.8692	-DE/DX =	0.0
A37	A(20,19,21)	112.6065	-DE/DX =	0.0
A38	A(20,19,22)	109.6305	-DE/DX =	0.0
A39	A(20,19,23)	110.2489	-DE/DX =	0.0
A40	A(21,19,22)	108.087	-DE/DX =	0.0
A41	A(21,19,23)	109.6931	-DE/DX =	0.0
A42	A(22,19,23)	106.3594	-DE/DX =	0.0
A43	A(19,20,24)	110.5092	-DE/DX =	0.0
A44	A(19,20,25)	111.487	-DE/DX =	0.0
A45	A(19,20,28)	114.1592	-DE/DX =	0.0
A46	A(24,20,25)	107.1631	-DE/DX =	0.0
A47	A(24,20,28)	107.1299	-DE/DX =	0.0
A48	A(25,20,28)	106.0174	-DE/DX =	0.0
A49	A(19,21,26)	108.29	-DE/DX =	0.0
A50	A(19,21,27)	109.8405	-DE/DX =	0.0
A51	A(19,21,34)	111.5122	-DE/DX =	0.0
A52	A(26,21,27)	106.839	-DE/DX =	0.0
A53	A(26,21,34)	109.8877	-DE/DX =	0.0
A54	A(27,21,34)	110.3391	-DE/DX =	0.0
A55	A(20,28,29)	109.5235	-DE/DX =	0.0
A56	A(20,28,30)	108.738	-DE/DX =	0.0
A57	A(20,28,53)	113.6737	-DE/DX =	0.0
A58	A(29,28,30)	103.0438	-DE/DX =	0.0

A59	A(29,28,53)	111.2845	-DE/DX =	0.0
A60	A(30,28,53)	110.0219	-DE/DX =	0.0
A61	A(32,31,33)	105.1466	-DE/DX =	0.0
A62	A(32,31,34)	107.826	-DE/DX =	0.0
A63	A(32,31,54)	107.8398	-DE/DX =	0.0
A64	A(33,31,34)	107.9534	-DE/DX =	0.0
A65	A(33,31,54)	107.6036	-DE/DX =	0.0
A66	A(34,31,54)	119.582	-DE/DX =	0.0
A67	A(21,34,31)	115.2799	-DE/DX =	0.0
A68	A(21,34,35)	110.0014	-DE/DX =	0.0
A69	A(21,34,36)	109.1787	-DE/DX =	0.0
A70	A(31,34,35)	106.1969	-DE/DX =	0.0
A71	A(31,34,36)	107.0993	-DE/DX =	0.0
A72	A(35,34,36)	108.8813	-DE/DX =	0.0
A73	A(38,37,39)	106.4575	-DE/DX =	0.0
A74	A(38,37,52)	104.3845	-DE/DX =	0.0
A75	A(38,37,53)	110.4824	-DE/DX =	0.0
A76	A(39,37,52)	103.7936	-DE/DX =	0.0
A77	A(39,37,53)	114.4499	-DE/DX =	0.0
A78	A(52,37,53)	116.3188	-DE/DX =	0.0
A79	A(41,40,42)	104.4754	-DE/DX =	0.0
A80	A(41,40,51)	106.6119	-DE/DX =	0.0
A81	A(41,40,53)	111.8962	-DE/DX =	0.0
A82	A(42,40,51)	103.3594	-DE/DX =	0.0
A83	A(42,40,53)	116.3022	-DE/DX =	0.0
A84	A(51,40,53)	113.2449	-DE/DX =	0.0
A85	A(44,43,45)	106.726	-DE/DX =	0.0
A86	A(44,43,50)	103.8063	-DE/DX =	0.0
A87	A(44,43,54)	112.4848	-DE/DX =	0.0
A88	A(45,43,50)	104.5744	-DE/DX =	0.0
A89	A(45,43,54)	112.4887	-DE/DX =	0.0
A90	A(50,43,54)	115.8824	-DE/DX =	0.0
A91	A(47,46,48)	106.1717	-DE/DX =	0.0
A92	A(47,46,49)	103.6568	-DE/DX =	0.0
A93	A(47,46,54)	113.8699	-DE/DX =	0.0
A94	A(48,46,49)	104.8836	-DE/DX =	0.0
A95	A(48,46,54)	111.7452	-DE/DX =	0.0
A96	A(49,46,54)	115.5799	-DE/DX =	0.0
A97	A(14,53,28)	94.603	-DE/DX =	0.0
A98	A(14,53,40)	92.0842	-DE/DX =	0.0
A99	A(28,53,37)	93.185	-DE/DX =	0.0

A100	A(37,53,40)	80.6098	-DE/DX =	0.0
A101	A(4,54,31)	92.2486	-DE/DX =	0.0
A102	A(4,54,46)	92.0513	-DE/DX =	0.0
A103	A(31,54,43)	93.7637	-DE/DX =	0.0
A104	A(43,54,46)	81.9644	-DE/DX =	0.0
D1	D(3,1,2,4)	162.9297	-DE/DX =	0.0
D2	D(3,1,2,5)	-76.1614	-DE/DX =	0.0
D3	D(3,1,2,6)	42.6095	-DE/DX =	0.0
D4	D(7,1,2,4)	42.9613	-DE/DX =	0.0
D5	D(7,1,2,5)	163.8702	-DE/DX =	0.0
D6	D(7,1,2,6)	-77.3589	-DE/DX =	0.0
D7	D(8,1,2,4)	-73.4427	-DE/DX =	0.0
D8	D(8,1,2,5)	47.4662	-DE/DX =	0.0
D9	D(8,1,2,6)	166.2371	-DE/DX =	0.0
D10	D(2,1,3,9)	-173.2492	-DE/DX =	0.0
D11	D(2,1,3,10)	65.3558	-DE/DX =	0.0
D12	D(2,1,3,11)	-51.8206	-DE/DX =	0.0
D13	D(7,1,3,9)	-52.9345	-DE/DX =	0.0
D14	D(7,1,3,10)	-174.3295	-DE/DX =	0.0
D15	D(7,1,3,11)	68.494	-DE/DX =	0.0
D16	D(8,1,3,9)	63.1267	-DE/DX =	0.0
D17	D(8,1,3,10)	-58.2683	-DE/DX =	0.0
D18	D(8,1,3,11)	-175.4448	-DE/DX =	0.0
D19	D(1,2,4,12)	-21.6936	-DE/DX =	0.0
D20	D(1,2,4,13)	89.9133	-DE/DX =	0.0
D21	D(1,2,4,54)	-144.5695	-DE/DX =	0.0
D22	D(5,2,4,12)	-144.7889	-DE/DX =	0.0
D23	D(5,2,4,13)	-33.182	-DE/DX =	0.0
D24	D(5,2,4,54)	92.3352	-DE/DX =	0.0
D25	D(6,2,4,12)	100.3222	-DE/DX =	0.0
D26	D(6,2,4,13)	-148.0709	-DE/DX =	0.0
D27	D(6,2,4,54)	-22.5537	-DE/DX =	0.0
D28	D(1,3,9,14)	166.905	-DE/DX =	0.0
D29	D(1,3,9,15)	45.4432	-DE/DX =	0.0
D30	D(1,3,9,16)	-72.6537	-DE/DX =	0.0
D31	D(10,3,9,14)	-71.4623	-DE/DX =	0.0
D32	D(10,3,9,15)	167.0759	-DE/DX =	0.0
D33	D(10,3,9,16)	48.9791	-DE/DX =	0.0
D34	D(11,3,9,14)	45.4561	-DE/DX =	0.0
D35	D(11,3,9,15)	-76.0057	-DE/DX =	0.0
D36	D(11,3,9,16)	165.8975	-DE/DX =	0.0

D37	D(2,4,54,31)	80.6271	-DE/DX =	0.0
D38	D(2,4,54,46)	-101.1881	-DE/DX =	0.0
D39	D(12,4,54,31)	-42.7759	-DE/DX =	0.0
D40	D(12,4,54,46)	135.4089	-DE/DX =	0.0
D41	D(13,4,54,31)	-154.6545	-DE/DX =	0.0
D42	D(13,4,54,46)	23.5302	-DE/DX =	0.0
D43	D(3,9,14,17)	156.1036	-DE/DX =	0.0
D44	D(3,9,14,18)	44.8345	-DE/DX =	0.0
D45	D(3,9,14,53)	-83.9476	-DE/DX =	0.0
D46	D(15,9,14,17)	-80.5728	-DE/DX =	0.0
D47	D(15,9,14,18)	168.1581	-DE/DX =	0.0
D48	D(15,9,14,53)	39.376	-DE/DX =	0.0
D49	D(16,9,14,17)	34.3153	-DE/DX =	0.0
D50	D(16,9,14,18)	-76.9538	-DE/DX =	0.0
D51	D(16,9,14,53)	154.2641	-DE/DX =	0.0
D52	D(9,14,53,28)	-17.3897	-DE/DX =	0.0
D53	D(9,14,53,40)	159.3519	-DE/DX =	0.0
D54	D(17,14,53,28)	104.3127	-DE/DX =	0.0
D55	D(17,14,53,40)	-78.9457	-DE/DX =	0.0
D56	D(18,14,53,28)	-145.2635	-DE/DX =	0.0
D57	D(18,14,53,40)	31.4781	-DE/DX =	0.0
D58	D(21,19,20,24)	-63.1944	-DE/DX =	0.0
D59	D(21,19,20,25)	55.8735	-DE/DX =	0.0
D60	D(21,19,20,28)	175.9782	-DE/DX =	0.0
D61	D(22,19,20,24)	57.175	-DE/DX =	0.0
D62	D(22,19,20,25)	176.2429	-DE/DX =	0.0
D63	D(22,19,20,28)	-63.6524	-DE/DX =	0.0
D64	D(23,19,20,24)	173.9393	-DE/DX =	0.0
D65	D(23,19,20,25)	-66.9928	-DE/DX =	0.0
D66	D(23,19,20,28)	53.1119	-DE/DX =	0.0
D67	D(20,19,21,26)	164.6114	-DE/DX =	0.0
D68	D(20,19,21,27)	48.2769	-DE/DX =	0.0
D69	D(20,19,21,34)	-74.3656	-DE/DX =	0.0
D70	D(22,19,21,26)	43.3579	-DE/DX =	0.0
D71	D(22,19,21,27)	-72.9765	-DE/DX =	0.0
D72	D(22,19,21,34)	164.3809	-DE/DX =	0.0
D73	D(23,19,21,26)	-72.2116	-DE/DX =	0.0
D74	D(23,19,21,27)	171.454	-DE/DX =	0.0
D75	D(23,19,21,34)	48.8114	-DE/DX =	0.0
D76	D(19,20,28,29)	-54.6197	-DE/DX =	0.0
D77	D(19,20,28,30)	57.2902	-DE/DX =	0.0

D78	D(19,20,28,53)	-179.7886	-DE/DX =	0.0
D79	D(24,20,28,29)	-177.308	-DE/DX =	0.0
D80	D(24,20,28,30)	-65.3981	-DE/DX =	0.0
D81	D(24,20,28,53)	57.5231	-DE/DX =	0.0
D82	D(25,20,28,29)	68.5033	-DE/DX =	0.0
D83	D(25,20,28,30)	-179.5868	-DE/DX =	0.0
D84	D(25,20,28,53)	-56.6656	-DE/DX =	0.0
D85	D(19,21,34,31)	176.3628	-DE/DX =	0.0
D86	D(19,21,34,35)	56.3505	-DE/DX =	0.0
D87	D(19,21,34,36)	-63.0704	-DE/DX =	0.0
D88	D(26,21,34,31)	-63.5508	-DE/DX =	0.0
D89	D(26,21,34,35)	176.4369	-DE/DX =	0.0
D90	D(26,21,34,36)	57.0159	-DE/DX =	0.0
D91	D(27,21,34,31)	54.0065	-DE/DX =	0.0
D92	D(27,21,34,35)	-66.0058	-DE/DX =	0.0
D93	D(27,21,34,36)	174.5733	-DE/DX =	0.0
D94	D(20,28,53,14)	89.8114	-DE/DX =	0.0
D95	D(20,28,53,37)	-97.4306	-DE/DX =	0.0
D96	D(29,28,53,14)	-34.4113	-DE/DX =	0.0
D97	D(29,28,53,37)	138.3466	-DE/DX =	0.0
D98	D(30,28,53,14)	-147.9745	-DE/DX =	0.0
D99	D(30,28,53,37)	24.7834	-DE/DX =	0.0
D100	D(32,31,34,21)	-49.5763	-DE/DX =	0.0
D101	D(32,31,34,35)	72.5023	-DE/DX =	0.0
D102	D(32,31,34,36)	-171.271	-DE/DX =	0.0
D103	D(33,31,34,21)	63.5469	-DE/DX =	0.0
D104	D(33,31,34,35)	-174.3745	-DE/DX =	0.0
D105	D(33,31,34,36)	-58.1478	-DE/DX =	0.0
D106	D(54,31,34,21)	-173.1206	-DE/DX =	0.0
D107	D(54,31,34,35)	-51.0421	-DE/DX =	0.0
D108	D(54,31,34,36)	65.1846	-DE/DX =	0.0
D109	D(32,31,54,4)	-128.4102	-DE/DX =	0.0
D110	D(32,31,54,43)	50.8183	-DE/DX =	0.0
D111	D(33,31,54,4)	118.6299	-DE/DX =	0.0
D112	D(33,31,54,43)	-62.1416	-DE/DX =	0.0
D113	D(34,31,54,4)	-4.8725	-DE/DX =	0.0
D114	D(34,31,54,43)	174.356	-DE/DX =	0.0
D115	D(38,37,53,28)	-107.1064	-DE/DX =	0.0
D116	D(38,37,53,40)	77.0211	-DE/DX =	0.0
D117	D(39,37,53,28)	132.7579	-DE/DX =	0.0
D118	D(39,37,53,40)	-43.1146	-DE/DX =	0.0

D119	D(52,37,53,28)	11.62	-DE/DX =	0.0
D120	D(52,37,53,40)	-164.2525	-DE/DX =	0.0
D121	D(41,40,53,14)	-115.1971	-DE/DX =	0.0
D122	D(41,40,53,37)	72.5696	-DE/DX =	0.0
D123	D(42,40,53,14)	4.7481	-DE/DX =	0.0
D124	D(42,40,53,37)	-167.4852	-DE/DX =	0.0
D125	D(51,40,53,14)	124.2741	-DE/DX =	0.0
D126	D(51,40,53,37)	-47.9592	-DE/DX =	0.0
D127	D(44,43,54,31)	127.5712	-DE/DX =	0.0
D128	D(44,43,54,46)	-50.5385	-DE/DX =	0.0
D129	D(45,43,54,31)	-111.8677	-DE/DX =	0.0
D130	D(45,43,54,46)	70.0226	-DE/DX =	0.0
D131	D(50,43,54,31)	8.369	-DE/DX =	0.0
D132	D(50,43,54,46)	-169.7406	-DE/DX =	0.0
D133	D(47,46,54,4)	138.5366	-DE/DX =	0.0
D134	D(47,46,54,43)	-40.4943	-DE/DX =	0.0
D135	D(48,46,54,4)	-101.1717	-DE/DX =	0.0
D136	D(48,46,54,43)	79.7973	-DE/DX =	0.0
D137	D(49,46,54,4)	18.664	-DE/DX =	0.0
D138	D(49,46,54,43)	-160.3669	-DE/DX =	0.0

*R bond length, A angles, D dihedral angles for the numbered atoms present in the Figure A4.

Appendix B

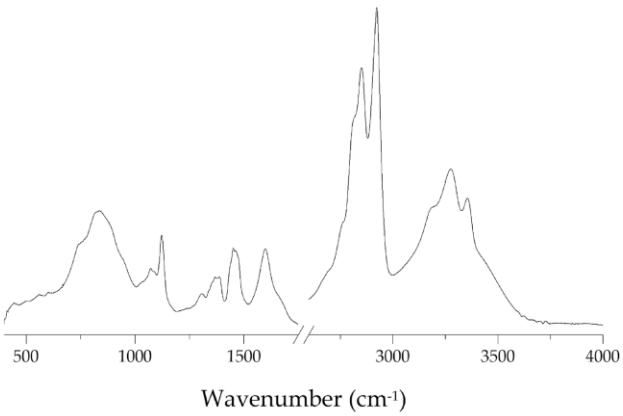

Figure B1: FTIR spectrum (400 – 1800 cm^{-1} and 2600 – 4000 cm^{-1}) of the free ligand dihydrochloride spermidine.

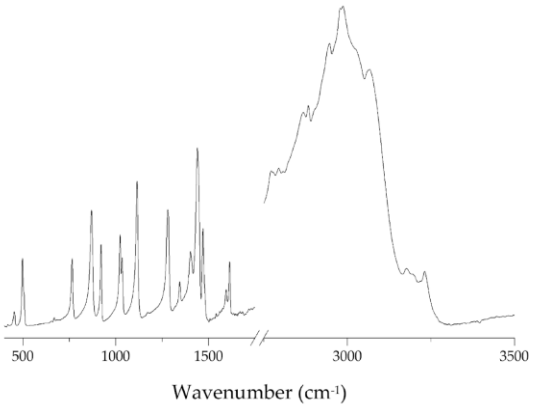

Figure B2: FTIR spectrum (600 – 1800 cm^{-1} and 2600 – 3500 cm^{-1}) of the free ligand dihydrochloride putrescine.

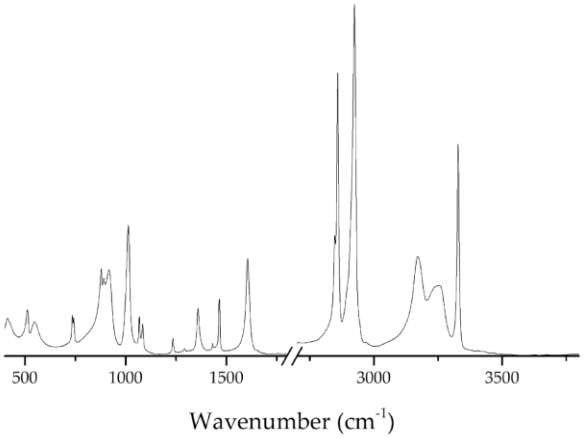

Figure B3: FTIR spectrum (600 – 1800 cm^{-1} and 2600 – 3800 cm^{-1}) of the free ligand neutral putrescine.

Appendix C

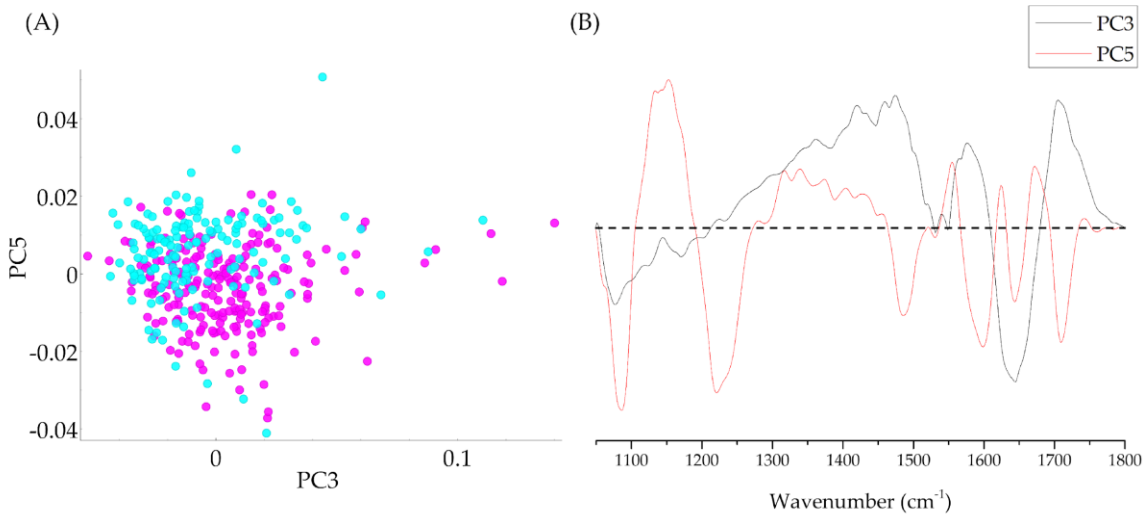

Figure C1: PCA score (A) and loading plots (B) of FTIR (1050 – 1800 cm^{-1}) data for HOb cell line, cisplatin combination *vs* cisplatin.

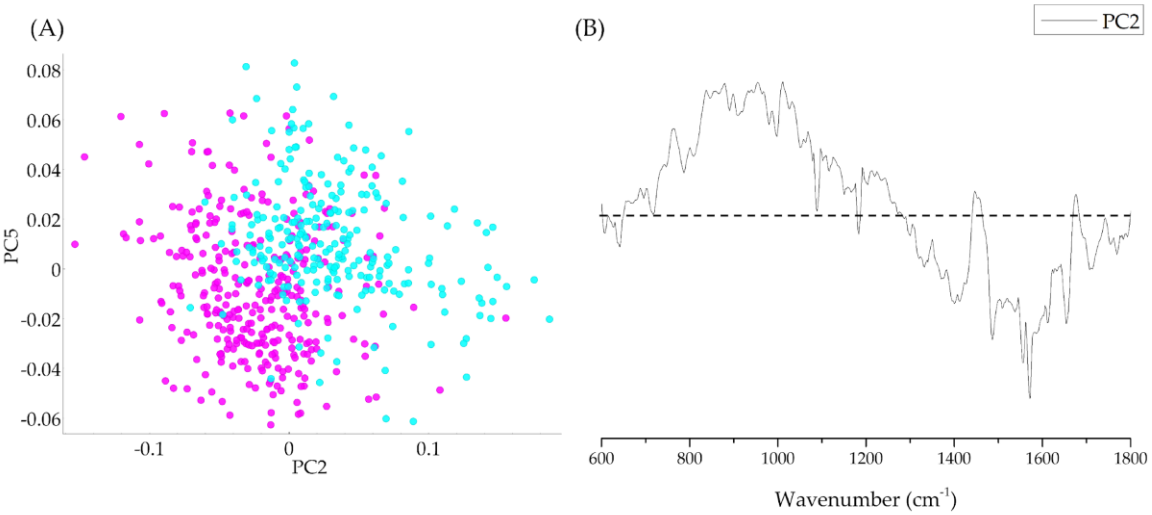

Figure C2: PCA score (A) and loading plots (B) of Raman (600 – 1800 cm^{-1}) data for HOb cell line, cisplatin combination *vs* cisplatin.

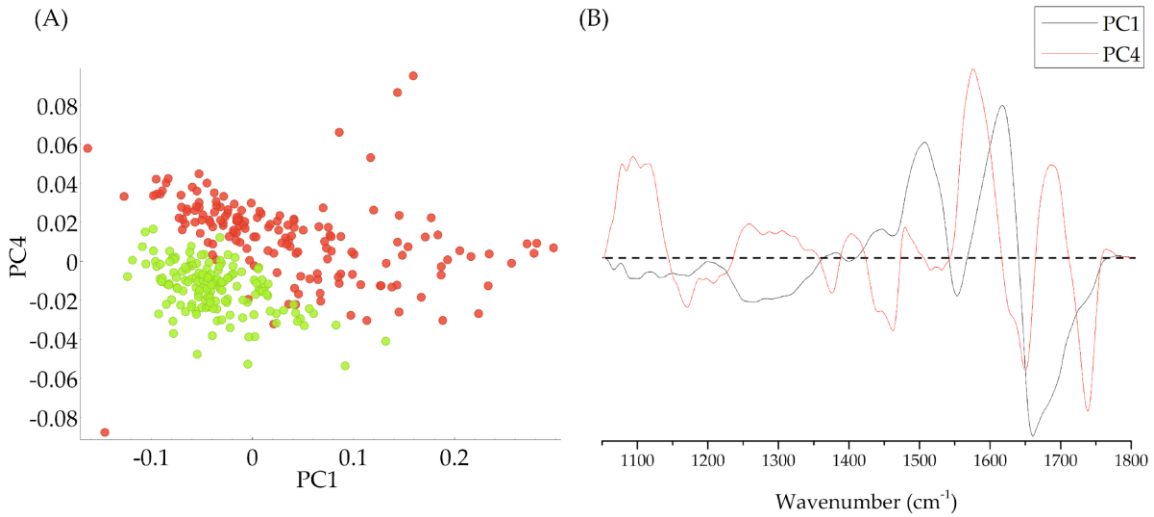

Figure C3: PCA score (A) and loading plots (B) of FTIR (1050 – 1800 cm^{-1}) data for HOb cell line, Pd_2SpmCl_4 combination *vs* Pd_2SpmCl_4.

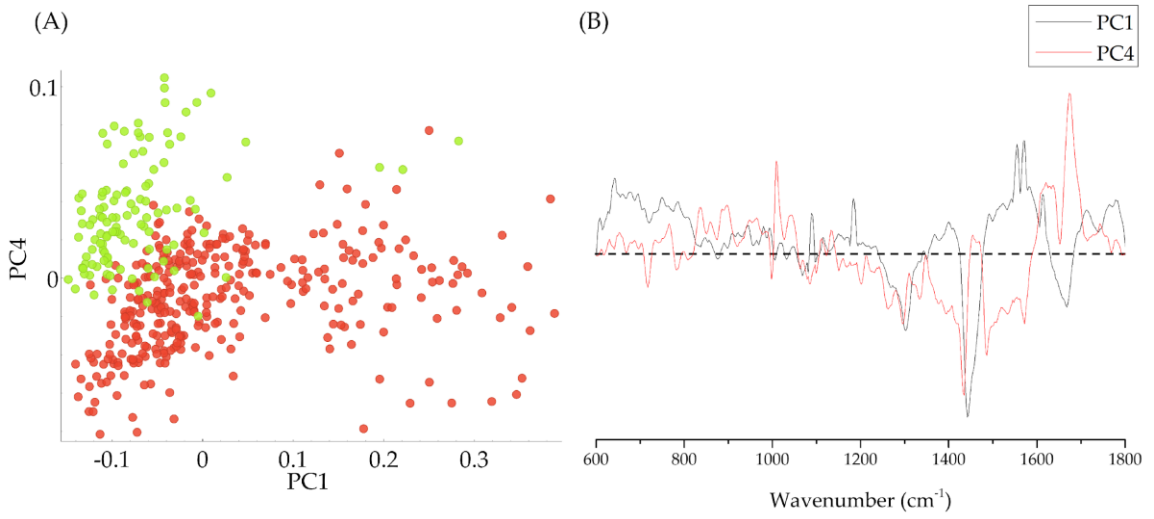

Figure C4: PCA score (A) and loading plots (B) of Raman (600 – 1800 cm^{-1}) data for HOb cell line, Pd_2SpmCl_4 combination *vs* Pd_2SpmCl_4.

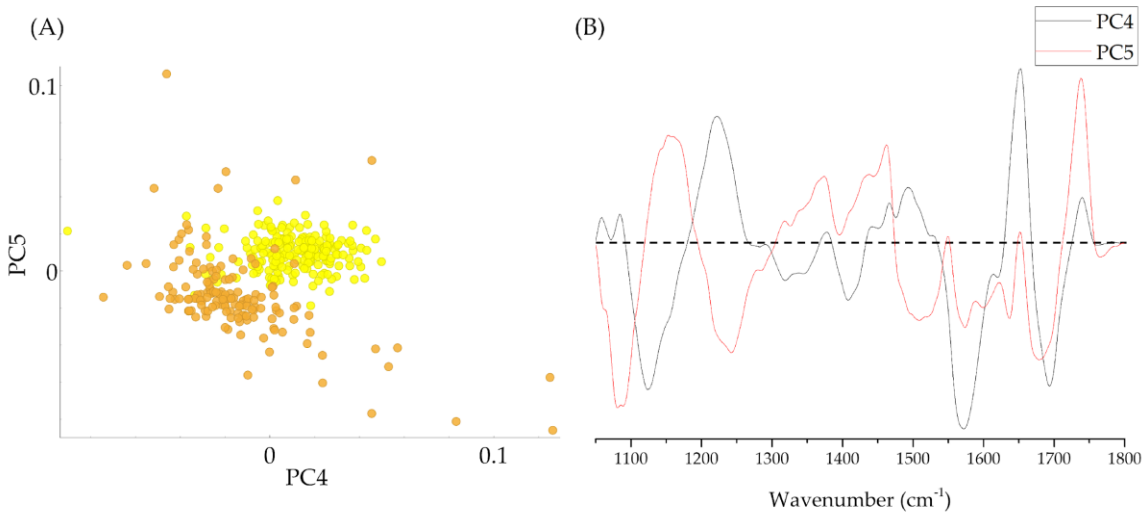

Figure C5: PCA score (A) and loading plots (B) of FTIR (1050 – 1800 cm^{-1}) data for HOb cell line, $Pd_3Spd_2Cl_6$ combination *vs* $Pd_3Spd_2Cl_6$.

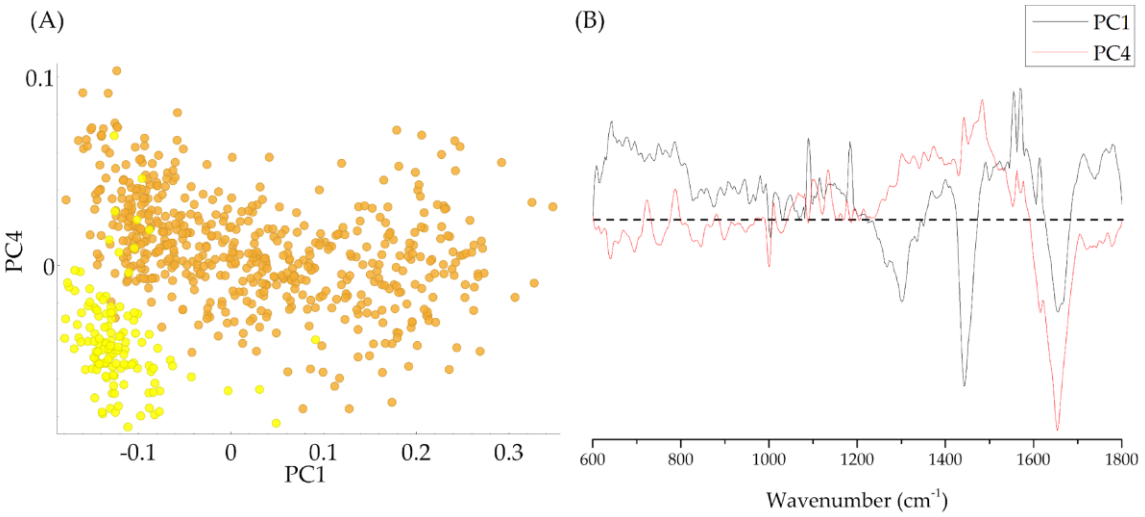

Figure C6: PCA score (A) and loading plots (B) of Raman (600 – 1800 cm^{-1}) data for HOb cell line, $Pd_3Spd_2Cl_6$ combination *vs* $Pd_3Spd_2Cl_6$.

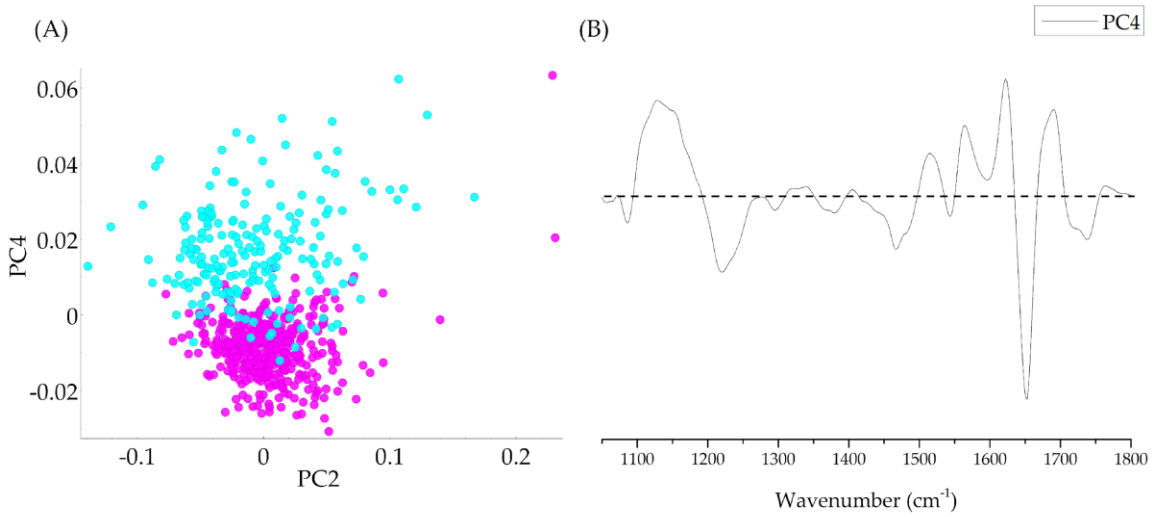

Figure C7: PCA score (A) and loading plots (B) of FTIR (1050 – 1800 cm^{-1}) data for MG-63 cell line, cisplatin combination *vs* cisplatin.

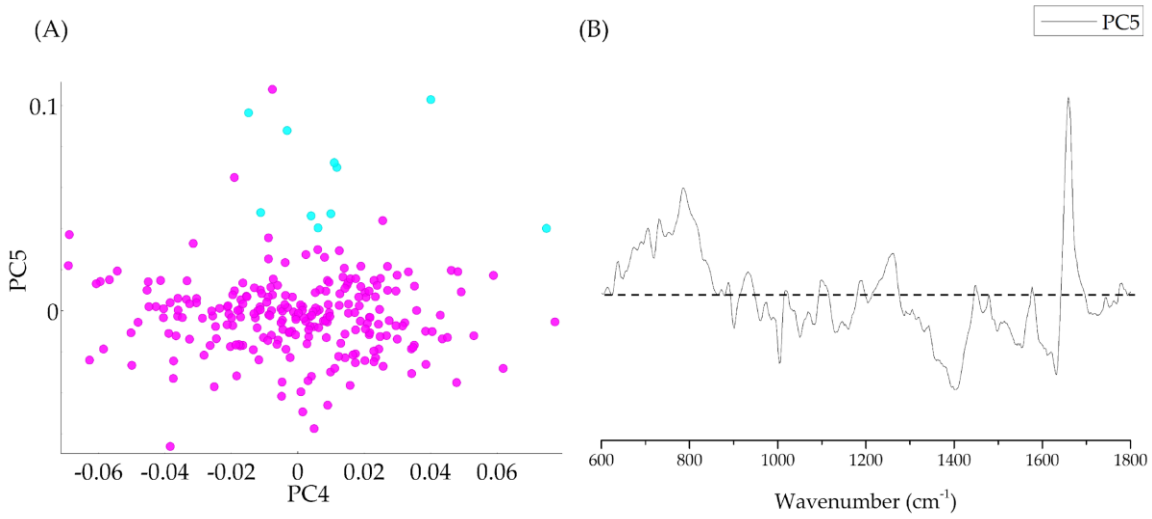

Figure C8: PCA score (A) and loading plots (B) of Raman (600 – 1800 cm^{-1}) data for MG-63 cell line, cisplatin combination *vs* cisplatin.

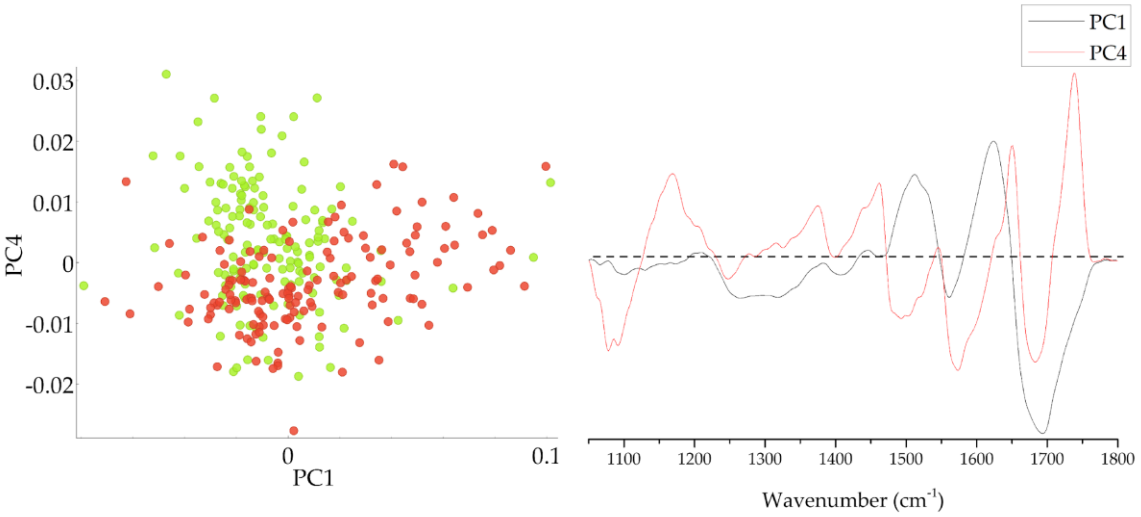

Figure C9: PCA score (A) and loading plots (B) of FTIR (1050 – 1800 cm^{-1}) data for MG-63 cell line, Pd_2SpmCl_4 combination *vs* Pd_2SpmCl_4.

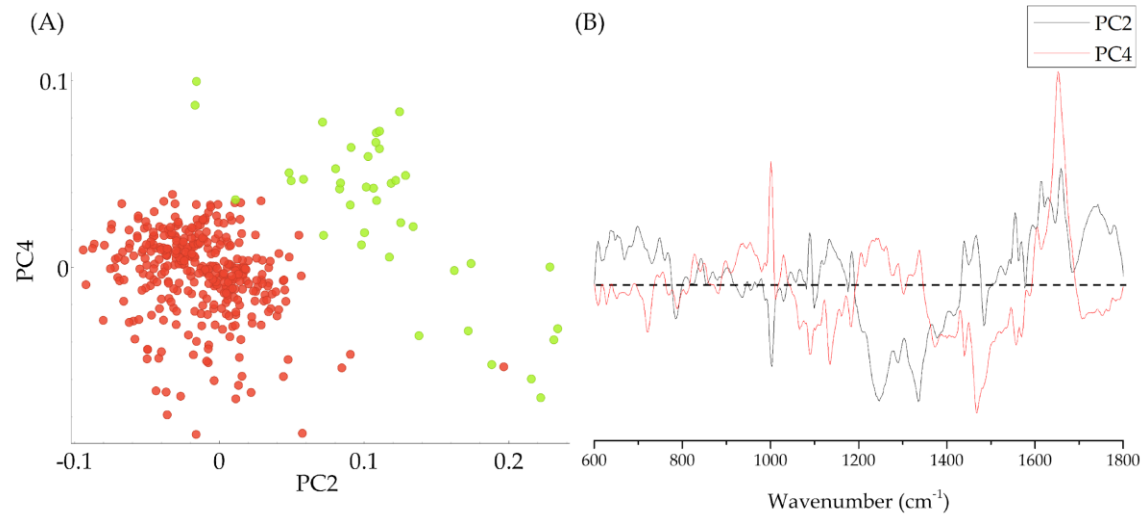

Figure C10: PCA score (A) and loading plots (B) of Raman (600 – 1800 cm^{-1}) data for MG-63 cell line, Pd_2SpmCl_4 combination *vs* Pd_2SpmCl_4.

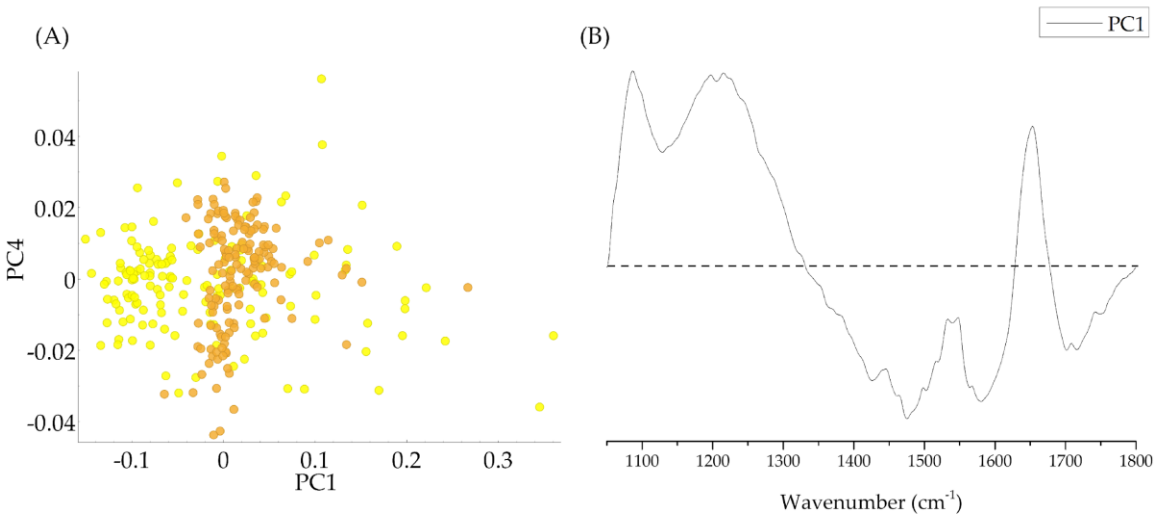

Figure C11: PCA score (A) and loading plots (B) of FTIR (1050 – 1800 cm^{-1}) data for MG-63 cell line, $Pd_3Spd_2Cl_6$ combination *vs* $Pd_3Spd_2Cl_6$.

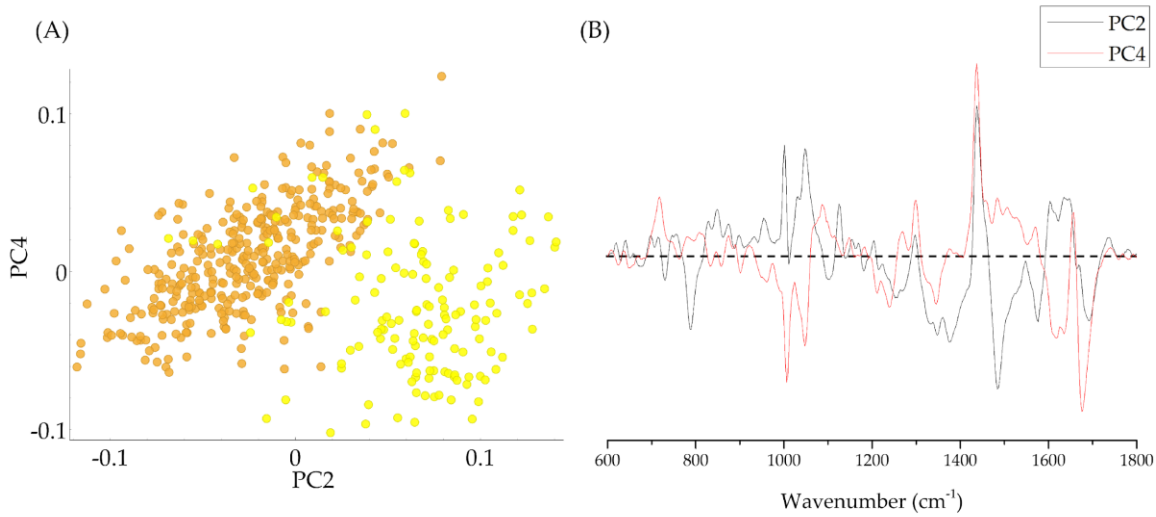

Figure C12: PCA score (A) and loading plots (B) of Raman (600 – 1800 cm^{-1}) data for M;G-63 cell line, $Pd_3Spd_2Cl_6$ combination *vs* $Pd_3Spd_2Cl_6$.